The Effect of Flow History on the Crystallization of Semicrystalline Polymers

Thesis by

Guruswamy Kumaraswamy

In Partial Fulfillment of the Requirements
for the Degree of
Doctor of Philosophy

California Institute of Technology
Pasadena, California

2000

(Defended March 1, 2000)

To my parents

Abstract

Semicrystalline polymers constitute well over half of all the polymers produced worldwide. Their material properties depend sensitively on the thermal and flow history experienced during processing which strongly influences the kinetics of phase change and the morphology of the final crystalline microstructure. Therefore, it is of considerable interest to understand the mechanisms of flow effects on the rate and geometry of nucleation and crystal growth.

Microstructural development under the influence of flow is controlled by the interplay between melt relaxation processes and crystallization processes: the thermodynamic and kinetic aspects give rise to rich physics that are not well understood. This thesis elucidates key fundamentals of this process. We develop novel instrumentation that improves over prior approaches by examining the development of order at all the length scales of interest (*in-situ* rheo-optics, synchrotron small angle X-ray scattering (SAXS), and wide angle X-ray diffraction (WAXD), and *ex-situ* electron and optical microscopy); and by reducing the sample requirement by about three orders of magnitude, opening the way to study of model materials. We investigate a polydisperse, commercial Ziegler-Natta isotactic polypropylene (iPP) using the short term shearing protocol pioneered by the group of Janeschitz-Kriegl which imposes a well defined thermal and flow history on the polymer.

Rheo-optical investigations reveal that imposition of brief intervals of shear (less than a thousandth of the quiescent crystallization time) reduces the crystallization time by two orders of magnitude at a crystallization temperature of 141°C. Above a critical value of the shear stress, there is a transition to highly oriented growth with increase in shearing duration. This transition is correlated with changes in the transient behavior during flow and the semicrystalline morphology observed *ex-situ*. During flow, we observe the generation of long-lived, highly oriented structures (evident in the transient birefringence) under all conditions that induce subsequent

growth of highly oriented crystallites. In turn, the development of oriented crystallites observed *in-situ* after cessation of flow correlates with development of a "skin-core" morphology observed *ex-situ.*

The transient structures that develop during flow are identified as oriented α-phase crystals by WAXD, and show an unexpected temperature dependence for their time of formation: with *increase* in temperature, they occur at *shorter* times after startup of flow. This very unusual temperature dependence is strikingly similar to that for rheological processes, and is in contrast to the exponential increase expected for crystallization time-scales. Thus, the transition to anisotropic nucleation in polymers subjected to flow follows a non-classical kinetic pathway controlled by the formation of a transient, highly oriented metastable melt state.

In-situ synchrotron SAXS and WAXD reveal that for shearing conditions that lead to anisotropic morphologies, crystals that are highly oriented in the flow direction develop during shear, templating the formation of crystallites after flow cessation. In the densely nucleated skin regions, *ex-situ* TEM shows lamellae growing radially from oriented central "shish" structures until they impinge to form the "shish-kebab" or row-nucleated structures. Under milder shear conditions, the rate of crystallization is gradual compared to strong shearing, and less oriented morphologies develop. Interestingly the ratio of parent to the crosshatched, epitaxial daughter lamellae for the oriented crystallites increases with increase in shearing time, imposed wall shear stress and temperature.

Our data suggests a mechanistic model for shear-enhanced crystallization: the rheologically-controlled formation of a critical anisotropic distribution of chain segments in the melt upon imposition of flow nucleates oriented crystallites. For intense shearing conditions, these line-nuclei are long and dense. Row nucleated structures develop from these line nuclei as lamellae grow radially to form fully impinged structures. For milder shearing conditions, lower nucleation densities lead to the development of less oriented structures.

Acknowledgements

I am fortunate to have run into some amazingly helpful people during my time at Caltech. Interacting with them will count among my best graduate school experiences; it is truly a pleasure to recollect those experiences and thank those people.

At first, I would like to acknowledge what a pleasure it has been to study at Caltech. While I might have had the usual (perhaps slightly more severe) misgivings about graduate school and the nature of graduate education in general, I have always enjoyed the constant intellectual stimulation and friendly, department-boundary-free atmosphere at Caltech. It is probably only here that I could, as a first year chemical engineering graduate student, find it so easy to get help (and I needed a great deal of it) in my synthetic efforts (thanks to Steve Miller, Geoff Coates and Marcus Weck in Chemistry and Zhibin Guan in ChemE), setting up a DLS instrument (Steve Paulin) and learning to do AFM (Steve O'Connor and Marc Unger in Chemistry). Useful advice received from Greg Smedley while building my instrument is also gratefully acknowledged. Innovative and friendly machine shop experts (Mike, Guy and Ray in Chemistry, Rodney in Mechanical and Bovan and Mike in Central) and the chemistry electronics guru (Tom Dunn) made designing and building equipment considerably easier than it might have been. Special thanks to Suresh Guptha for tolerating my frequent visits to his office and innumerable and often naive queries.

I would like to thank my advisor, Julie Kornfield, for her tremendous enthusiasm, keen insights into data, funding numerous conferences uncomplainingly and especially for her patience with me. I have learnt a great deal from interacting with her and doing research in her group. Members of the Kornfield group, both past (Vinay, Susan, Steve Paulin, Barbara, Zhongren, Mike Reddig, Sunil, Ravi, Deniz) and present (Weijun, Ani, Giyoong, Mike Kempe, Wei, Yan, Jagdish and Christian), have provided a great work environment in the lab for which I am very grateful. I would especially like to thank Sunil, Jagdish, Weijun, Vinay and Chris for often lending a sympathetic ear to real and imaginary woes and for help with numerous lab related and unrelated things; Ravi, for his advice when I started working with semicrystalline polymers; and Ani, for her help with microtoming and electron microscopy, and for the best *baklava* that I have ever had. I also had the opportunity to work with an undergraduate student, Joanna who did many hours of polypropylene characterization: I hope she got as much out of her surfs as I did working with her. Thanks are also due to our group secretary, Anne Hormann for keeping everything in the group well oiled and running, for parting the (otherwise impassable) waters of administrative detail on many occasions, and for always being cheerful.

I am very grateful to Bob Sammler and Clive Bosnyak at Dow Chemical and Abaneshwar Prasad at Equistar for providing me with samples and characterization. My first two papers read better, thanks to Bob Sammler's keen eye for detail and insistence on stating things precisely yet clearly, with minimal jargon or obfuscation. Thanks are also due to my collaborators outside Caltech from whom I have learnt a great deal about synchrotron X-ray scattering, Prof. Benjamin Hsiao and Dr. Fengji Yeh (both SUNY, Stony-Brook).

I would also like to thank my committee members, Prof. R. H. Grubbs, Prof. Z. G. Wang and Prof. J. E. Bercaw for taking the time to read my thesis and attend my presentation.

Thanks are also due to several people (not already mentioned) whom I am privileged to call my friends: the ChemE hiking club: Dave, Jeremy, Jason, Sumit, Doris, Peter, Steve Glade. I would also like to thank the *desi* gang: Vidya, Amit, Sane, Ravi Abrol, Goutam, Sulekha, Ramesh, Ganesh, Anil, Bhavna, Nitin, Prashant, Puru, Rajiv and Shachi for dinners, *chai* get-togethers, entertainment and endless discussions on every imaginable topic. Thanks are also due to my non-Caltech friends: TK, Harish, Srikanth, Dole, Kashyap, Arjun and Raggy for reality checks, widely different perspectives and for making life more varied and enjoyable.

Finally, I would like to acknowledge my family in Bombay, especially my parents, Kumaraswamy and Jaya and my sister, Meenu for everything that they have done. Words cannot do justice to what I owe them.

Contents

List of Figures

List of Tables

Chapter 1 Introduction

1.1 Background

Chemically and structurally regular macromolecules that can arrange into a crystalline lattice are called semicrystalline polymers. Topological frustration imposed by the covalent connectivity of these long-chain molecules prevents complete crystallization, and a variety of morphologies can be formed depending on the conditions of crystallization.[1–3] Controlling the crystallization conditions allows us to control the semicrystalline morphology and, consequently, the material properties in the final product.[4] Due to the desirable qualities of semicrystalline polymers, such as the high strength to weight ratio, the range over which their material properties can be tuned and the ease with which they can be processed relative to metals and ceramics, their worldwide consumption has seen a continued increase since their introduction. Currently, semicrystalline polymers comprise about two-thirds by volume of the vast 100 million ton a year polymer industry.[5,6] Worldwide use of polyolefins alone exceeded 125 billion pounds in 1997.[6] Due to their versatility, semicrystalline polymers are ubiquitous[5,7]: high volume commodity polymers such as polyethylenes and isotactic polypropylene are used to make films (for packaging applications, bags, pouches, and wrappings for produce, trash bags, agricultural applications in greenhouses, ground cover, canal linings, construction related applications such as moisture barriers and utility covering materials), fibers (for textile, cables, carpeting applications, etc.) and molded objects (for rigid containers, hot-fill bottles, furniture, toys, housewares, automotive parts, etc.); lower volume, engineering plastics such as nylons, polyesters, polyoxymethylene, polyethersulfone, polyetheretherketone, etc., that are able to withstand high operating temperatures and corrosive environments are being used increasingly for applications in electronics, medical devices (e.g., hip implants) and underhood automotive parts (such as intake manifolds, gas tanks, centrifugal fans).

Despite the wide range of applications, the number of monomeric motifs that commercial semicrystalline polymers are typically made up of is rather small. However, resins with widely different properties have been produced through the innovative use of catalyst chemistry and polymerization conditions to link this limited set of monomeric units in a variety of ways.[8–12] In recent times, advances in single-site metallocene catalysis[8–10] and other novel chemistries[11,12] have opened up routes for the synthesis of polymers with systematic control over molecular weight, molecular weight distribution and chain architecture (chain topology, branching characteristics, comonomer ratios and distribution, blockiness in elastomeric resins, etc.). Unfortunately, limited current understanding of how these molecular variables influence crystallization, especially under processing-like flow conditions, has severly hampered the translation of this exquisite control over polymer synthesis into the development of new product lines. None of the state-of-the-art models[13–17] for flow induced crystallization can accurately predict the crystallization kinetics and microstructure a priori, given the flow field and the molecular characteristics of the resin. In fact, most of the currently used models combine phenomenology with thermodynamics and rely on empirical adjustable parameters to fit experimental data. To enable rational design of processing conditions and resins to optimize material properties in the final product, it is necessary to clearly understand how molecular characteristics influence the relation between processing, structure development and final properties. Therefore, the goal of this thesis is to develop experimental tools to address the problem of structure formation under flow and to explore the influence of the relaxation dynamics of the crystallizing polymer melt on the kinetics and anisotropy of microstructural development using "clean" experiments under well controlled and characterized conditions. It is hoped that this work will open up investigations of the effect of molecular variables such as stereoregularity, molecular weight distribution and branching enabled by the availability of new model metallocene polymers.

We begin this chapter with a brief introduction to quiescent crystallization in semicrystalline polymers and discuss morphological aspects and some of the factors that influence crystallization kinetics. We then motivate our studies on the effect of flow on polymer crystallization with some examples that lay out the scope of this work. Finally, we outline the organization of the thesis.

1.1.1 Crystallization in Semicrystalline Polymers: Morphological Aspects

Crystallization is a first order liquid to solid phase transition involving a change in density and symmetry.[1,2] Thus, it takes place by a nucleation and growth mechanism. In polymers, the long chain nature of the molecules makes crystallization a far from equilibrium process. Due to the nonequilibrium nature, amorphous and crystal phases coexist in apparent violation of the Gibbs phase rule. Thus, equilibrium treatments cannot be used to predict crystallization rates or the structure of the polymer crystals, and kinetic factors are important.

Kinetic constraints on crystallization play an important role in determining the crystal morphology.[18,3] Crystallites grow by reorganizing random-coil chains into platelet-like crystalline lamellae (typically $\sim$ O(10 nm) thick) bounded by the interlamellar region[19,20] and separated by regions of noncrystalline material (Figure 1.1). Since the chains in the lamellae are frequently aligned at large angles to the basal plane and since the dimensions of the lamellae are far smaller than the length of the polymer molecule, it was concluded that the lamellae consisted of chain-folded molecules.[21] This discovery forms the basis for most of the current understanding of polymer crystal morphology. Lamellar crystals are observed in growth from both solutions as well as melts. During crystallization from a quiescent melt, crystallization commonly proceeds by the nucleation of a fiber like structure which evolves into a sheaf like entity composed of a few splayed or non-crystallographically branched lamellae. These sheaves continue to splay and branch as they grow and form a spherical envelope called a spherulite (Figure 1.2). The non-crystallographic branching of lamellar stacks was explained by Keith and Padden[22–24] by considering the segregation of non crystallizable "impurities" (comonomers, stereoirregular units, branches, etc.) to the crystal-melt interface. This causes the growing planar interface to become unstable to the formation of fibrils, and leads to branching. Recently, it has been shown[25–27] that this model is unable to explain spherulite formation in some cases and alternate mechanisms are being investigated. Once spherulitic structures are formed, they continue to grow (primary crystallization) until they impinge. There is a further increase in the crystallinity (secondary crystallization) after spherulitic impingement due to the crystallization of thinner, more imperfect crystal stacks in confined regions of uncrystallized melt.[19,20]

It is interesting to note the range of length scales spanned by the hierarchy of ordered structures formed when polymers crystallize.[18,3] Polymer chains in a crystal adopt their lowest free energy stable conformations, and are typically either in the form of linear zig-zags (e.g., polyethylene) or helices (e.g., isotactic polypropylene). These extended forms pack together with periodicities on the order of a few angstroms, and chain fold into the lath like lamellae ($\sim$ 10 nm). Sheaf-like stacks formed by these crystalline lamellae are around 50-100 nm thick while spherulites can range in size from submicron to millimeters. Structural order ranging from angstroms to millimeters leads to a rich variety in morphology: characterization of crystalline structure in polymers is therefore challenging and necessitates several techniques to span the range of length scales.

1.1.2 Crystallization in Semicrystalline Polymers: Kinetic Models

To explain the formation of these non-equilibrium morphological features, kinetic theories have been formulated that capture various aspects of crystallization kinetics. At a gross level, kinetics of isothermal phase transformation are often modeled using the geometric Avrami model.[28,29] According to this model, crystals nucleate at random throughout the volume of the melt and grow in 1, 2 or 3 dimensions. The crystal volume fraction, $x(t)$ at a time t, is given by:

$$x(t) = \int_0^t v(t,\tau)\dot{n}(\tau)[1 - x(\tau)]d\tau \tag{1.1}$$

where $v(t,\tau)$ is the volume of a crystal at time t that was nucleated at time τ and $\dot{n}(t)$ is the nucleation rate at time t. For three-dimensional crystal growth, $v(t,\tau)$ can be written as:

$$v(t,\tau) = f g_x g_y g_z (t-\tau)^3 \tag{1.2}$$

where f is a factor that depends on the growth geometry and g_x, g_y and g_z are growth rates in different directions. Since polymers cannot crystallize completely, the Avrami analysis is modified to give[1]:

$$ln[1 - \frac{x(t)}{x(\infty)}] = \frac{-kt^n}{x(\infty)} \tag{1.3}$$

where $x(\infty)$ is the crystalline volume fraction after long crystallization times, k is a constant that depends on the nucleation and growth rates while n is the "Avrami" exponent which takes values from 1 to 4 depending on the nature of crystallization (See Table 1.1).

Growth geometry	Homogeneous nucleation		Heterogeneous nucleation
	Linear growth	Diffusion controlled growth	Linear growth
1 dimensional	2	1.5	$1 \leq n \leq 2$
2 dimensional	3	2	$2 \leq n \leq 3$
3 dimensional	4	2.5	$3 \leq n \leq 4$

Table 1.1: Avrami exponents for different crystallization conditions. The advance of the growth front scales linearly with time ($\sim t$) for linear growth and $\sim t^{1/2}$ for diffusion controlled growth.

While the Avrami analysis does not predict an induction time for crystallization, the "apparent" induction time (when the level of crystallinity is below the limits of experimental detection) increases as n is increased from 1 to 4. However, apart from this change in the apparent induction time, the shape of the crystallization data is similar for different n, especially during the early stages of phase transformation. This makes it difficult to analyze crystallization kinetics using the Avrami model. Further, the Avrami model is simply a phenomenological geometric model and does not provide a molecular picture of crystallization. Thus, the Avrami model cannot explain experimental observations such as changes in the slope of the crystal growth rates with temperature or the dependence of the melting point, T_m, for polymer crystals on the crystallization temperature, T_{cryst} (T_m increases with T_{cryst}).

The surface nucleation theory of Lauritzen and Hoffmann[30,31] provides a molecular understanding of crystallization and is able to account for and predict several experimental observations. According to the theory, lamellar growth takes place through a process of secondary nucleation: polymer chains from the melt deposit onto the growing face of the lamella and form secondary nuclei (Figure 1.3). Accretion of polymer strands into the crystal leads to a change in the free energy of the system due to contributions from the free energy of fusion and the surface energy penalty incurred due to the formation of new crystal-melt interfaces. Therefore, as strands are added on, the free energy of formation of the surface nucleus goes through a maximum and then decreases monotonically. This model is similar to classical nucleation theory[32] and thus, the growth speed of the lamella, g, at a temperature T is given by an analogous expression:

$$g = g_o exp[\frac{-U^*}{k_B T}] exp[\frac{-K_g}{T \Delta T f}] \tag{1.4}$$

where g_o is a constant, $\frac{-U^*}{k_B T}$ is a term associated with the transport of polymer chains to the crystal surface, K_g is a temperature independent term, ΔT is the subcooling and f accounts for variations in the heat of fusion with temperature. Thus, g vanishes as the temperature approaches the glass transition temperature (due to the transport term) and as ΔT approaches zero (due to the driving force term) in accord with experimental observations (Figure 1.4). The Lauritzen-Hoffmann theory explains changes in crystal growth speeds with temperature by postulating different nucleation mechanisms[30,31,33]: in regime I (low subcoolings), the rate of deposition of secondary nuclei on the crystal surface is much smaller than the rate of lateral spreading and thus, lateral crystal growth along the entire substrate is completed after the deposition of just one nucleus; at higher subcoolings (regime II), nuclei are deposited more rapidly than they can spread laterally, and thus numerous nuclei are formed on a substrate; at even higher subcoolings (regime III), nuclei are deposited such that the average separation between adjacent nuclei is on the order of the width of a nucleus. The change in growth rates at transitions between these regimes have been experimentally verified for several systems, to accord well with the theory. This is one of the major successes of this model. The change in growth rate comes about due to a change in the constant K_g in Equation 1.4:

$$K_g(I) = 2K_g(II) = K_g(III) = \frac{4b\sigma\sigma_e \mathrm{T}_{Mo}}{k_B(\Delta h_f)} \tag{1.5}$$

where b is the thickness of the deposited nucleus, σ and σ_e are surface energies of the basal and lateral planes respectively (see Figure 1.3), Δh_f is the enthalpy of fusion and T_{Mo} is the equilibrium melting point with respect to which the subcoolings are calculated. Regime transitions in the Lauritzen-Hoffman theory are highly dependent on the value of the equilibrium melting point, T_{Mo}, defined as the melting point for an infinite stack of extended chain crystals where polymer chain ends have been paired as in the case of crystallization in small molecules. Since such equilibrium crystals are never formed, T_{Mo} has to be estimated by extrapolation. The surface nucleation theory also provides an estimate for T_{Mo}, based on the assumption that the difference between the crystallization and melting temperatures is due to the thickening of lamellae at the crystallization temperature:

$$T_m = T_{cryst} + \Delta T[1 - \frac{1}{1+\zeta}] \tag{1.6}$$

where ζ depends weakly on the subcooling. This forms the basis for the Hoffman-Weeks method whereby a plot of the melting temperature against the crystallization temperature (determined by differential scanning calorimetry experiments) can be conveniently used to determine the equilibrium melting point. This method provides an underestimate for T_{Mo} since Hoffman-Weeks plots are experimentally observed to be nonlinear at low subcoolings (Figure 1.5).

1.1.3 Flow Effects on Polymer Crystallization

While quiescent crystallization has been explored reasonably well and detailed models have been developed for it, the strong influence of imposed flow fields on the kinetics and morphology of polymer crystallization is poorly and incompletely understood. Polymer melts and solutions show viscoelastic behavior upon imposition of stresses or flow fields. Since stresses in high polymers relax over macroscopic time scales, at the temperatures at which they are typically processed, readily accessible deformation fields lead to an easily measurable distortion of the polymer chain from its random coil, isotropic equilibrium configuration. Semicrystalline polymers crystallize from these distorted chain configurations under typical processing like conditions. Preferential orientation of chain segments in the flow direction leads to "flow-enhanced" crystallization; the crystallization kinetics and semicrystalline morphology into which the polymer crystallizes are different from quiescent crystallization. The effect of flow on the crystallization process strongly depends on the extent to which the equilibrium chain configuration can be perturbed, and thus on the processes and time scales of stress relaxation in the polymer. Relaxation processes in polymers are highly dependent on the architecture of the macromolecule. For example, changing the topology of the molecule from linear to long-chain- or star-branched changes the scaling of the relaxation time with molecular weight from a power law to an exponential[34,35] (Figure 1.6). Consequently, chain architecture has implications for crystallization rates, total crystallinity and morphology under flow conditions and adds richer detail to the crystallization phenomenon. While this provides us with a handle with which to tune the microstructure and material properties, it also complicates crystallization studies and modelling.

Intensive research has gone into trying to understand flow enhanced crystallization over the last few decades. The contribution made by this work can be appreciated in the context of the background provided by a brief literature review (in the following chapters, the literature is re-examined and aspects germane to the topic of the chapter are highlighted and discussed is greater detail). The literature is replete with studies of samples extruded into standard "dog-bone" type test geometries, fiber spinning and film blowing experiments, etc., which have built up an enormous bank of knowledge regarding the effect of specific, commercially important types of flows on microstructure development (see, for example, the review by Peterlin[36] on drawing of semicrystalline polymer fibers). However, the complicated flow and thermal histories in these experiments makes it difficult to elicit details of the fundamental processes that govern flow enhanced crystallization, and thus, developing models of crystallization based on such experiments is not possible.

A vast literature that examines flow enhanced crystallization under better defined conditions also exists; researchers have used a variety of rheometers, extruders and custom-built equipment to impose well defined thermal and flow histories and monitored the development of crystallinity by tracking optical signals, rheological signatures, dilatometric data, etc. A brief, non-exhaustive summary of the most widely cited references that fall under this category is presented in Table 1.2. Flow generally enhances crystallization kinetics and severe flow conditions lead to anisotropic morphologies. However, it is difficult to derive any deep insights into the mechanisms of flow enhanced crystallization beyond these simple qualitative conclusions, since most of the experimental results convolute the effects of flow and thermal history on nucleation and growth. The use of different experimental protocols (continuous flow vs. brief intervals of shear, isothermal vs. nonisothermal, etc.) makes it difficult to compare the studies. Thus, when the findings of different studies disagree, it is not easy to identify the source of the discrepancy. Further, most of the studies do not provide detailed characterization of the molecular characteristics of the polymers studied (such as molecular mass polydispersity, copolymer content, branch content, tacticity, etc.). Also, the effects of flow on polymer crystallization being highly nonlinear, it is uncertain how some of the results of experiments done at low shear rates or shear stress or total strain will generalize to processing-like conditions. Thus, there is a need for definitive experiments with well characterized samples, under "clean" experimental conditions that eliminate thermal transients and gradients and impose a well defined and controlled flow history accessing stress levels comparable to those encountered in processing flows.

In this thesis, we describe the development of novel, powerful experimental tools that deconvolute the effect of flow from that of thermal transients or gradients, while allowing us to monitor transient structure development at a variety of length and time scales of interest. Experiments can be done with relatively small sample quantities ($\sim$ 500 mg/experiment), thus opening up studies of experimental resins or model materials that can now be synthesized due to advances in chemistry, but are available only in gram level quantities. We describe the results of our studies with a commercial polydisperse isotactic polypropylene resin: *in-situ* turbidity and birefringence with visible light and synchrotron X-ray scattering are described and analyzed along with structural information gleaned from *ex-situ* microscopy. Our investigations establish conditions that lead to the development of oriented morphologies, and shed light on the pathways that lead to their formation. This work suggests that the melt relaxation spectrum of the polymer melt might play an important role in anisotropic structure development in flow enhanced crystallization, and opens up avenues to experiments with model materials to resolve the issue.

In the next section, we discuss the objectives of our studies by examining the technological implications of an improved understanding of flow enhanced crystallization.

1.2 Objectives

Flow enhanced crystallization is governed by the interplay of the rheological and crystallization time scales that dictate phase-transformation kinetics and morphological development.[4] The physics of formation of macromolecular ordered structures, under the influence of flow, depends on molecular relaxation processes that determine chain

Research group	System	Flow device	Measurement	Conclusions
Haas, Maxwell[37]	PE, PB	s||p	σ, γ	Crystallization accelerated above critical σ
Kobayashi, Nagasawa[38]	PE	Couette	η, σ	Molecular orientation: anisotropy, rapid cryst.
Mitchell, Meier[39]	R	SIC	Excess ΔT	Cryst. rate independent of elongation
Wereta, Gogos[40]	PB	s||p	σ, γ	Flow: lower induction time and rapid cryst.
Ulrich et al.[41,42]	PEO	r||p	OM, Dil.	Flow: higher nucleation (nuc.) density
Stein et al.[43,44]	PE	SIC	Δn, SALS	Quantitative optical methods for cryst.
Sherwood et al.[45]	PEO, PϵC	Couette	Dil.	FIC is nucleation controlled Enhancement due to chain orientation
Lagasse, Maxwell[46]	PE, iPP	s||p	σ, η	MW-dependent critical shear rate, $\dot{\gamma}$ No effect of inert fillers; nuc. agents enhance cryst. kinetics only at low $\dot{\gamma}$
Andersen, Carr[47]	PE	r||p	Δn, Torque	Effect of MW distr. important for FIC
Wolkowicz[48]	PB	s||p	OM	Nuc. density increased, not growth rate
Yeh[49,50]	R, PE	SIC	TEM	Fibrillar nuclei limited in length
Monasse[51]	PE	s||p	OM	Nuc. & growth enhanced; Nuclei $\perp$ flow initially
Tribout et al.[52]	E-co-P	s||p , FP	OM, Δn	Enhanced nuc., growth, mechanism like quiescent
Mc Hugh et al.[53–56]	PE, iPP	4-RM, s-FG etc.	Δn, Turbidity	Amorphous crystallization precursor; Critical γ Weaker T dependence than nucleation theory Nuclei persist above nominal melting point
Vleeshouwers, Meijer[57]	iPP	CP	Modulus	Effect of flow only on high MW polymers At constant γ, more effective to increase $\dot{\gamma}$
Janeschitz-Kriegl et al.[15,58–61]	iPP	Extruder	Δn	Cryst. controlled by $\dot{\gamma}_w^{-2} t_s{}^{-1}$ Synergistic effects with nuc. agents Phenomenological theory for oriented "skin"

Table 1.2: Summary of experimental studies of flow enhanced crystallization. PE, PB, iPP, PEO, E-co-P, PϵC, R stand for polyethylene, poly(1-butene), isotactic polypropylene, polyethyleneoxide, ethylene-propylene copolymer, poly(ϵ-caprolactone) and natural rubber respectively. s||p and r||p are sliding and rotary parallel plate; FIC, SIC, FP, 4-RM and s-FG stand for flow induced and strain induced crystallization, fiber pullout, 4 roll mill and solution fiber growth experiments respectively. $\sigma, \gamma, \eta, \Delta$n, OM, TEM, SALS and Dil. stand for shear stress, strain, viscosity, birefringence, optical and electron microscopy, small angle light scattering and dilatometry respectively.

deformation by the imposed flow, and on the crystallization route from this distorted initial state. Thus, to obtain a complete picture of the crystallization process, it is necessary to be able to monitor deformation and structural evolution right from the initial stages and over all the length scales of ordering. Therefore, a combination of *in-situ* and *ex-situ* techniques that characterize the details of morphological structure needs to be employed. Ultimately, the understanding that would result from such studies might enable rational process design and materials selection to tunably engineer products with exceptional properties, close to their theoretical limit.

Examples of semicrystalline materials with highly optimized material properties resulting from superbly "bio-engineered" processing strategies and materials abound in nature. Biomaterials such as spider silk have been perfected through evolution to have a highly desirable combination of tensile strength and toughness that cannot be matched even by sophisticated modern high performance fibers such as Kevlar.[62,63] Studies[64] of the supramolecular semicrystalline structure of the alanine sequences that make up spider silk reveal that the exceptional material properties result from a bimodal population of crystals, one with a very high degree of orientation leading to a high modulus along the fiber direction and another that shows very weak orientation that reinforces the fiber and gives it significant compressive strength. Recent studies[65–67] of the glands that secrete, store and spin silk in spiders as well as of the process of spinning suggest that the semicrystalline microstructure in spider silk is controlled by the spider's manipulation of elongational flow rates as a pre-oriented, low viscosity liquid crystalline feedstock is spun through a duct with a hyperbolic geometry to orient the molecules while being treated to a low pH environment to assist the folding of the silk proteins. This level of exceptional control over morphology, however, remains beyond the reach of engineers currently and considerable progress needs to be made before we can understand or mimic such materials.

Less esoteric but commercially important applications such as improving the transparency of semicrystalline polymer films[68–70] (important for packaging applications) or reducing the wall thickness in molded parts[5,71] (driven by environmental concerns about the increased usage of non-biodegradable plastics and to decrease cycle times) using novel resins has led to a resurgence of interest in understanding the fundamentals of flow enhanced crystallization. An improved ability to manipulate crystallinities at the end of processing as well as microstructure might also make it possible to use biodegradable thermoplastic polymers such as polylactides and polyhydroxybutyrates which are currently limited[72,73] by their poor processability, narrow processing window and low levels of crystallinity.

This thesis is aimed at developing a deeper understanding of the fundamental processes that control crystallization of polymers subject to the imposition of flow fields. Well controlled and characterized experimental conditions are used in conjunction with a wide range of *in-situ* and *ex-situ* characterization techniques to monitor the development of structure from the earliest stages of crystallization, and to explore the influence of thermodynamic factors and kinetic pathways on nucleation and crystal growth.

1.3 Thesis Organization

The thesis starts with an introduction to the experimental methods and techniques that we have adopted to examine shear enhanced polymer crystallization. In the next chapter, we describe an instrument that we have developed for rheo-optical and rheo-(X-ray scattering) investigations. Our approach is contrasted with others in the literature, and the advantages of our novel device are explained.

In Chapters 3-6, we present the results of our investigations on a polydisperse industrial isotactic polypropylene. In Chapter 3, we describe *in-situ* rheo-optical observations and *ex-situ* optical microscopy that map out the effect of different shear treatments on crystallization kinetics and morphology. In Chapter 4, we describe how "extreme" shear conditions provide a kinetic pathway for nucleation of anisotropic crystallites. The structure of these crystallites are explored in detail using X-ray scattering and electron microscopy in Chapter 5. In the last chapter, X-ray scattering data is analyzed thoroughly, in light of the *in-situ* optical and *ex-situ* microscopy evidence.

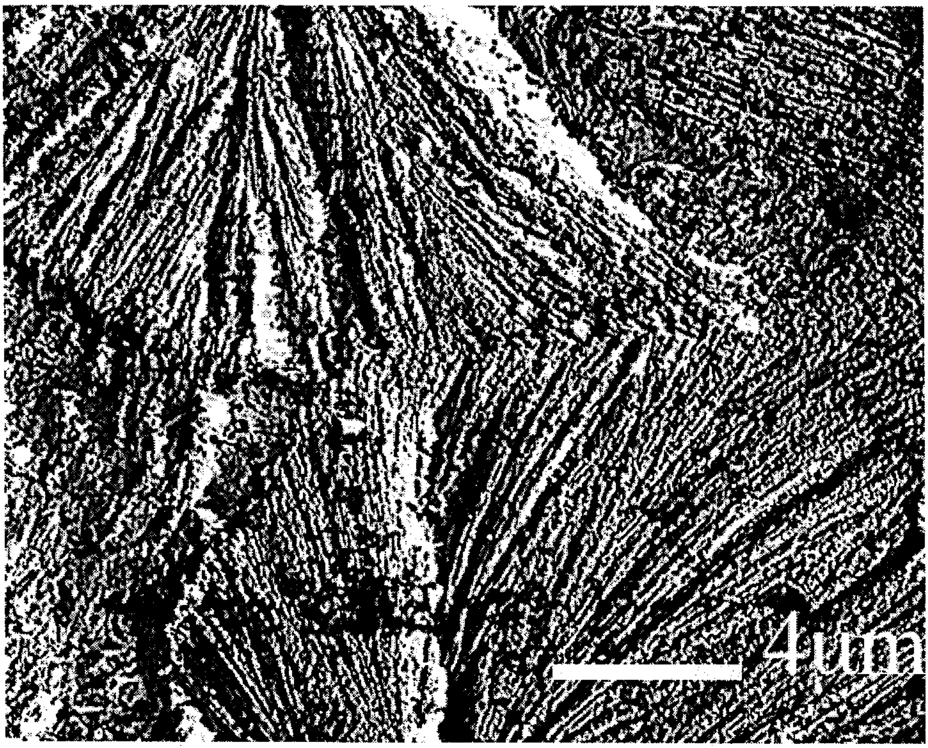

Figure 1.1: Electron micrograph of sheaf like lamellar stack structures in isotactic polypropylene crystallized isothermally at 141°C under near-quiescent conditions.

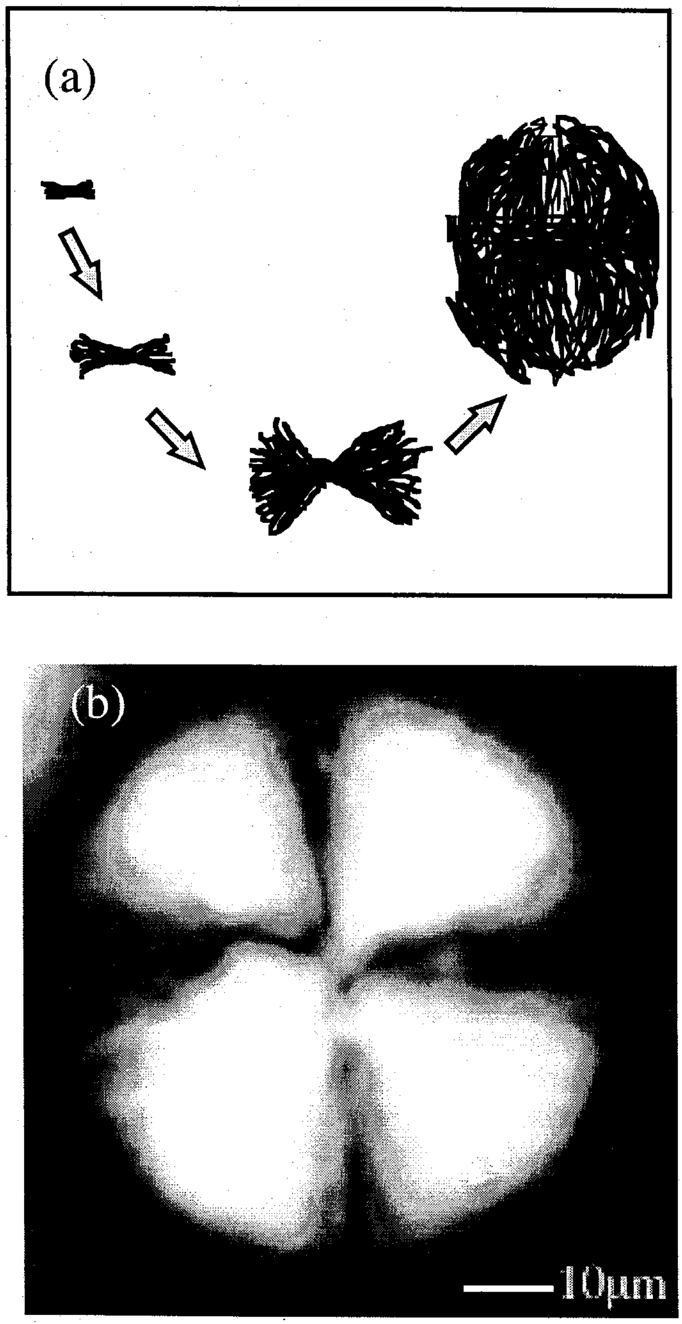

Figure 1.2: (a) Spherulitic growth often proceeds from a stack of lamellae, progressing to form sheaves that splay and finally form a spherical structure. In the last stage of development indicated in the figure, the sheaves enclose the "eyes" or "Popoff leaves"; (b) Polarizing optical micrograph of a spherulite of poly(1-butene) crystallized isothermally at 90°C. The familiar Maltese cross extinction pattern is observed.

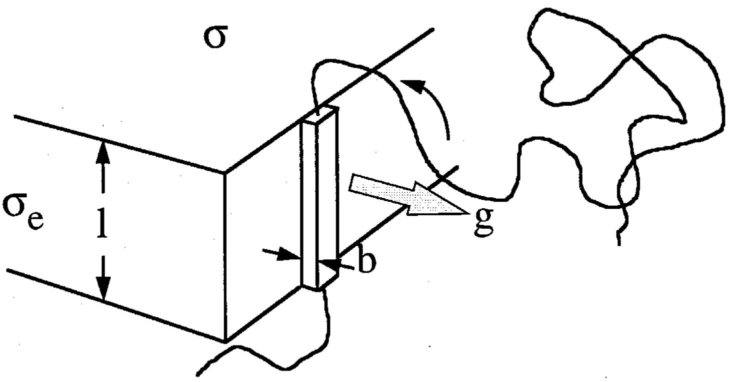

Figure 1.3: Schematic of lamellar growth via the secondary nucleation mechanism postulated by Hoffman and coworkers (see text for details). Polymer chains in the melt are "reeled" in as they accrete on the growing lamella. The thickness of the lamella, l, is determined by the secondary nucleation process; b is the width of the secondary nucleus.

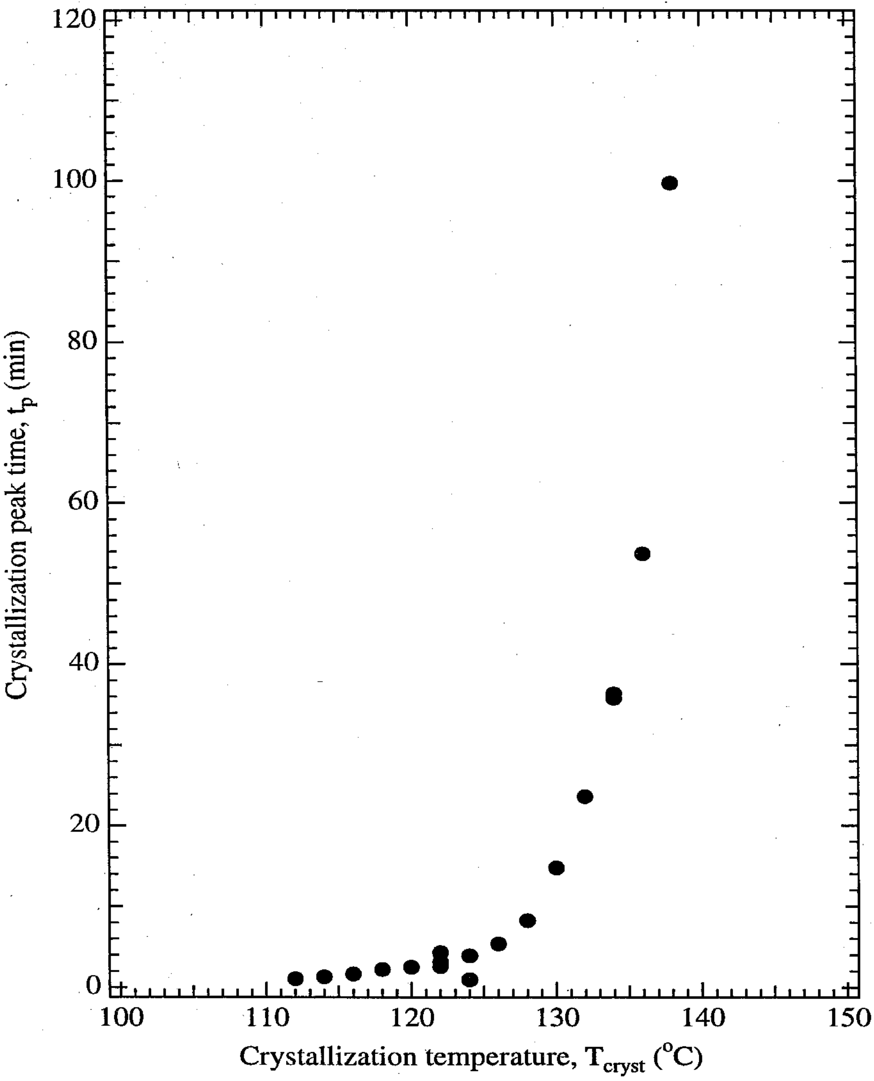

Figure 1.4: Temperature dependence of the crystallization kinetics of an isotactic polypropylene used for most of the experiments in this thesis (PP-300/6) determined by differential scanning calorimetry (DSC). The polymer was held at 210°C for 2 minutes and then cooled to the crystallization temperature, T_{cryst}, where it was held isothermal and allowed to crystallize. The crystallization peak time is determined based on the heat of crystallization evolved as the polymer undergoes a phase change. Temperatures lower than 110°C could not be attained since PP-300/6 would begin crystallizing during the cooldown to T_{cryst}.

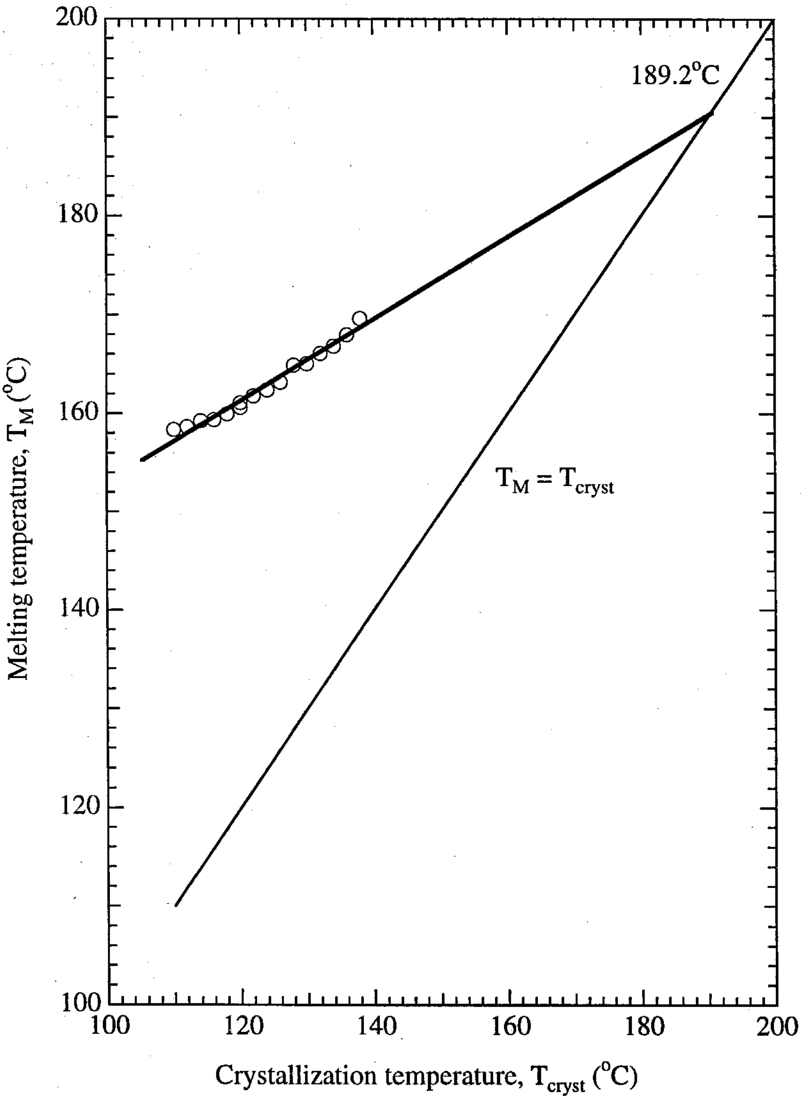

Figure 1.5: Melting points, T_M of PP-300/6, crystallized isothermally at different crystallization temperatures for a long time (~ 5 times the crystallization peak time, t_p at that T_{cryst}) were determined by DSC with a heating rate of 5°C/min. The melting points were then extrapolated to estimate the equilibrium melting point, T_{Mo}, using the Hoffman-Weeks method. As anticipated (see text), the T_{Mo} thus determined (189.2°C) is considerably lower than literature estimates (208°C) from other techniques.

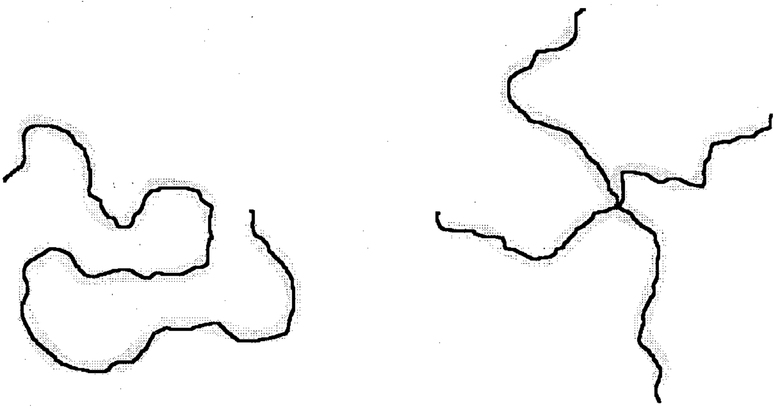

$\tau \sim M^{3.4}$ $\tau \sim e^{M}$

Figure 1.6: The longest stress relaxation time of polymers, τ, is strongly dependent on the architecture of the molecule. Experimental evidence explained by reptation theories[34] show that the terminal relaxation time of a linear polymer has a power law dependence on the molecular weight. For a star polymer, this changes to an exponential dependence on the arm-length of the molecule.

Bibliography

1. Mandelkern, L. *Crystallization of Polymers,* McGraw-Hill, NY: 1964.
2. Wunderlich, B. *Macromolecular Physics,* volume 1, 2 and 3 Academic Press, NY: 1976.
3. Bassett, D. *Principles of Polymer Morphology,* Cambridge University Press, Cambridge: 1981.
4. van Krevelen, D. *Chimia* **1978,** *32,* 279.
5. Kaplan, W. A., Ed.; *Modern Plastics Encyclopedia,* McGraw-Hill, NY: 1998.
6. Graff, G. *Modern Plastics* **1998,** *73,* 31.
7. McCrum, N. G.; Buckley, C. P.; Bucknall, C. B. *Principles of Polymer Engineering,* Oxford Science, Oxford: 1997.
8. Horton, A. D. *TRIP* **1994,** *2,* 158.
9. Hamielec, A.; Soares, J. *Prog. Polym. Sci.* **1996,** *21,* 651.
10. Coates, G. W.; Waymouth, R. L. *Science* **1995,** *267,* 217.
11. Guan, Z.; Cotts, P. M.; McCord, E. F.; McLain, S. J. *Science* **1999,** *283,* 2059.
12. Lu, B.; Chung, T. C. *Macromolecules* **1999,** *32,* 8678.
13. Ziabicki, A. *Colloid Polym. Sci.* **1974,** *252,* 207.
14. Ziabicki, A. *Colloid Polym. Sci.* **1974,** *252,* 433.
15. Liedauer, S.; Eder, G.; Janeschitz-Kriegl, H.; Jerschow, P.; Geymayer, W.; Ingolic, E. *Intern. Polym. Proc.* **1993,** *8,* 236.

16. Bushman, A.; McHugh, A. *J. Polym. Sci. (Polym. Phys.)* **1996,** *34,* 2393.

17. Doufas, A. K.; Dairanieh, I. S.; McHugh, A. J. *J. Rheol.* **1999,** *43,* 85.

18. Khoury, J.; Passaglia, E. Treatise on Solid State Chemistry. In ; Hannay, N. B., Ed.; Plenum Press, NY: 1976; Chapter The Morphology of Crystalline Synthetic Polymers, pages 335–497.

19. Mandelkern, L. *Polymer J.* **1985,** *17,* 337.

20. Mandelkern, L. *Acc. Chem. Res.* **1990,** *23,* 380.

21. Keller, A. *Phil. Mag.* **1957,** *2,* 1171.

22. Keith, H. D.; F. J. Padden (Jr.) *J. Appl. Phys.* **1963,** *34,* 2409.

23. Keith, H. D.; F. J. Padden (Jr.) *J. Appl. Phys.* **1964,** *35,* 1270.

24. Keith, H. D.; F. J. Padden (Jr.) *J. Appl. Phys.* **1964,** *35,* 1286.

25. Bassett, D. C.; Olley, R. H. *Polymer* **1984,** *25,* 935.

26. Norton, D. R.; Keller, A. *Polymer* **1985,** *26,* 704.

27. Phillips, P. J. Handbook of Crystal Growth. In , Vol. 2; Hurle, D. T. J., Ed.; Elsevier Science, NY: 1994; Chapter Spherulitic Crystallization in Macromolecules, pages 1167–1216.

28. Avrami, M. *J. Chem. Phys.* **1939,** *7,* 1103.

29. Avrami, M. *J. Chem. Phys.* **1940,** *8,* 212.

30. Hoffman, J. D.; Davis, G. T.; J. I. Lauritzen, Jr. Treatise on Solid State Chemistry. In Hannay, N. B., Ed.; Plenum Press, NY: 1976; Chapter The Rate of Crystallization of Linear Polymers with Chain Folding, pages 497–614.

31. Hoffman, J. D.; Miller, R. L. *Polymer* **1997,** *38,* 3151.

32. Turnbull, D.; Fisher, J. C. *J. Chem. Phys.* **1949,** *17,* 71.

33. Hoffman, J. D. *Polymer* **1983,** *24,* 3.

34. Doi, M.; Edwards, S. F. *The Theory of Polymer Dynamics,* Oxford Publications, Oxford: 1986.

35. Larson, R. G. *Constitutive Equations for Polymer Melts and Solutions,* Butterworths: 1988.

36. Peterlin, A. *Colloid Polym. Sci.* **1987,** *265,* 357.

37. Haas, T.; Maxwell, B. *Polym. Eng. Sci.* **1969,** *9,* 225.

38. Kobayashi, K.; Nagasawa, T. *J. Macomol. Sci. (Phys)* **1970,** *B4,* 331.

39. Mitchell, J. C.; Meier, D. J. *J. Polym. Sci. (A-2)* **1968,** *6,* 1689.

40. Wereta, A. (Jr.); Gogos, C. *Polym. Eng. Sci.* **1971,** *11,* 19.

41. Fritzsche, A.; Price, F.; Ulrich, R. *Polym. Eng. Sci.* **1976,** *16,* 182.

42. Ulrich, R.; Price, F. *J. Appl. Polym. Sci.* **1976,** *20,* 1077.

43. Stein, R. S.; Norris, F. H. *J. Polym. Sci.* **1956,** *30,* 381.

44. Stein, R. S. *Polym. Eng. Sci.* **1976,** *16,* 152.

45. Sherwood, C.; Price, F.; Stein, R. *J. Polym. Sci. (Polym. Symp.)* **1978,** *63,* 77.

46. Lagasse, R.; Maxwell, B. *Polym. Eng. Sci.* **1976,** *16,* 189.

47. Andersen, P.; Carr, S. *Polym. Eng. Sci.* **1978,** *18,* 215.

48. Wolkowicz, M. *J. Polym. Sci. (Polym. Symp.)* **1978,** *63,* 365.

49. Yeh, G. *Polym. Eng. Sci.* **1976,** *16,* 138.

50. Yeh, G. *Polym. Eng. Sci.* **1976,** *16,* 145.

51. Monasse, B. *J. Mater. Sci.* **1995,** *30,* 5002.

52. Tribout, C.; Monasse, B.; Haudin, J. *Colloid Polym. Sci.* **1996,** *274,* 197.

53. McHugh, A.; Yung, W. *J. Polym. Sci. (Polym. Phys.)* **1989,** *27,* 431.

54. McHugh, A.; Khomani, B. *Intern. Polym. Proc.* **1990,** *5,* 252.

55. Rietveld, J.; McHugh, A. J. *J. Polym. Sci. (Polym. Lett.)* **1983,** *21,* 919.

56. McHugh, A.; Guy, R.; Tree, D. *Colloid Polym. Sci.* **1993,** *271,* 629.

57. Vleeshouwers, S.; Meijer, H. *Rheol. Acta* **1996,** *35,* 391.

58. Liedauer, S.; Eder, G.; Janeschitz-Kriegl, H. *Intern. Polym. Proc.* **1995,** *10,* 243.

59. Jerschow, P. *Crystallization of Polypropylene: New Experiments, Evaluation Methods and Choice of Material Compositions,* Thesis, Johannes Kepler University, Linz, Austria, 1994.

60. Jerschow, P.; Janeschitz-Kriegl, H. *Rheol. Acta* **1996,** *35,* 127.

61. Jerschow, P.; Janeschitz-Kriegl, H. *Intern. Poly, Proc.* **1997,** *12,* 72.

62. Kaplan, D. L.; Adams, W. W.; Farmer, B. L.; Viney, C., Eds.; *Silk Polymers: Materials Science and Biotechnology,* ACS Symposium Series 544: 1993.

63. Tirrell, D. A. *Science* **1996,** *271,* 39.

64. Simmons, A. H.; Michal, C. A.; Jelinski, L. W. *Science* **1996,** *271,* 84.

65. Willcox, P. J.; Gido, S. P.; Muller, W.; Kaplan, D. L. *Macromolecules* **1996,** *29,* 5106.

66. Vollrath, F.; Knight, D. P.; Hu, X. W. *Proc. R. Soc. Lond. B* **1998,** *265,* 817.

67. Knight, D. P.; Vollrath, F. *Proc. R. Soc. Lond. B* **1999,** *266,* 519.

68. Yuksekkalayci, C.; Yilmazer, U.; Orbey, N. *Polym. Eng. Sci.* **1999,** *39,* 1216.

69. Shibayama, M.; Katoh, K.; Iwamoto, T.; Takahashi, D.; Nomura, S. *Polymer J.* **1991**, *23,* 837.

70. Jar, P. Y. B.; Shanks, R. A. *J. Polym. Sci. (Polym. Phys.)* **1996,** *34,* 707.

71. Bailly, C.; Sederel, W. L. *Makromol. Chem., Macromol. Symp.* **1993,** *75,* 55.

72. Doi, Y. *Microbial Polyesters,* VCH Publishers: 1990.

73. Marchessault, R. H.; *TRIP* **1996,** *163,* 163.

Chapter 2 Instrument Design and Experimental Methods

2.1 Motivation

The macroscopic properties of a semicrystalline material depend on its microstructure: the fraction of crystalline material (the degree of crystallinity) and the morphology[1] (the spatial arrangement, size and orientation distribution of the crystallites). The microstructure of a semicrystalline polymer depends strongly on processing history.[2] Imposing flow fields on a crystallizing polymer melt can accelerate the rate of crystallization and result in the formation of oriented crystallites.[3] Commercial polymer processing operations (such as extrusion, injection molding, film blowing or fiber spinning) subject a polymer melt to intense flow fields (shear, elongational or mixed) and crystallization occurs from the distorted melt.[3,4] The effect of processing on semicrystalline structure is of interest because it has a profound effect on material properties, such as mechanical strength and gas permeability.[5–8] For example, the development of highly anisotropic crystallites during spinning gives certain polymeric aramide and polyethylene fibers a Young's modulus between 80 and 130 GPa in the direction of orientation (compared to 1 to 3 GPa for typical semicrystalline polymers or 200 GPa for steel).[2] Thus, there is a strong motivation to observe structure development in real time during processing.

In spite of intensive research over the past three decades, the fundamental basis of the effects of processing on structure development remains elusive. Processing alters the rate, form and anisotropy of crystallization. These effects are believed to arise through the interplay of flow and thermal history, melt relaxation dynamics and nucleation and growth kinetics. Three requirements for tackling such a complex problem are evident: the need to create a precisely controlled flow and thermal history, the need to monitor structure development in real time, and the need to perform experiments on materials with well-defined molecular structure. The first challenge is to generate a well-defined flow history and deformations that mimic processing conditions and characterize the effects of flow while excluding those of temperature transients and gradients. This requirement has been addressed by Janeschitz-Kriegl and coworkers.[9–12] The second requirement is that of monitoring structure development on scales that range from the segmental orientation distribution in the liquid state, to the nanostructure of the crystalline lamellae and noncrystalline interlamellar material. To probe the effects of local molecular structure (e.g., stereoregularity or comonomer content) and macromolecular architecture (e.g., overall chain length, polydispersity or long-chain branching), well-defined materials with systematic control of these parameters should be studied. Such model polymers can be synthesized, but they are not available on a large-scale. Therefore, instruments that can operate with modest amounts of sample (a few grams) are required.

We have designed and constructed an instrument for observing the kinetics and morphology of crystallization in real time that meets all these criteria. In particular, it enables the application of well defined intervals of shearing with shear stresses up to those typical of industrial processes with continuous monitoring of structural development during and after flow.

2.2 Background

Given the obvious commercial relevance, various aspects of flow enhanced crystallization have been studied by researchers. These experiments can be broadly categorized into three types: (i) investigations that probe the effect of a complicated flow pattern particular to a specific processing geometry on the development of semicrystalline structure; (ii) investigations that use modified rheometers to generate better defined thermal and flow histories but which are typically unable to access processing-like conditions; (iii) studies that examine the effects of well controlled flow and thermal history that can access shear stresses comparable to processing conditions.[9–12]

Ex-situ and *in-situ* investigation[7,8,13–26] of the effect of flows in "practical" geometries (extrusion, spinning) on structure development during crystallization has yielded considerable information on the effects of a particular type of processing flow on the resulting crystallization and material properties of the resin studied. While these experiments provide a direct link between practical processing parameters and structure development, the use of industrial processing equipment necessitates large quantities of sample and limits the range of conditions that can be applied and how well they can be controlled.

Well defined flow histories can be applied by shearing the polymer using modified rheometers in sliding plate, torsional parallel disk, cone and plate or Couette geometries.[27–37] Use of rheometers enabled experiments with small sample quantities under controlled isothermal conditions, but in most cases, the high levels of shear strain and strain rate typical of processing conditions could not be accessed. Further, in all such experiments (except the recent studies of Vleeshouwers and Meijer[37]) the subcooled polymer melt was subjected to continuous shear for the entire duration of the experiment. Thus, flow deformation is experienced by the melt as well as the crystalline entities formed during the experiment. This causes a continuous change in the orientation distribution of the crystallites as they are formed and obscures the relation between the distortion of the melt and the final semicrystalline structure.

Elegant experiments by Janeschitz-Kriegl et al.[9–12] clearly isolated the effects of flow from thermal effects and separated the effects of shear on anisotropic growth from the effects of shear on already crystallized material. Polymer held in a reservoir was injected into a slit die. The die, which was thermally isolated from the extruder, was held at a high temperature to erase the memory of the filling process and then cooled to the desired crystallization temperature (Figure 1). Then the relaxed subcooled melt was subjected to intense shearing at wall shear stresses similar to those in polymer processing operations for a "brief" shearing time (short enough that no detectable crystallization occurred). This experimental protocol generates well defined initial conditions for the polymer melt and a controlled and simple deformation profile. The polymer was allowed to crystallize subsequently and the turbidity and birefringence were tracked to monitor the progress of crystallization. The crystallization temperatures were selected such that the shearing time was always much shorter than the crystallization time, thus minimizing the deformation of already formed crystallites. Since the high pressures used to drive the flow were generated by an extruder, large amounts of sample were required for operation of the instrument. This requirement severely limited the range of polymers that could be studied. Further, the rotating polarizer set-up used for monitoring the birefringence limited the time resolution of their measurements making it difficult to monitor the deformation of the melt during short shearing times.

We have designed a shear device that retains the advantages of Janeschitz-Kriegl's apparatus while adding the capability to work with small amounts of sample. Further, a wide range of experimental probes has been incorporated that allow us to monitor chain conformation in the polymer melt during shear, along with the development of the crystallite nanostructure and the semicrystalline microstructure during crystallization. Our device is designed to accommodate a wide variety of real-time, *in-situ* probes of structure (optical and X-ray) and to facilitate subsequent *ex-situ* characterization by optical and electron microscopies. Like the preceding instrument, our device generates a brief interval of shear by driving the polymer from a reservoir into a narrow slit. Data can be acquired with 5 ms time resolution during the pressure pulse to quantify the conformational distortion of polymers in the melt and relate it to the nature of the subsequent crystallization (viz. the enhanced kinetics and development of anisotropic crystalline structures). Each experiment requires only about 500 mg of polymer. Recent advances in metallocene catalysis have made it possible to synthesize polyolefins with precisely defined molecular architectures and well controlled distribution of molecular weights.[38] The modest sample requirement of our instrument enables studies of these well defined, model polymers and experimental resins that are available only in small quantities.

In the next Section, we present a complete description of the design and operation of our instrument. We discuss the capabilities of the instrument and demonstrate our ability to impose precisely controlled wall shear stresses on the subcooled sample. We then present illustrative results on different isotactic polypropylene resins.

2.3 Instrument design

The design considerations behind our flow cell are driven by the experimental protocol established by Janescitz-Kriegl and coworkers.[9] The desired mode of operation is to fill the flow channel at low injection pressures and high temperatures ($> T_{Mo}$, hold at this temperature to erase melt memory effects, cool quickly to the desired crystallization temperature, apply a controlled wall shear stress and monitor structure development during and after flow. An instrument that can perform this protocol is capable of doing a variety of other experiments, e.g., injecting a hot melt into a cold mold or applying continuous stress during crystallization. In addition, such an instrument could be used to observe transient flow-induced structure in other microstructured polymers, e.g., polymer blends, liquid crystalline polymers or block copolymers.

2.3.1 Flow Cell

To study the effects of shearing time and stress on the subsequent crystallization behavior requires sharp deformation pulses (desired rise and fall times are less than $\sim$ 50 ms), with control over the pulse duration (typically from 250 ms to 8 s) and magnitude (wall shear stresses up to $\sim$ 0.1 MPa). These considerations necessitate a device based on pressure driven flow through a channel (we were unable to design an instrument that provides uniform shear with the required specifications on rise and fall times). The flow channel is machined into an independent component called the "flow cartridge" (C in Figures 2 a,b) to facilitate removal of samples for *ex-situ* analysis and also to provide flexibility in changing to a different flow geometry. Here we use a two-dimensional channel flow geometry because of its simplicity: a rectangular slit with an aspect ratio greater than 10 (width = 6.35 mm, depth = 0.5 mm) is cut into a stainless steel block. The length of the flow cartridge is $\sim$ 63.5 mm which limits the maximum shear strain to 120. Other flow geometries can be easily accommodated by making an appropriate flow cartridge.

2.3.2 Mechanical Assembly

The flow cartridge fits snugly in a large block which serves as a thermal reservoir (called the heater block, H, in Figures 2 a,b). The flow cartridge is held in place during experiments by a stainless steel restraining plate bolted onto the heater block. The restraining plate and the flow cartridge can be removed after experiments, enabling easy sample retrieval for *ex-situ* microtoming and microscopy. The heater block is bolted onto an aluminum block in which a hole (25.4 mm diameter) serves as a melt reservoir (R). The volume of the melt reservoir is significantly greater than that of the flow channel, thereby enabling several "fills" and experiments with a single loading of the melt reservoir.

The high pressure needed to extrude the polymer is transmitted to the melt in the reservoir through a displacement piston. The piston is a stainless steel rod (25 mm diameter) equipped with a high temperature, high pressure lip seal (AS-92071, All Seals Inc., Santa Ana, CA). Pressures at the entrance of the flow channel are recorded through a pressure transducer (PT-462E, Dynisco Measurement Control, Sharon, MA.; range of up to 10,000 psi) mounted flush in the flow channel. Wall shear stresses are calculated from the pressure via a simple macroscopic balance. The displacement piston is driven by a pneumatic actuator. We chose a pneumatic system over a hydraulic system since it is more compact and amenable to transportation to a synchrotron X-ray source.

Four threaded steel rods are coupled using nuts to the extended tie rods at the front of the pneumatic actuator (Hydroline Inc., Rockford, IL) and provide a frame to mount the reservoir block, R. The actuator is held on an optical breadboard using edge clamps and the breadboard is mounted on a heavy table using eight $\frac{1}{4}$-20 bolts. The table is bolted to the floor of the laboratory to damp out vibrations caused by the impact when high pressures are suddenly applied across the cartridge.

2.3.3 Pneumatic Switching System

The pneumatic actuator is driven by a tank of compressed nitrogen gas, and is controlled by a high switching speed solenoid-activated three way spool type valve with a closed cross-over (W7076C6331, Ross Operating Valve Co., Troy, MI). When the valve is switched, gas pressure (set by a laboratory regulator on the nitrogen tank to between 0 and 100 psi, or 0.68 MPa) is generated at the back of the piston in the actuator. Since rapid switching requires a large gas flow rate, which cannot be obtained from a small orifice laboratory pressure regulator, the gas from the regulator is routed to a "surge tank" mounted on the valve. This arrangement also circumvents the problem of time lag for pressure buildup due to the high compressibility of the gas. The 100:1 area ratio of the actuator can be used to generate pressures up to 68 MPa at the end of the actuator shaft (corresponding to a wall shear stress of $\sim$ 0.1 MPa). We did not seek to achieve higher wall shear stresses since most polymer melts undergo slip or melt fracture beyond this value of wall shear stress.[39,40] The rise and fall times for the pressure are less than $\sim$ 50 ms. The solenoid valve is switched open for a controlled duration through a computer equipped with a data acquisition board.

2.3.4 Temperature Control

The strong dependence of isothermal crystallization kinetics on crystallization temperature motivates minimizing the spatial and temporal temperature fluctuations in the flow channel. The temperature in the heater block must be substantially higher than the melting temperature to erase melt memory of the filling process. Thereafter, the heater block must be cooled to the desired crystallization temperature and stabilized before the pressure pulse can be applied. The total time for cooling should be insignificant compared to the crystallization time; it is important that the temperature not drop appreciably below T_{cryst} since that could cause relatively rapid initiation of crystallization. Finally, the spatial temperature gradient between the melt reservoir (which is maintained at a temperature $> T_{Mo}$) and the flow channel (maintained at the crystallization temperature) must be sharp.

To satisfy these requirements, the heater block has a large thermal mass and is equipped with two symmetrically mounted cartridge heaters and also with channels through which a heat transfer oil can be recirculated. The cartridge heaters are regulated through a proportional integral differential (PID) feedback controller (CN76020, Omega Engineering Inc., Stamford, CT) based on the temperature of the heater block H as measured via a thermocouple. The heat transfer fluid (50 cs methyl silicone oil, Nye lubricants, New Bedford, MA) is maintained at the desired crystallization temperature via a high temperature recirculating bath (Model TP-12, Julabo USA, Kutztown, PA). Recirculating the heat transfer fluid through the heater block cools it relatively quickly (in $\sim$ 7-10 mins) from the melt temperature. The long thermal response time has the advantage of providing temporal stability to $\pm 0.1°$C throughout the experiment; however, it limits the range of our experiments, since the quiescent crystallization time must be significantly longer than the thermal response time. The heater block is thermally isolated from the melt reservoir by means of an insulating mica "gasket" (roughly 4 mm thick). The melt reservoir is clad with flexible fiberglass insulation and is heated by four cartridge heaters with independent feedback PID control.

2.3.5 *In-situ* Structural Characterization

A range of morphological probes to characterize the structure development and orientation in the melt is required. Observation ports are cut into the heater block and in the cartridge. Flow cartridges can be equipped with appropriate windows for either optical or X-ray experiments (e.g., quartz windows $\sim$ 4 mm thick or beryllium windows $\sim$ 0.5 mm. The windows are glued on using a high temperature epoxy (526N, Aremco Products Inc., Ossining, NY). An epoxy with a compliant nature was chosen to minimize thermal stresses induced in the windows due to the temperature changes during the experiment.

With this arrangement, real time optical measurements of turbidity and birefringence (indicative of the development of crystallinity and chain orientation, respectively), of the small angle light scattering (SALS) patterns (characteristic of micron-scale lamellar superstructure) and of the wide angle X-ray diffraction (WAXD) and small angle X-ray scattering (SAXS) patterns (characteristic of the unit cell and nanoscale lamellar structures, respectively) can be easily accommodated into our design. For the turbidity and birefringence measurements, the optical train consists of visible laser light (red HeNe, λ = 632.8 nm), a polarizer oriented at 45° to the flow direction, the sample, a polarizing beam splitting prism (10GL08AR, Newport Co., Irvine, CA), aligned at -45° to the flow direction, and two photodiode detectors (PDA50, Thor Labs Inc., Newton, NJ). The intensity of light viewed through crossed polarizers, $I_\perp$, is measured by a photodiode on the beam transmitted through the polarizing beam splitter; the intensity of light viewed through parallel polarizers, $I_{||}$, is recorded by a photodiode on the transverse beam. The sum of these two intensities is used to determine the total transmitted intensity, $(I_{||}+I_\perp)/I_o$, where I_o is the intensity of transmitted light recorded when the sample is fully amorphous. When depolarization due to light scattering is negligible, the average birefringence of the sample, Δn, may be computed from $I_{||}$ and $I_\perp$ using:

$$\Delta n = \frac{\lambda}{\pi d} \arcsin \sqrt{\frac{I_\perp}{(I_{||} + I_\perp)}} \tag{2.1}$$

When the retardation goes over orders, the number of orders accumulated since the cessation of shear is used to determine Δn, since the initial retardation is less than one order in all our experiments.

To account for the differences in the detector gains when calculating the birefringence, a quarter wave plate with its axis along the flow direction is used for calibration at the beginning of each experiment. Care is taken to minimize the amount of stray light incident on the detectors. Neutral density filters are used to avoid saturation of the detectors. The stability of the laser source is unimportant for the birefringence measurements (since Δn involves a ratio of the intensity of light in a particular polarization state to the total intensity). However, the turbidity measurements require a stable light source. The HeNe laser used was determined to be stable to better than 2% over the timescale of our experiments which was adequate for our measurements. While the birefringence measured in our experiments is reproducible with high precision (better than 5%) even at low values of Δn (Δn $\sim 10^{-3}$), the accuracy of the measurements for such low birefringence is limited by the thermal stress induced birefringence in the quartz windows, generated during heating and cooling, and by scattering of laser light off defects on the surfaces of the windows. These can be partially corrected for by subtracting the baseline value of Δn measured at the beginning of an experiment.

Turbidity and birefringence after the onset of crystallization arise due to scattering from crystallites and are sensitive to the size, shape and anisotropy of the crystallites as well as to the difference in dielectric properties between the crystalline and amorphous regions. Thus, while turbidity is not an exact measure of the absolute degree of crystallinity, we use the rate of change of turbidity to provide a qualitative estimate of the rate of crystallization.

The H_V SALS studies use a similar set-up with a polarizer at 45° to the flow direction in front of the sample and a 50 mm diameter sheet polarizer crossed with respect to the first behind the sample. The scattering angle available for measurement of the SALS pattern is maximized by using a polarizer with a large diameter as the analyzer and by positioning it close to the heater block. (To prevent degradation in the quality of the dichroic polarizer due to the high temperature of the heater block, we needed to place it about 3 cm away from H.) A two-dimensional air cooled charge coupled device (CCD) camera (Sensys KAF 0400-G0-L, Photometrics Ltd. Tucson, AZ) with antiblooming electronics was used to acquire the SALS patterns. The data is acquired with a Pentium PC at a time resolution of 2 s.

Our instrument lends itself to easy modification to study the effects of the dynamics of orientation and relaxation of selectively deuterium labelled chains in our sample on the nature of the crystallization process by using polarization modulation infrared (IR) dichroism using an IR laser at the wavelength corresponding to the C-D stretch. The optical train used for these studies has been described previously.[41] This allows us to selectively resolve the effects of a specific species (e.g., by blending in deuterated high molecular weight chains into a matrix of low molecular weight polymer) on flow enhanced crystallization. Finally, the compact design enables transportation of our instrument to a synchrotron source for measurements of the SAXS and WAXD patterns in real time.

2.4 Results and Discussion

We now demonstrate the features of our instrument and illustrate some of the shear enhanced crystallization phenomena with results of selected experiments with three different isotactic polypropylenes. First, we show that the instrument imposes box-like pressure profiles while monitoring the distortion of the melt. Then, we demonstrate how simple optical measurements can be used to monitor the effect of varying shearing durations on crystallization kinetics in a relatively monodisperse polymer. Finally, we contrast the behavior of the narrow distribution material with that of a polydisperse sample and show how kinetic information can be combined with different *in-situ* optical measurements and *ex-situ* microscopy.

The resins used in the experiments include a polymer obtained from Aldrich, "PP-250/3.7" (M_w = 250 kg/mol; polydispersity index, PDI = M_w/M_n = 3.7; melt flow index, MFI = 12 at 230°C/2.16 kg load), a broad polydispersity industrial grade isotactic polypropylene from Quantum Inc., "PP-300/6" ($M_w \sim$ 300 kg/mol; PDI $\sim$ 6-8; MFI= 12 at 230°C/2.16 kg load) from Equistar Chemical and a developmental resin with a well defined linear architecture and relatively low polydispersity from the Dow Chemical company, "PP-186/2.1" (M_w = 186 kg/mol; PDI = 2.1; MFI = 22 at 230°C/2.16 kg load).

2.4.1 Transient Melt Flow

We describe the response of molten PP-250/3.7 to an imposed deformation. The high shear stresses imposed on the polymer melt as it is driven into the slit give rise to nonlinear rheological phenomena during start-up of flow which are manifested as an overshoot in the birefringence (Figure 3). The birefringence, Δn, in the melt is related to the anisotropy in conformation of polymer chains in the melt.[42] The observed value represents an average over the birefringence profile across the shear channel.

$$\Delta n = \frac{2}{d}\int_0^{d/2} [n_{11}(x) - n_{33}(x)]dx \qquad (2.2)$$

where $n_{11} - n_{33}$ is the birefringence in the plane of the flow and vorticity directions, d is the optical path length and x is the co-ordinate measured across the gap. For conditions that are not too far in the nonlinear region (viz. chain stretching that is much less than full extension), Δn is related to the third normal stress difference, N_3 by the stress optic rule.[42]

To examine the flow behavior of the iPP melt, the reservoir and the heater block are both held at 200°C which is well above the nominal melting point for the polymer ($T_{nom} \sim 170°C$). The pressure drop across the slit is around 2000 psi which corresponds to a wall shear stress, $\sigma_w \sim 0.04$ MPa. The pressure has sharp rise and fall times (less than 50 ms), giving a well defined shearing interval. In the case of capillary rheometers with constant piston speed, Hatzikiriakos and Dealy[43,44] have shown that the build-up of the pressure transient is dominated by the compressibility of the polymer melt in the reservoir. Therefore, we checked to see if a similar effect causes the transient in the build-up of pressure in our device. However, since the pressure build-up in our experiments was independent of the amount of polymer in the reservoir, we conclude that compressibility is not an important factor in the pressure transient.

The birefringence (Equation 1) does not increase immediately, and shows an overshoot at around 2 s of shearing (Figure 3). The overshoot in the time trace of the birefringence in our experiments is a manifestation of the overshoot in the third normal stress difference, $N_3 = \sigma_{11} - \sigma_{33}$, since the stress-optic rule holds for these flow conditions.[42] Overshoots in the first normal stress difference, N_1, have been observed upon start-up of shear[45,46] and have been rationalized in terms of the stretching of the polymer chains in the flow. Since the third normal stress difference, N_3, is the sum of N_1 and a relatively small quantity, the second normal stress difference, N_2,[47] we expect the same physics to govern overshoots in N_1 and N_3. Note that the magnitude of the birefringence during shear is approximately $5\text{x}10^{-5}$; values of Δn this small are readily measured using the simple crossed polarizer arrangement.

2.4.2 Crystallization of a Model Polymer

We examine the effects of shearing on crystallization, starting with a low molecular weight and relatively monodisperse resin PP-186/2.1. Shearing significantly increased the rate of crystallization of PP-186/2.1 (Figure 4); however, we have not found conditions that cause highly anisotropic growth. The experimental protocol was as indicated in Figure 1, allowing the polymer to relax at 240°C for 5 minutes and then cooling to T_{cryst} =132°C. Shearing times ranging from 250 ms to 4 s were used and the crystallization kinetics were tracked by monitoring the intensity of light transmitted through the sample. Shearing for short times (less than 1 s) caused a strong acceleration of the crystallization kinetics as indicated by the rapid decrease in the time taken for the transmitted intensity to drop. Shearing for longer times did not show significant further decrease in the crystallization time. These results contrast with the findings of Janeschitz-Kriegl and coworkers on a commercial Ziegler-Natta polypropylene. They observed that the crystallization time scaled with the fourth power of the wall shear rate and the second power of the shearing time ($t_{\frac{\lambda}{2}} \sim \dot{\gamma}_w^{-4} t_s{}^{-2}$). A phenomenological model was proposed[9] to explain this highly nonlinear scaling behavior. Our system does not show the $t_s{}^{-2}$ scaling. We speculate that this might be attributed to the faster relaxation of our low molecular weight sample which might preclude the formation of the long lived "line nuclei" which form the basis of their phenomenological model. Further evidence that "line nuclei" are not developed comes from the absence of an increase in birefringence as the sample crystallizes, suggesting that the crystallites formed are not highly aligned.

2.4.3 Crystallization of a Commercial Resin

The more heterogeneous polypropylene, PP-300/6, shows some qualitatively different responses to shear history, including more dramatic reductions of crystallization time and highly anisotropic crystallization following sufficiently long shearing at high wall shear stresses. The polymer was melted in the reservoir at 200°C while the cartridge was held at 163°C. The polymer was allowed to thermally equilibrate for 5 minutes after being extruded at a low pressure of around 500 psi to fill the subcooled slit. While "true" quiescent crystallization at this low subcooling would take place on the order of days, the polymer melt even in "nominally" quiescent conditions in our experiment crystallizes in a few hours due to the considerable pre-shearing experienced during the low pressure extrusion to fill the flow channel.[48] After thermal equilibration, extrusion was resumed at a pressure drop of 2600 psi (wall shear stress = 0.05 MPa) for four seconds, and the crystallization behavior monitored over a period, t_{cryst} of 2000 s.

Solidification following this treatment produces a very different microstructure in the material near the walls than in the center of the channel. Near the surface (Figure 5a), a highly oriented, densely nucleated structure is observed. At greater depth, the anisotropy decreases abruptly, but the density of nuclei is still high relative to quiescently crystallized material. At the core, the structure is spherulitic. This spatial variation in structure correlates qualitatively with the depth dependent deformation history. The shear rate is highest near the wall (Figure 5b), as is the total strain applied to the material. The deformation rate decreases with position moving toward the center of the slit. At the center, the material is undeformed (the precise velocity profile depends on the rheological properties of the specific material). The shear thinning behavior of the present sample leads to a velocity profile (Figure 5b) that is blunted relative to the Poiseuille flow associated with Newtonian fluids.

In real time we do not have access to depth selective measurements of the structure in the material. Instead, we use information on the final structure to interpret measured quantities that average over the gap. *Ex-situ* analysis of the crystallized sample using optical and electron microscopies as well as X-ray scattering helps us better understand how different structures contribute to the turbidity, birefringence, SALS, etc., and provides a foundation for interpretation of real time depth averaged observations. For example, in interpreting the birefringence observed during flow, it is important to recognize that the signal is dominated by a relatively thin region near each wall, due to the non-linear dependence of the normal stresses on shear rate. Flow-induced changes in the rate of increase in the turbidity of the samples are also dominated by the material near the walls, since the polymer at the center continues to follow quiescent crystallization kinetics. With this spatial heterogeneity in mind, we turn to interpretation of the time resolved measurements of birefringence and turbidity.

Shearing for 4 seconds accelerated the crystallization kinetics by several orders of magnitude and the transmitted intensity fell to half of its initial value in just over 500 s (Figure 6). The birefringence during the pressure pulse (Figure 6, inset) showed the development of an oriented structure which did not fully relax after cessation of shear. This structure was observed only for shearing times greater than 2 s. For shorter shear durations, no such oriented structure was formed during flow and the crystallites formed subsequently were not oriented on a macroscopic length scale. Strongly oriented crystalline structures (as indicated by the behavior of $I_{\perp}$) were formed only when the melt birefringence showed the long-lived feature (Figure 6). Thus the formation of the structure in the melt during shearing correlates with the subsequent growth of crystalline structures oriented on macroscopic length scales. While this increase in birefringence during shearing has been observed by previous researchers,[49] its relationship to subsequent anisotropic structure had not been shown. This clearly demonstrates the need to measure the melt distortion and to use it to interpret the nature of the crystallization process.

2.4.4 Application to Other Materials and Flow Geometries

The results described in this Section focus exclusively on our investigations into the relation between melt flow history and microstructure formation in semicrystalline polymers. However, the small sample requirement of our instrument also opens up studies of model polymers or other materials available only in quantities of grams, and makes it possible to study their behavior under commercial processing-like conditions. The unique ability to incorporate a range of structural probes (with data collection at millisecond time resolution) makes it a valuable tool for the investigation of processing induced structure in a variety of systems such as liquid crystalline polymers, blends and block copolymers. Finally, while we are interested in using simple flow geometries to unravel the physics of flow-enhanced crystallization, the versatile design makes it easy to use complicated flow geometries and impose arbitrary flow fields to investigate processing-structure-property relations in materials under more realistic processing-like conditions.

2.5 Summary

An instrument to study the effects of shearing on the crystallization process in semicrystalline polymers is described. It can impose transient stresses similar to those encountered in polymer processing and provides *in-situ* monitoring of microstructure development during and after cessation of flow. Box-like wall shear stress profiles (rise and fall times under 50 ms with maximum wall shear stress on the order of 0.1 MPa) can be applied for controlled durations. A unique feature of our device is that it accommodates a wide variety of real-time probes of structure such as visible and infra-red polarimetry and light and X-ray scattering measurements. The design also allows us to retrieve the sample for *ex-situ* optical and electron microscopy. Data is acquired with millisecond resolution enabling us to record the extent of shear deformation of the polymer melt during the pressure pulse. Our device works with small sample quantities (as little as 5 grams; each experiment takes ~500 mg) as opposed to the kilogram-quantities required by previous instrumentation capable of imposing comparable deformations. This orders-of-magnitude reduction in the sample size allows us to study model polymers with well defined properties and new developmental resins, both of which are typically available only in gram-scale quantities. The compact design of the shear cell makes it possible to transport it to synchrotron light sources for *in-situ* X-ray scattering studies of the evolution of crystalline structure. Thus, our device is a valuable new tool that can be used to evaluate the crystallization characteristics of resins with experimental compositions or molecular architectures when subjected to processing-like flow conditions. We demonstrate some of the features of this device by presenting selected results on isotactic polypropylenes.

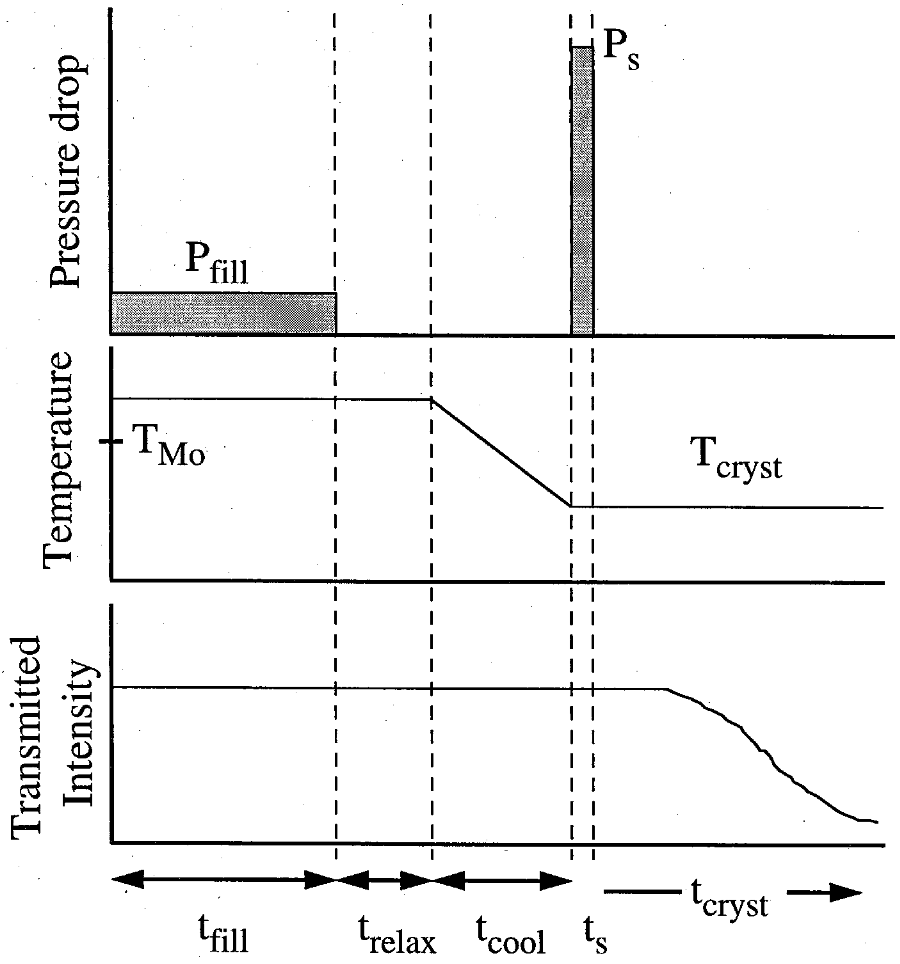

Figure 2.1: Experimental protocol for shear-enhanced crystallization experiments. The polymer melt is extruded from the reservoir using a low pressure P_{fill} for a time t_{fill} (top graph); then it is allowed to relax for time t_{relax} at a temperature that is above the equilibrium melting temperature, T_{Mo} (middle graph). When the polymer melt has relaxed, it is cooled to the crystallization temperature, T_{cryst}, and then subjected to shear as it is extruded at a high pressure, P_s, for a brief interval, t_s. The progress of crystallization with time, t_{cryst}, is monitored using different probes (see text), including turbidity (bottom graph).

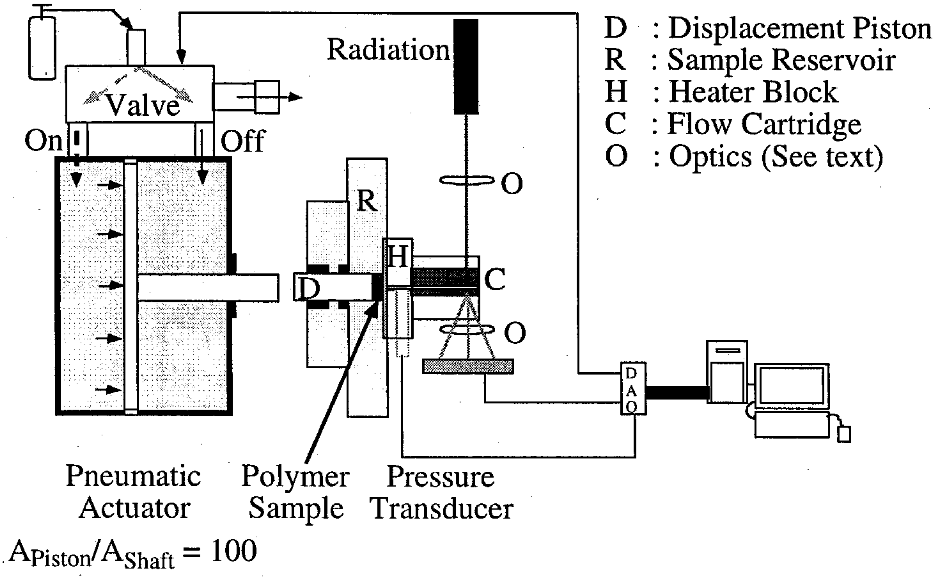

Figure 2.2: (a) Schematic diagram of the shear instrument (see text for details). Feedback controllers for temperature control and relays used to switch the valve are not shown. The recirculating system used for the heat transfer oil to keep the heater block isothermal is also not shown. (b) Isometric view of the reservoir (R), heater block (H) and cartridge (C) indicating how they fit together. Note that H and C are machined in two parts that are assembled together. The reservoir block is mounted to the pneumatic actuator using threaded rods (see text) which pass through the holes indicated towards the corners of R. The heater block bolts onto the reservoir block as shown. The cartridge slides into H and is held in place by a plate that bolts onto the face of H. The perspective shown in part (b) is upside down relative to part (a); the light exits through the conical aperture to permit light and X-ray scattering. Details of the channels for circulating oil through the heater block, mounting holes for pressure transducer, heaters, etc., have been omitted for clarity.

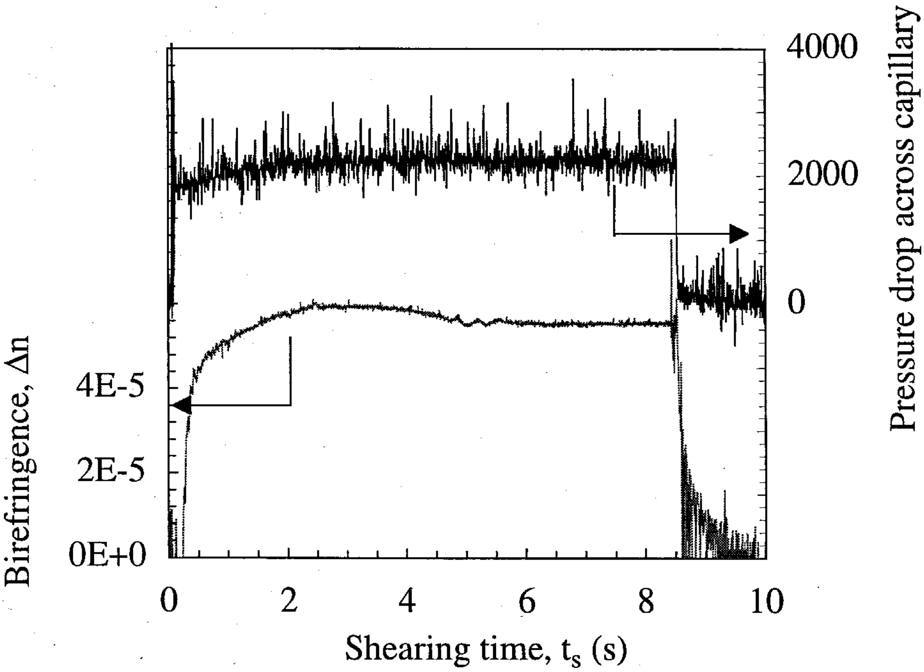

Figure 2.3: Typical shearing experiment for a melt of a commercial isotactic polypropylene, PP-250/3.7, held at 200°C. The rise and fall times for the pressure are on the order of tens of ms. The birefringence shows an overshoot due to the nonlinear viscoelastic response of the melt. Data are acquired with a resolution of 5 ms and are presented without filtering.

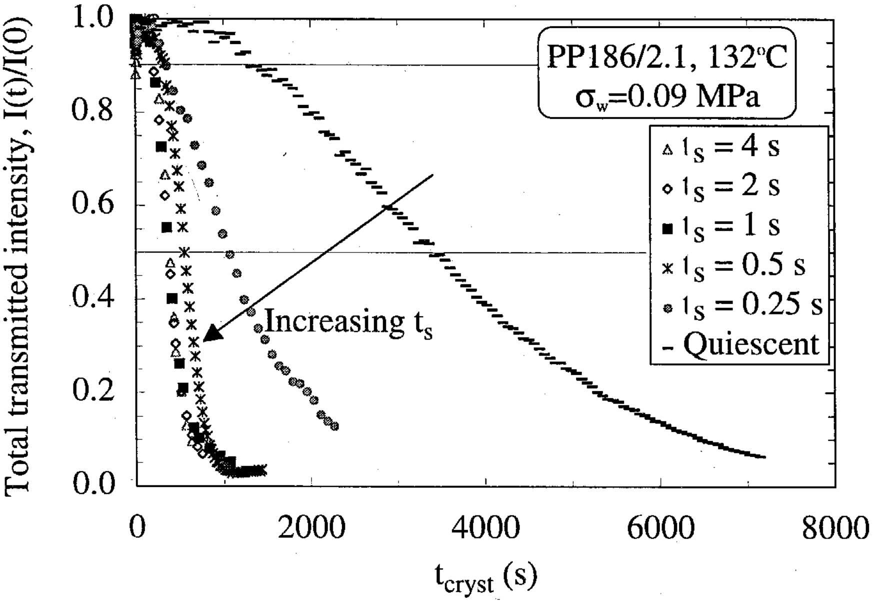

Figure 2.4: Effect of shearing time on the acceleration of crystallization kinetics of PP-186/2.1. A wall shear stress of 0.09 MPa was imposed on the relaxed, subcooled polymer melt at 132°C and the total transmitted intensity was monitored as a function of time. Short shearing times ($t_s < 1$s) dramatically decrease the time required for crystallization. Note that the shortest crystallization times ($t_{1/2} \sim 400$ s) are much longer than the longest shearing time ($t_s \leq 4$ s).

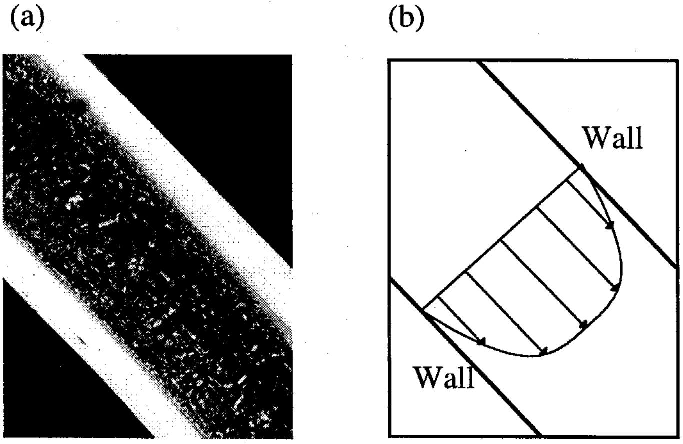

Figure 2.5: (a) *Ex-situ* polarized light micrograph of the cross-section (width = 0.5 mm) of PP300/6 after shearing at a wall shear stress of 0.05 MPa for 4 s. The sample strip runs from upper left to lower right, between the black regions in the lower left and the upper right. The bright regions on each side of this strip have a high birefringence oriented along the flow direction indicative of highly oriented crystallites. The region near the middle of the strip contains spherulites. Thus, shearing has induced formation of a pronounced skin-core morphology. The scattering from the skin dominates the turbidity and birefringence observed in the in-situ optical measurements. (b) Schematic of the relatively blunt velocity profile expected for a shear-thinning polymer melt under pressure driven flow. The velocity profile was calculated by fitting rheological data for PP300/6 to a power law constitutive equation. A no-slip boundary condition was assumed to hold at the walls of the die.

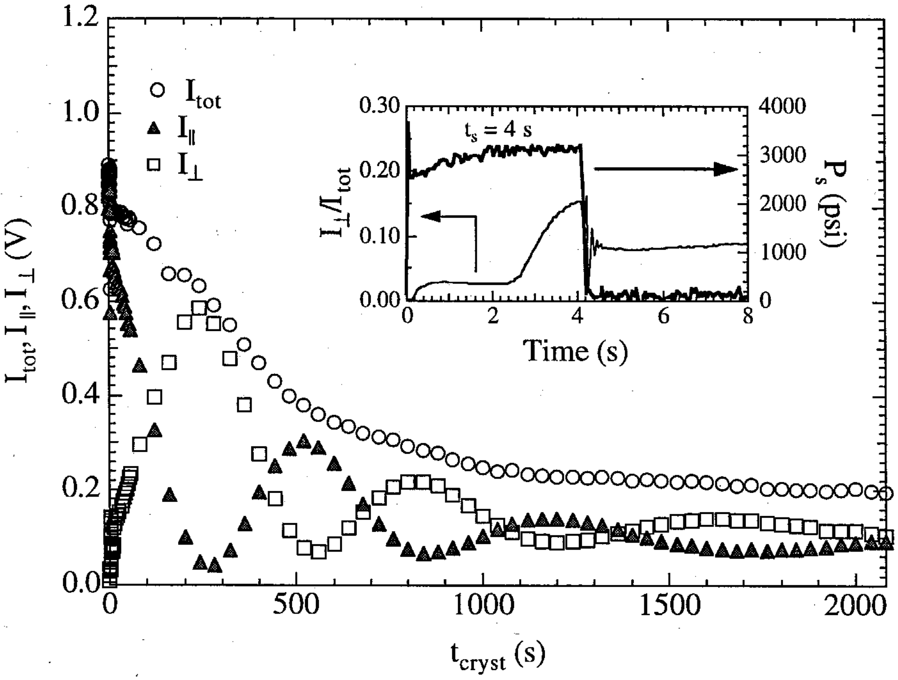

Figure 2.6: Crystallization of a polydisperse isotactic polypropylene, PP300/6 after shearing at a wall shear stress of 0.05 MPa for 4 s. The deformation of the polymer melt during the pressure pulse is monitored (inset). The unusual increase in the birefringence starting at 2.5 s indicates formation of an oriented structure, which does not relax after shear cessation. This is seen to correlate with the formation of anisotropic crystallites.

Bibliography

1. Bassett, D. *Principles of Polymer Morphology,* Cambridge University Press: 1981.
2. van Krevelen, D. *Chimia* **1978,** *32,* 279.
3. Fujiyama, M.; Wakino, T. *J. Appl. Polym. Sci.* **1991,** *43,* 57.
4. Peterlin, A. *Colloid Polym. Sci.* **1987,** *265,* 357.
5. Wang, L.; Porter, R. *J. Polym. Sci. (Polym. Phys.)* **1984,** *22,* 1645.
6. Arvanitoyannis, I.; Tsatsaroni, E.; Psomiadou, E.; Blanshard, J. *J. Appl. Polym. Sci.* **1994,** *51,* 1753.
7. Lopez, L.; Cieslinski, R.; Putzig, C.; Wesson, R. *Polymer* **1995,** *36,* 2331.
8. Ulcer, Y.; Cakmak, M.; Miao, J.; Hsiung, C. *J. Appl. Polym. Sci.* **1996,** *60,* 669.
9. Liedauer, S.; Eder, G.; Janeschitz-Kriegl, H.; Jerschow, P.; Geymayer, W.; Ingolic, E. *Intern. Polym. Proc.* **1993,** *8,* 236.
10. Liedauer, S.; Eder, G.; Janeschitz-Kriegl, H. *Intern. Polym. Proc.* **1995,** *10,* 243.
11. Jerschow, P.; Janeschitz-Kriegl, H. *Rheol. Acta* **1996,** *35,* 127.
12. Jerschow, P.; Janeschitz-Kriegl, H. *Intern. Poly, Proc.* **1997,** *12,* 72.
13. McHugh, A.; Khomani, B. *Intern. Polymer Proc.* **1990,** *5,* 252.
14. McHugh, A.; Tree, D.; Pornnimit, B.; Ehrenstein, G. *Intern. Polymer Proc.* **1991,** *6,* 208.
15. Ulcer, Y.; Cakmak, M. *Polymer* **1997,** *38,* 2907.

16. Phillips, R.; Herbert, G.; News, J.; Wolkowicz, M. *Polym. Eng. Sci.* **1994,** *34,* 1731.

17. Ito, H.; Minagawa, K.; Takimoto, J.; Tada, K.; Koyama, K. *Intern. Polym. Proc.* **1996,** *11,* 363.

18. Hsiung, C.; Cakmak, M.; White, J. *Polym. Eng. Sci.* **1990,** *30,* 967.

19. Huang, H. *J. Appl. Polym. Sci.* **1998,** *67,* 2111.

20. Kalay, G.; Bevis, M. *J. Polym. Sci. (Polym. Phys.)* **1997,** *35,* 265.

21. Saiu, M.; Brucato, V.; Piccarolo, S.; Titomanlio, G. *Intern. Polym. Proc..* **1992,** *7,* 267.

22. Yu, T.; Wilkes, G. *J. Rheol.* **1996,** *40,* 1079.

23. Dees, J.; Spruiell, J. *J. Appl. Polym. Sci.* **1974,** *18,* 1053.

24. Gupta, R.; Auyeung, K. *Polym. Eng. Sci.* **1989,** *29,* 1147.

25. Misra, S.; Lu, F.; Spruiell, J.; Richeson, G. *J. Appl. Polym. Sci.* **1995,** *56,* 1761.

26. Cakmak, M.; Kim, J. *J. Appl. Polym. Sci.* **1997,** *64,* 729.

27. Haas, T.; Maxwell, B. *Polym. Eng. Sci.* **1969,** *9,* 225.

28. Kobayashi, K.; Nagasawa, T. *J. Macomol. Sci. (Phys)* **1970,** *B4,* 331.

29. Wereta, A. (Jr.); Gogos, C. *Polym. Eng. Sci.* **1971,** *11,* 19.

30. Lagasse, R.; Maxwell, B. *Polym. Eng. Sci.* **1976,** *16,* 189.

31. Andersen, P.; Carr, S. *Polym. Eng. Sci.* **1976,** *16,* 217.

32. Andersen, P.; Carr, S. *Polym. Eng. Sci.* **1978,** *18,* 215.

33. Ulrich, R.; Price, F. *J. Appl. Polym. Sci.* **1976,** *20,* 1077.

34. Sherwood, C.; Price, F.; Stein, R. *J. Polym. Sci. (Polym. Symp.)* **1978,** *63,* 77.

35. Wolkowicz, M. *J. Polym. Sci. (Polym. Symp.)* **1978,** *63,* 365.

36. Tribout, C.; Monasse, B.; Haudin, J. *Colloid Polym. Sci.* **1996,** *274,* 197.

37. Vleeshouwers, S.; Meijer, H. *Rheol. Acta* **1996,** *35,* 391.

38. Hamielec, A.; Soares, J. *Prog. Polym. Sci.* **1996,** *21,* 651.

39. Macosko, C. *Rheology: Principles, Measurements and Applications,* VCH Publishers: 1993.

40. Larson, R. *Rheol. Acta.* **1992,** *31,* 213.

41. Kannan, R.; Kornfield, J. *J. Rheol.* **1994,** *38,* 1127.

42. Janeschitz-Kriegl, H. *Polymer Melt Rheology and Flow Birefringence,* Springer-Verlag: 1983.

43. Hatzikiriakos, S.; Dealy, J. *Polym. Eng. Sci.* **1994,** *34,* 493.

44. Dealy, J. *Rheol. Acta.* **1995,** *34,* 115.

45. Menezes, E.; Graessley, W. *J. Polym. Sci. (Polym. Phys.)* **1982,** *20,* 1817.

46. Pearson, D.; Kiss, A.; Fetters, L.; Doi, M. *J. Rheol.* **1989,** *33,* 517.

47. Larson, R. G. *Constitutive Equations for Polymer Melts and Solutions,* Butterworths: 1988.

48. Linear viscoelastic data for PP-300/6 indicates that the time for relaxation of stresses in the melt at T_{cryst} is lesser than the time allowed for thermal equilibration. However, in our experiments, the memory of the high strain distortion experienced by the melt during the initial low pressure extrusion is retained and decreases the crystallization time.

49. Jerschow, P. *Crystallization of Polypropylene: New Experiments, Evaluation Methods and Choice of Material Compositions,* Thesis, Johannes Kepler University, Linz, Austria, 1994.

Chapter 3 Correspondence between *In-situ* Rheo-Optics and *Ex-situ* Structure Determination

3.1 Introduction

Processing of semicrystalline polymeric resins strongly affects their final morphology and consequently their material properties. Semicrystalline polymers are often processed from the melt state. The semicrystalline morphology that develops in the final product, under typical melt processing conditions, is very different from what is observed for quiescent crystallization of the same polymer. For example, the chain extended crystals and the interlocked lamellar structure formed as polyethylene crystallizes under the influence of an elongational flow field yield materials with a very high modulus.[1–3] The high stresses and strain rates experienced by a hot polymer melt as it contacts the cold walls of the die in an injection molding operation can lead to the development of a highly nonuniform "skin-core" morphology. The difference in properties (such as crystallinity and degree of orientation) between the highly oriented crystallites in the skin and the spherulitic core can lead to undesirable effects such as stress whitening, warpage, or in extreme cases, delamination of the skin. On the other hand, the skin can offer desired hardness of the surface. Thus, an understanding of the nature of flow enhanced crystallization with respect to the influence of processing conditions and resin characteristics is required to enable rational design of materials and to optimize properties.

The technological importance of the development of inhomogeneous semicrystalline structure developed during injection molding has driven extensive investigations of test specimens injection molded from various resins under different processing conditions.[4–11] Such studies have yielded a wealth of information regarding the details of processing-morphology relations for particular resins under specific processing conditions. However, the non-isothermal nature of molding and the complicated flow fields imposed makes it difficult to gain insight into the underlying dynamics that lead to the final observed morphology.

To separate the effects of flow from those of temperature transients and gradients present in injection molding, other researchers have used modified rheometers to study shear enhanced crystallization under well-defined flow and isothermal conditions.[12–22] In most of these studies, the polymer melt was subjected to continuous shear at the crystallization temperature and a variety of techniques were used in different studies to monitor the onset and progress of crystallization. The three main conclusions from these studies were: (i) Shear was observed to accelerate crystallization kinetics[12–22] and, under severe conditions, change the semicrystalline morphology from spherulitic to crystallites oriented in the flow direction.[12,13,21] (ii) While researchers recognized the difficulty in separating the process of crystal growth from nucleation,[19] they attributed the enhancement in crystallization kinetics to an increase in nucleation rate caused by distortion of polymer chains in the melt (based on studies of nucleation density,[20] induction time for nucleation[19] and crystal growth rates). (iii) A pronounced effect of molecular weight and molecular weight distribution was observed[15,17,19,20,22] and it was suggested that the high molecular weight species played an important role in melt orientation and the observed enhancement in crystallization kinetics. However, most of the rheometers used for these experiments could not access the high strain and strain rates typical of industrial processing conditions. In addition, the imposition of continuous shear during crystallization changes the orientation distribution of crystallites due to reorientation in the shear field, making it difficult to differentiate between the formation of oriented crystallites and their reorientation due to flow.

A new experiment was proposed by Janeschitz-Kriegl and coworkers[23] in the early 1990's to alleviate some of the limitations in prior experimental approaches. They studied the effect of brief, intense shearing of an isothermal polymer melt (brief compared to the time taken for crystallization) on subsequent crystallization. This approach aimed to separate the effect of primary nucleation (which was assumed to happen mainly during shear) from the growth of crystals at later times. Reorientation of crystallites in the flow field was also minimized. A well defined thermal history was applied and high wall shear stresses were imposed for controlled durations.

In polydisperse isotactic polypropylenes, they found that (i) a brief "pulse" of shear can cause rapid subsequent growth of highly oriented crystallites and (ii) the effect of a shear "pulse" on the crystallization time scaled with the fourth power of the wall shear strain rate and the second power of the shearing time, $\dot{\gamma}_w^{-4} t_s^{-2}$. To explain this scaling, a model with an Avrami-like phenomenology was put forward with an arbitrary shear rate dependence assigned to the nucleation rate and to the growth rate of the crystalline "thread-like" precursors[23] that were assumed to grow from the point nucleation sites generated during shear. The model also explained the weaker dependence of crystallization time on shear rate and shear time for nucleated isotactic polypropylene ($\dot{\gamma}_w^{-2} t_s^{-1}$). Resins with a lower content of high molecular weight chains also showed this weaker scaling, which they could explain by assuming that the number of nuclei is fixed rather than increasing due to sporadic generation during shear.[24] However, while the model is very successful in describing their results, there is no molecular explanation for the nature of the "thread-like" precursors that form the basis of the theory. Finally, it must be noted that $\dot{\gamma}_w^{-2} t_s^{-1}$ is not dimensionless, but is rendered dimensionless in the model by an arbitrary factor, g, having units of time.

Other phenomenological approches to modeling have relied on modifications to the Avrami formalism.[25–28] An early model by Ziabicki[25,26] formulated a general approach to crystallization from an oriented state by modifying the Avrami nucleation and growth rates to be functions of a time dependent "orientation characteristic." Recent work by Mc Hugh and coworkers[27,28] further incorporates concepts of irreversible thermodynamics and employs more accurate rheological models for the amorphous and partially crystalline states. Their model is very sensitive to the coupling between the degree of crystallinity, the orientation of the crystalline phase and the anisotropy of the amorphous phase subject to flow. This model appears promising, but the molecular variables that govern these coupling parameters need to be understood before it can be used predictively.

An earlier "zero-parameter" approach to theoretically explaining flow induced crystallization used the thermodynamic concept of melting point elevation.[29,30] This approach, originally proposed by Flory[29] to explain strain induced crystallization in crosslinked rubbers, relates the reduced entropy of the oriented state from which the polymer crystallizes to an elevation in the equilibrium melting point of the crystal. It was hypothesized that this caused a given temperature to correspond to a deeper subcooling, which causes the observed enhancement in the crystallization kinetics. This theory does not attempt to explain how flow enhanced crystallization often results in the development of oriented semicrystalline morphologies. Further, experimental evidence suggests that the calculated increase in the equilibrium melting point is too small to account for the observed enhancement in crystallization kinetics.[12,31,32] However, Andersen and Carr[17] have suggested that the observed crystallization kinetics may be reconciled with the thermodynamic theory by accounting for the effect of the high molecular weight tail of the chain length distribution on the decrease in entropy upon shearing.

Development of reliable models for flow enhanced crystallization requires experimental data on the earliest events that occur during flow and their relationship to subsequent crystallization kinetics and morphology obtained using a protocol that separates the effects of flow from those of thermal transients or gradients (viz. the protocol developed by Janeschitz-Kriegl and coworkers). Insights into the interplay of flow and crystallization can be obtained by following the development of order at different length scales in real time using *in-situ* probes of structure. In light of Janeschitz-Kriegl's findings and their model, it is of immediate interest to determine the prerequisites for inducing oriented growth: Is there a critical shear stress that needs to be applied? What is the duration for which it needs to be applied? What occurs during flow that leads to subsequent oriented growth? How are the dynamics of these flow-induced events affected by thermodynamic factors (e.g., subcooling) vs.

dynamic factors (e.g., the relaxation spectrum of the melt)? Here we begin to address these questions by examining a polydisperse, industrial isotactic polypropylene sample similar to the one used by Janeschitz-Kriegl and coworkers. We compare our data with the available literature on polydisperse polymers and concentrate on structure development during shear, correlating it with the anisotropic structure development at later times as the polymer crystallizes.

3.2 Experimental

We examine shear enhanced crystallization in a polydisperse Ziegler-Natta isotactic polypropylene, PP-300/6 ($M_w \sim$ 300,000 g/mol, PDI $\sim$ 6-8, pentad content [mmmm] $\sim$ 96%, melt flow index = 12 dg/min at 230°C/2.16 kg load). In all the experiments, polymer melt held in a reservoir maintained at 180°C was injected into a hot, slit die. The die, which is thermally isolated from the reservoir, was held at a high temperature (220°C for 5 minutes)[33] to erase the memory of the filling process and then cooled to the desired crystallization temperature, T_{cryst} (experimental protocol as in Figure 2.1). The crystallization temperature was selected such that the time for quiescent crystallization is much greater than the time required to cool the die (typically around 10 minutes). Care was taken to minimize temperature undershoots during cooling. The stability of T_{cryst} was optimized to only about ± 0.5°C since we found that the sensitivity of our shear enhanced crystallization results to temperature fluctuations was not as high as might be expected from quiescent crystallization studies.

The relaxed, isothermal subcooled polymer melt is subjected to intense shearing at wall shear stresses, σ_w of 0.03 and 0.06 MPa for brief shearing times (short enough that no crystallization is evident from the turbidity measurements). Start-up and cessation of shearing takes $\sim$ 20 ms giving rise to a box-like wall shear stress profile.[34] The polymer was allowed to crystallize subsequently and the turbidity and birefringence were tracked to monitor the progress of crystallization. The wall shear stress, σ_w, is computed from the measured pressure drop across the slit. We do not present our data in terms of a calculated wall strain rate, $\dot{\gamma}_w$, or strain, γ_w, because we do not know how the rheological properties change due to the ordered structure that forms during the shearing time (see Results).

The optical system used for the *in-situ* measurements is the cross polarizer arrangement described in Section 2.3.5. Laser light from a 15mW HeNe ($\lambda = 632.8$ nm) polarized at 45° to the flow direction passes through the sample and is analyzed using a polarizing beam splitter with its axis at -45° to the flow direction (Figure 3.1). Detectors $D_\perp$ and $D_{||}$ measure the intensity of light through crossed and parallel polarizers, $I_\perp$ and $I_{||}$ respectively. The sum of the intensities incident on the two detectors ($D_\perp$ and $D_{||}$) is I_{tot} ($= I_\perp + I_{||}$), the total light transmitted through the sample. The total intensity normalized by the intensity of light transmitted initially through the molten sample, $I_{tot}(t = 0)$, decreases as crystallites that scatter light form. When depolarization can be neglected, $I_\perp/I_{tot}$ is related to the birefringence, Δn (Equation 2.1), and is a measure of the anisotropy in the sample. Depolarization is negligible when little scattering occurs; since the total transmitted intensity never drops significantly during the shear "pulse," Equation 2.1 can be used to describe the orientation of the polymer during flow.

Data is acquired with high time resolution (5 - 20 ms) during shearing to characterize the anisotropy in the melt. After cessation of shear, structure evolution occurs on much longer timescales, so lower data acquisition rates (depending on the characteristic crystallization time) are used subsequently.

At the end of the experiment, the sample was extracted and rapidly quenched by plunging into ice water for *ex-situ* examination. A Reichert UltraCut S Cryomicrotome was used to section the sample at a temperature of -100°C. Sections, 5 μm in thickness, were obtained in the flow-gradient (1-2, axes defined in Figure 3.1) and the gradient-vorticity (2-3) planes for optical microscopy.

3.3 Results

In this Section, we present our results on the shear enhanced crystallization in PP-300/6 as a function of shearing time and wall shear stress. First we examine the effect of shear on the time scale for crystallization, then we describe the development of orientation as determined by our *in-situ* birefringence measurements as the polymer crystallizes. Next, we present *ex-situ* measurements that show how "extreme" shearing conditions (high wall shear stress and shearing time) lead to the development of a pronounced "skin-core" morphology. We will demonstrate that an unusual rheo-optical signature observed *during* short-term shearing correlates with the subsequent formation of anisotropic semicrystalline texture. Finally, we show that the dynamics of creation of this oriented structure during flow is controlled by relaxation dynamics of the melt rather than by the degree of subcooling.

In-situ optical techniques provide information about structure formation averaged over the thickness of the flow channel. Simple rheo-optical measurements such as monitoring the turbidity as the sample crystallizes have been used to follow the progress of crystallization. Shearing PP-300/6 at a wall shear stress of 0.06 MPa at a temperature, $T_{cryst} = 141°C$, accelerates the crystallization kinetics (Figure 3.2), and the sample becomes turbid in a very short time compared to quiescent crystallization. The onset of turbidity is due to the material most strongly influenced by the flow history, typically the material near the walls which experiences the highest shear rate. We define a characteristic crystallization time, called the "half time," $t_{1/2}$, as the time taken for the transmitted intensity to decrease to half its initial value. This half time is not to be confused with the time taken to achieve a degree of crystallinity of 0.5, since the transmitted intensity can drop to zero when only a small amount of material in thin layers near each wall becomes opaque. Further, a given transmittance does not generally correspond to a given degree of crystallinity since it is sensitive to the size and shape of the crystalline scatterers. The crystallization temperature, T_{cryst}, was selected such that $t_{1/2}$ for quiescent crystallization was on the order of a few hours. Upon shearing the melt for $\sim$ 4 s, the half time decreases by about two orders of magnitude (Figure 3.2, inset). As the shearing time is increased, the crystallization time first decreases rapidly and then reaches a plateau at a shearing time of about 5 s (Figure 3.2, inset). The geometry of the shear cell limits us to a maximum strain of about 100 which restricts us to shearing times, $t_s \leq 12$ s for PP-300/6 at this σ_w and T_{cryst}.

As the polymer crystallizes, $I_{tot}(t)/I_{tot}(0)$ drops, $I_\perp/I_{tot}$ rises and $I_{||}/I_{tot}$ falls. Even in the case of unoriented crystallization, multiple scattering gives rise to depolarization manifested in an increase in $I_\perp/I_{tot}$ and a decrease in $I_{||}/I_{tot}$.[35] This change is not indicative of birefringence; it is observed even in quiescent crystallization when the structure is isotropic. For example, as PP-300/6 crystallizes at 141°C after shearing for 2 s at $\sigma_w = 0.06$ MPa, the increase in the normalized intensity between crossed polarizers, $I_\perp/I_{tot}$, occurs mainly after the the total transmitted intensity $I_{tot}(t)/I_{tot}(0)$ drops to less than 0.1 (Figure 3.3 a). Polarized light microscopy with crossed polarizers (PLM-CP) shows that the sample quenched into ice water at the end of the crystallization experiment (viz. when the sample turns completely turbid, $t_{cryst} \sim 1800$ s) contains no visible oriented crystallites and no skin-core texture (Figure 3.4 a,b). Large spherulitic structures, about 40 μm across, are observed in a 100 μm region near the walls in both flow-gradient (1-2, axes defined in Figure 3.1) and gradient-vorticity (2-3) planes while smaller spherulites are observed through the rest of the sample (characteristic of crystallization occurring during the quench).

Qualitatively different behavior is seen in $I_\perp/I_{tot}$ for shearing times longer than about 5 s. For example, when the polymer crystallizes after being sheared for 12 s (at the same T_{cryst} and σ_w), $I_\perp/I_{tot}$ starts increasing immediately (before the total transmitted intensity has dropped by even 10%) and goes through a maximum (Figure 3.3 b). The birefringence going "over orders" indicates the formation of highly oriented crystallites. This is evident in the skin-core morphology observed in the optical micrographs (PLM-CP, Figure 3.4 c,d) of microtomed sections of the sample quenched after it became completely turbid (viz. at $t_{cryst} \sim 400$ s). The micrograph of the sample viewed in the flow-gradient (1-2) plane shows a bright "skin" region near the walls of the die which, when viewed in the gradient-vorticity (2-3) plane, appears dark. This suggests that crystallites having cylindrical geometry are oriented along the flow direction in the skin region. The bright skin region extends to a depth of about 55 μm from the wall. The material appears stratified with a "fine grained" layer (~ 100 μm) between the skin and the isotropic core. Since the shear stress in the sample drops linearly from a maximum at the wall ($\sigma_w = 0.06$ MPa) to zero at the center of the flow channel, the "critical" shear stress at the boundary of the skin and the "fine grained" layer can be calculated to be $\sigma_{crit} \approx 0.047$ MPa.

The central core region exhibits spherulitic structures (Figure 3.4 c,d) which are much smaller than those observed during quiescent crystallization at 141°C (several 100 μm in diameter, micrographs not presented). Near quiescent conditions prevail over the central core, since this polymer exhibits shear thinning behavior that results in a flattened velocity profile.[36] Since the quiescent crystallization kinetics for PP-300/6 at 141°C are known to be slower than the time scale allowed for crystallization in the shear-enhanced crystallization experiments (quenched at $t_{cryst} = 400$ s and 1800 s for $t_s = 12$ s, 2 s vs. 20000 s for quiescent conditions), we infer that the spherulites in the inner core regions (Figure 3.4) formed during the ice water quench.[37]

The enhancement in crystallization kinetics is manifested in the change in $t_{1/2}$ with shearing time, while the development of oriented semicrystalline structures is reflected in the time at which $I_\perp/I_{tot}$ goes through a maximum. The optical signals are indicative mainly of structure formation near the walls of the die, since the polymer there crystallizes before the region near the center as a result of experiencing high shear rate and strain. The initial decrease in $t_{1/2}$ with increasing t_s shows intermediate behavior between the two power laws previously observed for short-term shearing experiments on a similar iPP[23,24] (Figure 3.5). Maxima in $I_\perp/I_{tot}$ during crystallization are observed only for $t_s > 5$ s; in this regime, both the time to reach these maxima, $t_{\lambda/2}$ and $t_{1/2}$, do not change with t_s.

To gain insight into the origin of the differences in the degree of orientation observed in the final crystallized samples, we examine the melt birefringence during shear (Figure 3.6). As the polymer melt is sheared, the isotropic conformation of the macromolecules is distorted giving rise to birefringence,[38] Δn (Figure 3.6, bottom). Since the chain stretching is small relative to full extension under our experimental conditions,[38] the stress-optic rule applies at short times where no crystallization occurs. Under such conditions, the birefringence can be related to the third normal stress difference, N_3 (= $\sigma_{11} - \sigma_{33}$, where 1, 2 and 3 represent the flow, gradient and vorticity directions). The high shear stresses imposed on the polymer in the experiments lead to chain stretching and result in a nonlinear overshoot in N_3, and consequently (see Section 2.4.1) in the observed overshoot in birefringence on start-up of flow (Figure 3.6, bottom). After the initial start-up behavior, polymer melts typically show steady state behavior and N_3 reaches a plateau. Another typical characteristic of melt behavior is that the birefringence relaxes back to zero upon cessation of shear. This is observed for $t_s < 5$ s (Figure 3.6).

Deviations from melt behavior both in the shape of the transient birefringence during flow and its relaxation after cessation of flow are observed with increasing shearing time. There is a transition from transient birefringence characteristic of melt flow to one that has a significant contribution due to long-lived, oriented structures generated during shear. For longer shearing times, the birefringence develops an upturn at times where the melt would show steady-state N_3. This upturn increases monotonically during the shear pulse indicating the formation of an oriented structure which we call the "shear-induced structure."[39] Upon cessation of shear, the birefringence does not decay to zero but drops to a finite value and then increases with time. The development of the upturn in the birefringence during shear, which we associate with the formation of the "shear induced structure," correlates with the development of strong anisotropy manifested by maxima in $I_\perp/I_{tot}$ observed at longer times as the polymer crystallizes and with the formation of a skin-core morphology in the crystallized sample. Real time synchrotron WAXD studies[40] during shear ($t_s >$ 5 s) reveal oriented fiber-like crystalline reflections corresponding to the α-crystalline form of isotactic polypropylene[41] (Chapters 4 and 5).

To examine the wall shear stress dependence of the "shear induced structure," we sheared PP-300/6 at the same crystallization temperature, 141°C, at a wall shear stress, $\sigma_w = 0.03$ MPa (0.03 MPa $< \sigma_{crit}$), for shearing times up to 20 s. The total shear strain experienced by the polymer at the longest shearing times under these conditions (estimated by weighing the polymer extruded during shear) was comparable to the strain experienced on shearing at $\sigma_w = 0.06$ MPa for 12 s. Shearing was again observed to accelerate the crystallization kinetics (Figure 3.7). A smaller overshoot in the melt birefringence (as compared to the experiments at higher σ_w) was observed during start-up of flow (Figure 3.7, inset). No upturn in the birefringence during shear was observed even for the highest shearing time, $t_s = 20$ s, where the instrumental limit of maximum accessible strain = 100 was reached. During crystallization only a very small increase in birefringence was evident in $I_\perp/I_{tot}$ and $I_{||}/I_{tot}$. *Ex-situ* polarized light microscopy of microtomed sections of the sample crystallized after shearing for 20 s showed no evidence of an oriented skin-core structure (Figure 3.8).

3.4 Discussion

Our discussion is organized around the essential and interesting features evident in the behavior of this isotactic polypropylene and their implications in relation to current models of shear enhanced crystallization:

i) There is a qualitative change in behavior with increasing shear stress and shearing time: below a critical stress and shearing time, shear decreases the time for crystallites to form; for $\sigma_w > \sigma_{crit}$ and $t_s > t_{crit}$, shear further induces highly anisotropic growth (skin-core structure).

ii) The effect of shearing time on crystallization kinetics saturates for $t_s > t_{crit}$: further increase in t_s does not significantly reduce $t_{1/2}$ or $t_{\lambda/2}$.

iii) The formation of skin-core morphology correlates with the growth of a birefringent feature ("shear induced structure") during shear.

3.4.1 Prerequisites for Induction of Highly Oriented Crystallization

The effect of flow changes with increasing strength and duration. Initially, application of a short interval of shear decreases the time for crystallites to grow, manifested by the decrease in the turbidity half time (Figures 3.2,3.4). This qualitative behavior is observed at all levels of wall shear stress and at all subcoolings that we have examined. However, this initial change in the rate of crystallization is not accompanied by highly anisotropic growth (Figures 3.3,3.4). *Ex-situ* optical micrographs (PLM-CP) [of sections subjected to a given shear history (σ_w, t_s, T_{cryst})] provide a way to examine the effect of shear stress, since the local shear stress varies linearly from σ_w at the wall to zero at the center. These images show that with increasing stress level at fixed t_s, shearing first appears to increase the crystallite nucleation density; if the shear stress is high enough and the duration long enough, then there is a fairly abrupt transition to highly oriented growth in a region near each wall.

This abrupt transition suggests that there is a critical stress below which highly oriented growth is not observed for a given shearing time. This threshold occurs at approximately 0.047 MPa for the example shown in Figure 3.4 c,d. In accord with this estimate of the threshold stress, when a wall shear stress below this value is used, crystallization occurs at shorter times than quiescent (Figure 3.7), but highly oriented growth is not observed (behavior like that in Figure 3.3a) for any accessible duration of shear (limited by the 100 strain unit maximum for our instrument). The peculiar upturn in the birefringence during shear is also absent (inset, Fig. 3.7). Correlated with the lack of oriented growth, the skin-core morphology is also absent (Figure 3.8). Thus, the development of the "shear induced structure" which correlates with subsequent oriented crystallization is observed only when the wall shear stress exceeds a critical value, viz. $\sigma_w > \sigma_{crit}$ *and* the shearing time exceeds a critical value which is a function of the imposed shear stress, viz. $t_s > t_{crit}(\sigma_w)$.

Requirement of a threshold strain for oriented crystallization has been reported by Mc Hugh and coworkers[32,42] who studied the development of crystallinity and orientation in an HDPE droplet subjected to an elongational ("strong") flow field. An acceleration of the crystallization kinetics by two to three orders of magnitude was observed. *In-situ* measurements of birefringence and dichroism during and after cessation of flow indicated that the orientation developed in the system led to oriented crystallization, provided a critical strain was exceeded. Our experiments with shear flow show an acceleration in crystallization kinetics similar to that observed in these planar extension experiments. Also, the threshold criterion for a critical shearing time is equivalent to the requirement of a threshold strain for experiments done at a fixed shear stress above σ_{crit}. Thus, accelerated kinetics, development of oriented growth and the existence of a "threshold" strain for oriented crystallization are observed both in "weak" shear flow experiments and flow induced crystallization experiments using "strong" extensional flows and appear to be general to different flow fields and polymer systems. Further, the ability to explore different shear stress levels opens the way to examining factors that control the critical strain. Results at $\sigma_w = 0.06$ and 0.03 MPa indicate a very nonlinear dependence of the threshold strain on the stress; the threshold is readily reached at 0.06 MPa, but inaccessible at 0.03 MPa, given our 100 strain unit limitation.

3.4.2 Saturation Behavior of "Skin" Crystallization Kinetics and Morphology

The optical signatures of the flow-induced, oriented growth exhibit an interesting saturation behavior. Once the shearing time exceeds 5 s (at 141°C using $\sigma_w = 0.06$ MPa), longer durations of shear no longer reduce $t_{1/2}$. These durations of shear are long enough to cause sufficiently oriented growth to determine a time at which the retardation reaches $\lambda/2$; interestingly, the saturation behavior for $t_{1/2}$ also holds for the time required to reach a retardation of $\lambda/2$ (Figure 3.5). Both the turbidity and birefringence are dominated by a thin region near each wall (once this outermost layer extinguishes the transmitted beam, the turbidity is insensitive to subsequent build up of scatterers in the interior). The lack of any further decrease of the time scales $t_{1/2}$ and $t_{\lambda/2}$ suggests that the rate and anisotropy of crystallization in the outermost region are no longer sensitive to continued application of shear after some characteristic duration $t_s{}^*$. Saturation of the kinetics and anisotropy of growth in the outermost region alone is not sufficient to explain the constancy of $t_{1/2}$ and $t_{\lambda/2}$; it would further require that the inner regions not produce substantial scattering on the same timescale (even a thickening of the region that contributes to scattering and birefringence would reduce $t_{1/2}$ and $t_{\lambda/2}$ which is not observed). One might speculate on the mechanism that could lead to such saturation behavior; perhaps there is some species that is consumed in producing the thread like precursors, which limits the extent of the flow-induced effect. Alternatively, the crystallites induced during flow might knit together, suppressing further deformation in a boundary layer near each wall, causing it to be insensitive to continued application of stress beyond that moment.

In contrast to the saturation behavior we observe in PP-300/6, Janeschitz-Kriegl and coworkers reported a power-law effect of t_s on crystallization time ($t_{\lambda/2} \sim t_s^{-2}$) throughout the range of conditions they imposed on an isotactic polypropylene of similar molecular weight and polydispersity (Daplen KS10, M_n 52,000 g/mol, M_w 330,000 g/mol).[23] There is evidence that such differences in behavior can result from subtle differences among similar materials. The Janeschitz-Kriegl group compared two different Ziegler-Natta iPP samples, one with M_n = 77,000 g/mol; M_w = 235,000 g/mol and M_z = 545,000 g/mol and the other with M_n = 47,000 g/mol; M_w = 322,000 g/mol and M_z = 1,360,000 g/mol.[24] The latter showed the $t_{\lambda/2} \sim t_s^{-2}$ scaling, while the former showed a weaker scaling ($t_{\lambda/2} \sim t_s^{-1}$ or even $t_{\lambda/2} \sim t_s^{0}$).[43] We do not believe the discrepancy between PP-300/6 and Daplen KS10 is due to the use of $t_{1/2}$ instead of using $t_{\lambda/2}$: in cases where both of these are observed, they follow the same trends as functions of t_s (Figure 3.5). We speculate that the difference between our observations ($t_{1/2}$ decreases initially with increasing t_s but saturates for $t_s > t_{crit}$) may be due to differences in the fraction and length of high molecular weight chains in the sample. It is possible that a molecular weight distribution with a stronger high molecular weight tail could delay the onset of saturation, if saturation is due to "consumption" of high molecular weight chains in the creation of oriented structures. This reiterates the importance of experiments with model systems to quantify the effect of the high molecular weight tail in the molecular weight distribution on shear enhanced crystallization.

3.4.3 Implications Regarding Precursors to Oriented Crystallization

The development of an oriented skin in our *ex-situ* morphological investigations correlates with the formation of oriented precursors during shear evident in the unusual upturn in the *in-situ* birefringence signal upon flow start-up. Here we first discuss two models for flow induced crystallization that each capture the creation of oriented precursors during flow and their connection to subsequent development of oriented morphologies. We then contrast our findings to experimental observations of precursor structures that do not appear to play a role in our system.

The model of Doufas et al.[28] can capture a shear stress overshoot upon startup of shear flow and the monotonic increase that follows. While the overshoot is a consequence of the nonlinear rheology of the amorphous melt, the subsequent upturn in shear stress results from the formation of crystallites. This parallels our observation of overshoot and subsequent upturn in the birefringence: the overshoot coming from the transient third normal stress difference and the upturn correlating with WAXD observations of oriented α-iPP crystallites.[40] However, the behavior in their model is crucially dependent on the choice of the empirical parameter that couples crystallization with amorphous orientation. A rational basis for an a priori choice of this parameter is currently lacking. Nevertheless, the strong nonlinear coupling in the model between crystallization kinetics and the orientation state of the crystallizing melt accords qualitatively with our observation that the emergence of precursors appears to be controlled by the time it takes for the melt to arrive at a given orientation state (Figure 3.9, as discussed below).

A physical (but phenomenological) picture for the generation of the precursors is suggested by the model proposed by Janeschitz-Kriegl to explain shear enhanced crystallization. They postulate the formation of "thread like precursors" during shear which grow with cylindrical symmetry, oriented in the flow direction from point nuclei. We believe that these "thread like precursors" and the lamellae that grow out from them are manifested in the unusual rise in the birefringence and oriented WAXD patterns observed in our experiments *in-situ* during shear for $\sigma_w > \sigma_{w,c}$ and $t_s > t_c(\sigma_w)$.

Amorphous precursors have been observed by McHugh and coworkers[44–46] during studies of seeded flow-induced crystallization of solutions of polyethylenes, isotactic polypropylenes and polyethylene oxide. These liquid like precursors form into oriented fibers for semicrystalline polymers. Since the precursors were also observed during flow of an atactic polystyrene system,[46] it was concluded that they originated from a liquid-liquid phase separation. We have examined the effect of extreme shearing conditions on an atactic polypropylene (M_w = 217,000g/mol, PDI≈2.3, conditions given in[47]). No "shear induced structure" was seen to form suggesting that the birefringent feature we observe does not result from a liquid-liquid phase separation. Keller and coworkers[48] suggest that a coil-stretch transition (at stagnation points in an elongational field, or of polymer molecules adsorbed to the wall in a shear field) is necessary for creation of oriented crystalline structures. Such a transition would have a distinct signature characterized by a rise in the birefringence. Again, our experiments with the atactic sample show no evidence of a coil-stretch transition, which suggests that it is probably not necessary for the formation of an oriented skin layer. The "shear induced structures" seen in our experiments most closely resemble the thread like precursors proposed by Janeschitz-Kriegl.

3.5 Conclusions

We have examined the shear enhanced crystallization of a polydisperse isotactic polypropylene (PP-300/6). Shearing the polymer for a duration much shorter than the quiescent crystallization time at the crystallization temperature always led to significantly accelerated crystallization kinetics as compared to quiescent. However, when shearing above a critical stress was continued for a time greater than a critical duration, the acceleration of crystallization kinetics saturate and a transition to the formation of oriented structures occurs. An oriented, crystalline structure which we call the "shear induced structure" is formed during shear when the wall shear stress is above some critical value and is applied for a critical shearing time. The formation of this "shear induced structure" correlates with the subsequent formation of a skin-core semicrystalline morphology. The time at which the "shear induced structure" appears decreases with temperature at fixed wall shear stress. The time for formation of the "shear induced structure" is governed by the rheology of the polymer melt and not by the subcooling.

3.6 Summary

The effects of "short term shearing" on the subsequent crystallization of a polydisperse Ziegler-Natta isotactic polypropylene are observed using *in-situ* optical measurements and *ex-situ* microscopy. Imposition of brief intervals of shear (0.25 to 20 s, less than a thousandth of the quiescent crystallization time) can reduce the crystallization time by two orders of magnitude (e.g., at 141°C with a wall shear stress of 0.06 MPa). With increasing shearing time, the crystallization time saturates and highly anisotropic growth ensues. This transition to oriented growth correlates with changes in the transient behavior during flow and the semicrystalline morphology observed ex-situ. During flow, we observe the generation of long-lived, highly oriented structures (evident in the transient birefringence) under all conditions that induce subsequent growth of highly oriented crystallites. In turn, the development of oriented crystallites observed *in-situ* after cessation of flow correlates with development of a "skin-core" morphology (highly oriented skin on a spherulitic core) observed ex-situ.

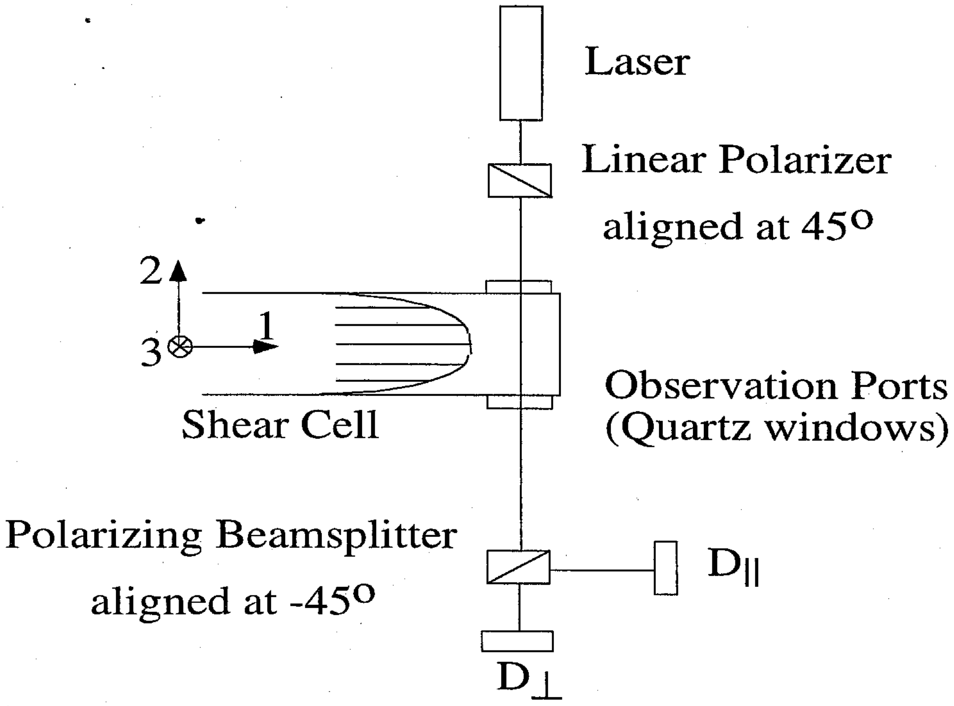

Figure 3.1: Schematic of the optical train used for turbidity and birefringence measurements. P1 is a linear polarizer oriented at 45° to the flow direction; P2 is a polarizing beam splitter. The extraordinary beam from P2 is incident on detector $D_{||}$ which reads the intensity of light through parallel polarizers, $I_{||}$. The through beam is incident on detector $D_{\perp}$ which reads the intensity of light through perpendicular polarizers, $I_{\perp}$.

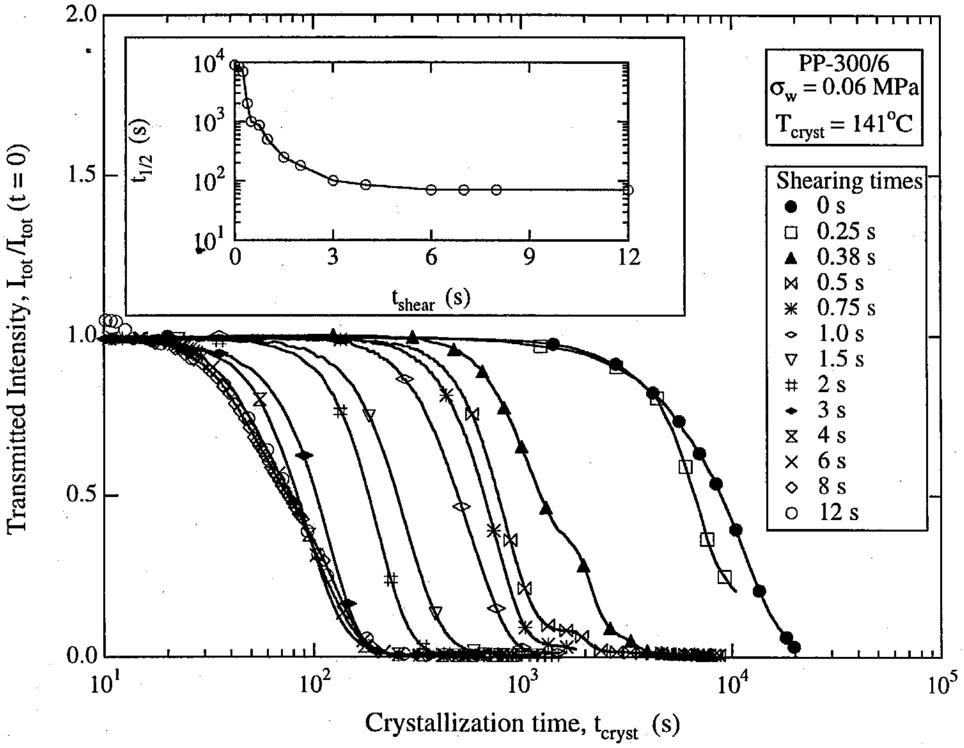

Figure 3.2: Turbidity of PP-300/6 as it crystallizes following a "pulse" of shear at T_{cryst}= 141°C and σ_w= 0.06 MPa for various shearing times, t_s ranging from 0 s to 12 s. The lines indicate experimental data; symbols are sparsely distributed on the lines to identify the experiments at different shearing times. Scattering of incident light as the polymer crystallizes leads to increased turbidity. The crystallization time decreases with increased shearing time, and the crystallization half time, $t_{1/2}$ (see text) reaches a plateau after a shearing time of about 5 s (inset).

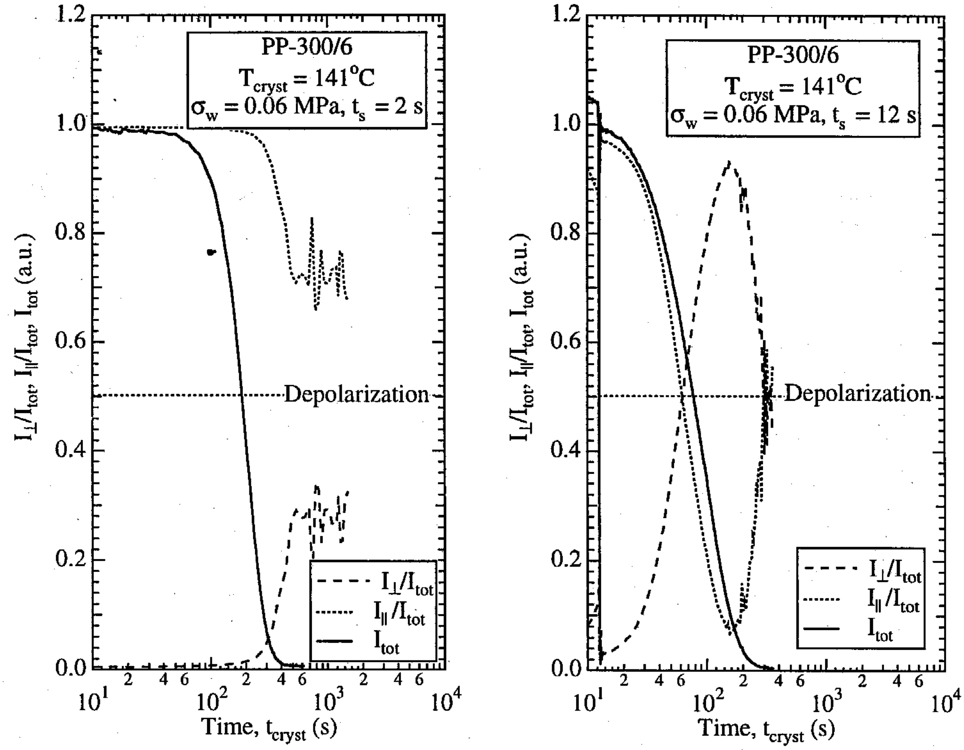

Figure 3.3: (a) Relative intensity through crossed and parallel polarizers for PP-300/6 as it crystallizes following a "pulse" of shear at the same T_{cryst} and σ_w as in Figure 3.2 (T_{cryst} = 141°C, σ_w = 0.06 MPa). t_s = 2 s does not cause a significant increase in the normalized intensity between crossed polarizers, $I_\perp/I_{tot}$ until multiple scattering when the sample becomes very turbid gives rise to depolarization. (b) Longer shearing times (t_s = 12 s) lead to the birefringence going "over orders" indicating the formation of a highly oriented crystalline structure.

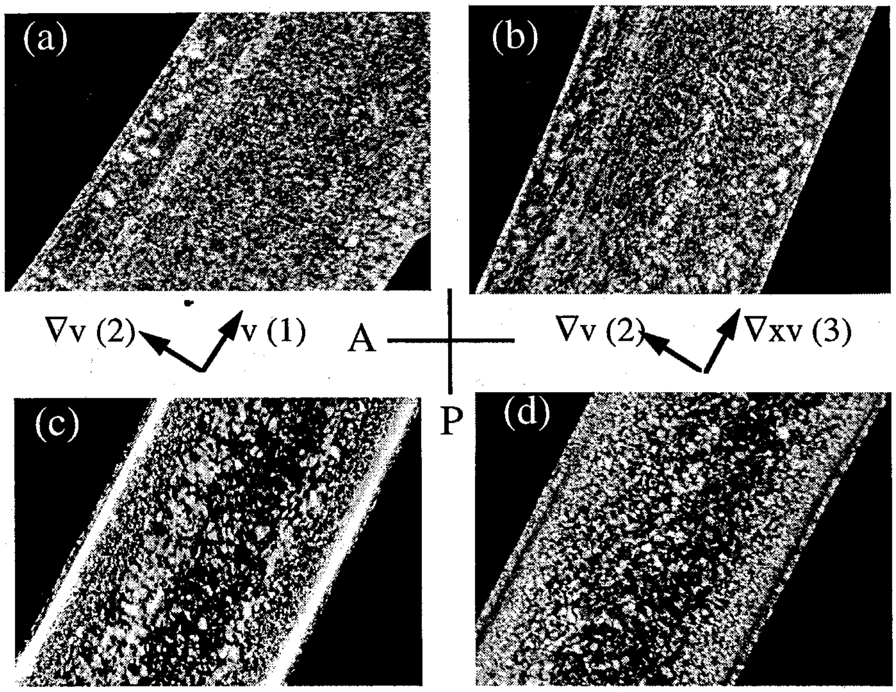

Figure 3.4: Micrographs (PLM-CP) of PP-300/6 crystallized at $T_{cryst} = 141°C$ after shearing at a wall shear stress of 0.06 MPa for $t_s = 2$ s (a and b) and $t_s = 12$ s (c and d) at the same experimental conditions as in Figure 3.3. The polarizer and analyzer directions are at ±45° to the long axis of the sample as indicated. Images on the left show the flow-velocity gradient (1-2) plane, while those on the right show the velocity gradient- vorticity (2-3) plane. After short shearing intervals ($t_s = 2$ s), no oriented structures are visible (a and b). Sufficiently long shearing times ($t_s = 12$ s) induces the formation of a characteristic skin-core morphology. The oriented skin region appears bright when viewed down the neutral direction (c) and dark when viewed down the flow direction (d) indicating that the skin has crystallites with cylindrical symmetry.

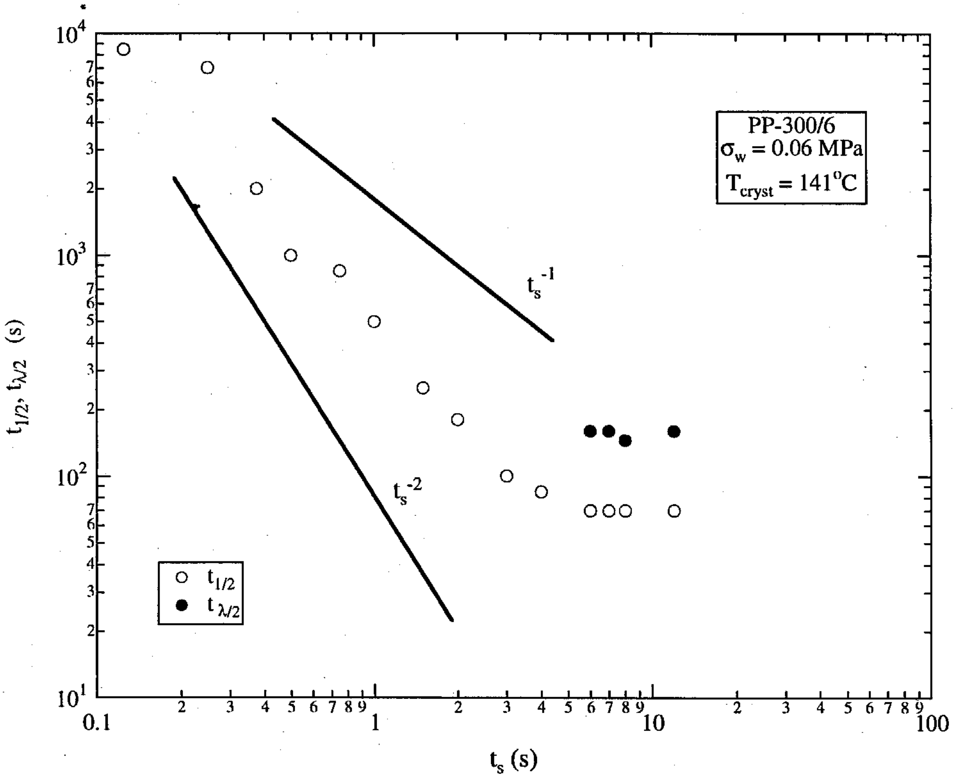

Figure 3.5: Turbidity half time, $t_{1/2}$, and time scale for formation of oriented structures, characterized by the time at which a maximum in $I_\perp/I_{tot}$ develops, $t_{\lambda/2}$ as a function of shearing time, t_s. Note that both these time scales saturate above a critical value of the shearing time, t_{crit}.

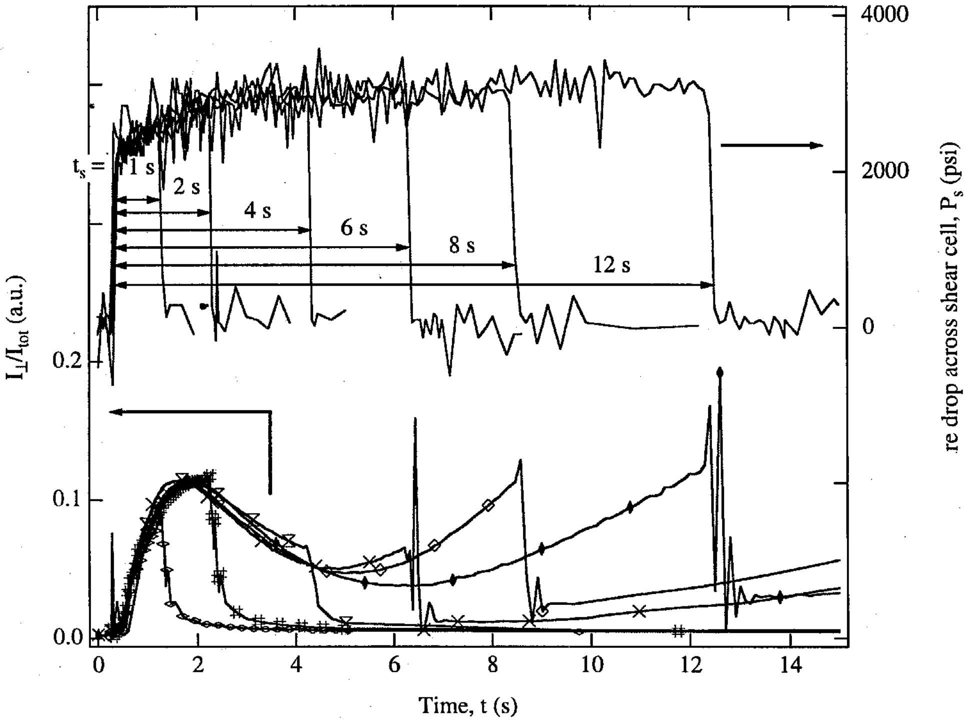

Figure 3.6: Transient intensity transmitted through crossed polars during shear pulses at the same T_{cryst} and σ_w as Figures 3.2-3.5. The top part of the plot shows the pressure imposed across the shear cell to turn the flow on and off. The imposed pressure drop (and corresponding wall shear stress) reaches 80% of the targeted value within 40 ms, gradually reaching the set value over the first two seconds and falls to zero within 40 ms when the actuator is switched off. This provides a good approximation to a "box-like" profile. The bottom part of the plot shows the corresponding birefringence traces for the experiments at different shearing times. The formation of the nonlinear overshoot is evident at about 2 s. Later, at times where a melt would have reached its steady state birefringence. there is a further upturn in the birefringence, which does not relax to zero after cessation of flow.

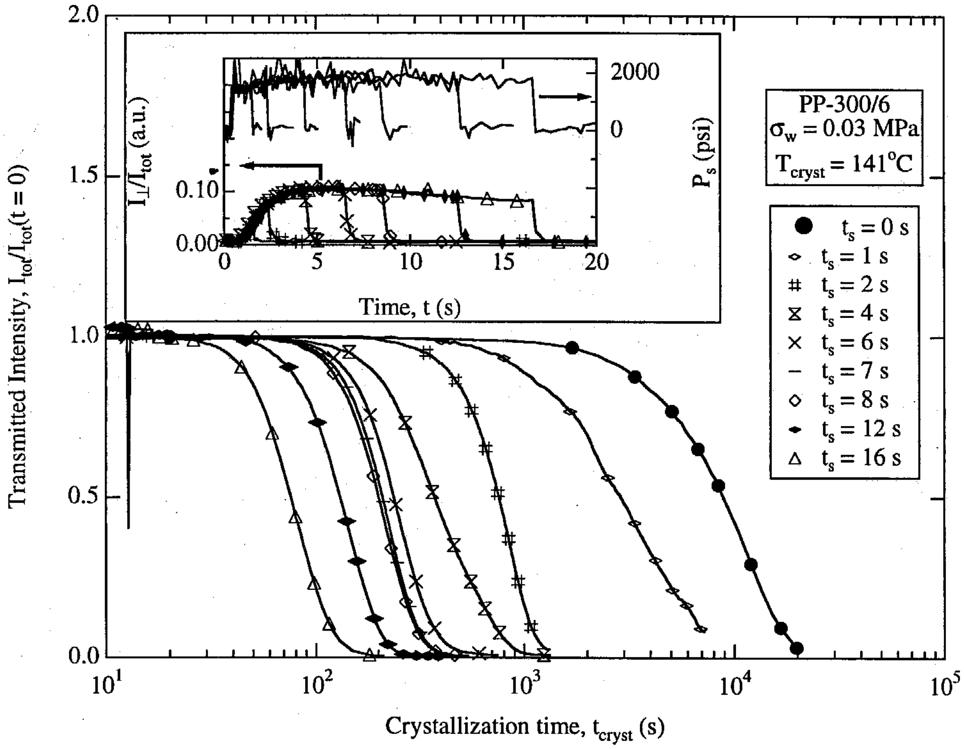

Figure 3.7: Shearing at a lower shear stress (0.03 MPa) at the same temperature (141°C, causes an acceleration in the crystallization kinetics, but no upturn is observed in the birefringence trace during shear (inset).

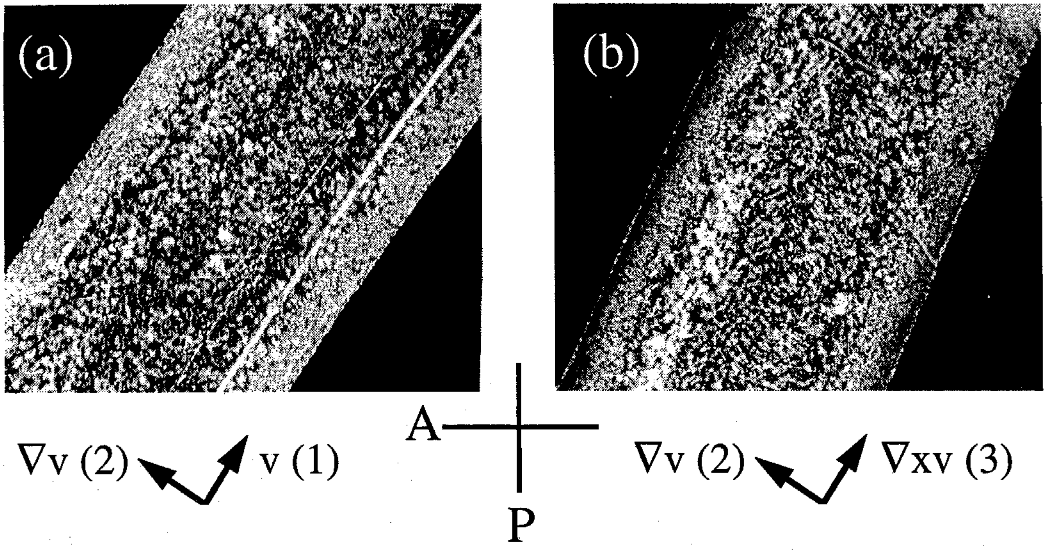

Figure 3.8: (PLM-CP) in the (a) flow-velocity gradient (1-2) and (b) gradient-vorticity (2-3) planes for PP-300/6 sheared at 0.03 MPa at $T_{cryst} = 141°C$ for 20 s.

Bibliography

1. Southern, J. H.; Porter, R. S. *J. Appl. Polym. Sci.* **1970,** *14,* 2305.
2. Odell, J. A.; Grubb, D. T.; Keller, A. *Polymer* **1978,** *19,* 617.
3. Bashir, Z.; Odell, J. A.; Keller, A. *J. Mater Sci.* **1984,** *19,* 3713.
4. Mencik, Z.; Fitchmun, D. R. *J. Polym. Sci. (Polym. Phys.)* **1973,** *11,* 973.
5. Fitchmun, D. R.; Mencik, Z. *J. Polym. Sci. (Polym. Phys.)* **1973,** *11,* 951.
6. Fujiyama, M.; Wakino, T.; Kawasaki, Y. *J. Appl. Polym. Sci.* **1988,** *35,* 29.
7. Fujiyama, M.; Wakino, T. *J. Appl. Polym. Sci.* **1991,** *43,* 57.
8. Isayev, A. I.; Chan, T. W.; Shimojo, K.; Gmerek, M. *J. Appl. Polym. Sci.* **1995,** *55,* 807.
9. Lopez, L.; Cieslinski, R.; Putzig, C.; Wesson, R. *Polymer* **1995,** *36,* 2331.
10. Ulcer, Y.; Cakmak, M.; Miao, J.; Hsiung, C. *J. Appl. Polym. Sci.* **1996,** *60,* 669.
11. Ulcer, Y.; Cakmak, M. *Polymer* **1997,** *38,* 2907.
12. Haas, T.; Maxwell, B. *Polym. Eng. Sci.* **1969,** *9,* 225.
13. Kobayashi, K.; Nagasawa, T. *J. Macomol. Sci. (Phys)* **1970,** *B4,* 331.
14. Wereta, A. (Jr.).; Gogos, C. *Polym. Eng. Sci.* **1971,** *11,* 19.
15. Lagasse, R.; Maxwell, B. *Polym. Eng. Sci.* **1976,** *16,* 189.
16. Andersen, P.; Carr, S. *Polym. Eng. Sci.* **1976,** *16,* 217.
17. Andersen, P.; Carr, S. *Polym. Eng. Sci.* **1978,** *18,* 215.

18. Ulrich, R.; Price, F. *J. Appl. Polym. Sci.* **1976,** *20,* 1077.

19. Sherwood, C.; Price, F.; Stein, R. *J. Polym. Sci. (Polym. Symp.)* **1978,** *63,* 77.

20. Wolkowicz, M. *J. Polym. Sci. (Polym. Symp.)* **1978,** *63,* 365.

21. Tribout, C.; Monasse, B.; Haudin, J. *Colloid Polym. Sci.* **1996,** *274,* 197.

22. Vleeshouwers, S.; Meijer, H. *Rheol. Acta* **1996,** *35,* 391.

23. Liedauer, S.; Eder, G.; Janeschitz-Kriegl, H.; Jerschow, P.; Geymayer, W.; Ingolic, E. *Intern. Polym. Proc.* **1993,** *8,* 236.

24. Jerschow, P.; Janeschitz-Kriegl, H. *Intern. Poly, Proc.* **1997,** *12,* 72.

25. Ziabicki, A. *Colloid Polym. Sci.* **1974,** *252,* 207.

26. Ziabicki, A. *Colloid Polym. Sci.* **1974,** *252,* 433.

27. Bushman, A.; McHugh, A. *J. Polym. Sci. (Polym. Phys.)* **1996,** *34,* 2393.

28. Doufas, A. K.; Dairanieh, I. S.; McHugh, A. J. *J. Rheol.* **1999,** *43,* 85.

29. Flory, P. J. *J. Chem. Phys.* **1947,** *15,* 397.

30. Krigbaum, W.; Roe, R. *J. Polym. Sci. (A)* **1964,** *2,* 4391.

31. Mitchell, J. C.; Meier, D. J. *J. Polym. Sci. (A-2)* **1968,** *6,* 1689.

32. McHugh, A.; Guy, R.; Tree, D. *Colloid Polym. Sci.* **1993,** *271,* 629.

33. The temperature chosen, 220°C, was higher than the Hoffman-Weeks equilibrium melting temperature for PP-300/6, which was determined to be 190°C. Holding at this temperature for 5 minutes was deemed to be adequate to erase melt memory effects since higher temperatures (upto 240°C) or longer holding times did not have any measurable difference on the crystallization kinetics.

34. The rise time is not limited by compression of the polymer in the reservoir, as determined by experiments with various ratios of reservoir-to-capillary volumes (Chapter 2). The time scale is not limited by diffusion of momentum either: the time scale that governs the wall shear stress transient, τ_T, is on the order of w^2/ν, where ν is the kinematic viscosity of the polymer melt, leading to $\tau_T \sim O(10^{-6}s)$ for the present experiments.

35. Ma, Q.; Ishimaru, A.; Kuga, Y. *Radio Science* **1990,** *25,* 419.

36. Nonlinear viscoelastic data obtained using a capillary rheometer indicate that PP-300/6 is shear thinning. Fitting this data to a power law model yields a value of about 0.38 for the power law exponent.

37. Hot stage polarized light microscopy melting studies of quenched sections of PP-300/6 (T_{cryst} 141°C, σ_w 0.06 MPa, t_{shear} 12 s) show that the spherulitic core has a lower melting temperature than the oriented skin. This suggests that the core might have crystallized at a lower temperature than the skin.

38. Janeschitz-Kriegl, H. *Polymer Melt Rheology and Flow Birefringence,* Springer-Verlag: 1983.

39. The trends showed by the birefringence on start up of flow (viz. initial overshoot followed by an upturn) might appear, at first glance, to be similar to those observed in shear stress by Wereta and Gogos[14] (Figure 6) or Andersen and Carr[17] (Figure 5). This is misleading. The steep increase in force and the subsequent decay between 10 and 20 s in Figure 6 of[14] is the viscoelastic reponse of the polymer melt to step strain. Neither the time scale nor the magnitude of the overshoot observed in the rheometer torque in Figure 5 of[17] change with the imposed strain rate suggesting that the overshoot might be an artefact of the experimental setup (repositioning of the polymer, as suggested by the authors). In both these references, the increase in stress at later times results from an increase in modulus of the polymer due to crystallization with no evidence that these are oriented.

40. Kumaraswamy, G.; Verma, R. K.; Wang, P.; Kornfield, J. A.; Yeh, F.; Hsiao, B. S. (in preparation).

41. Jones, A. T.; Aizlewood, J. M.; Beckett, D. R. *Makromol. Chem.* **1964,** *75,* 134.

42. Bushman, A. C.; McHugh, A. J. *J. Appl. Polym. Sci.* **1997,** *64,* 2165.

43. Figure 4 in.[24]

44. Rietveld, J.; McHugh, A. J. *J. Polym. Sci. (Polym. Lett.)* **1983,** *21,* 919.

45. McHugh, A. J.; Blunk, R. H. *Macromolecules* **1986,** *19,* 1249.

46. McHugh, A.; Spevacek, J. *J. Polym. Sci. (Polym. Phys.)* **1991,** *29,* 969.

47. Atactic polypropylene (M_n 96300 g/mol; M_w 217000 g/mol; M_z 407000 g/mol) was sheared at a temperature of 150°C for shearing times of $\sim$ 20 s at wall shear stresses around 0.1 MPa. No upturn was seen in the birefringence observed during shear.

48. Keller, A.; Kolnaar, H. W. H. Processing of Polymers. In Vol. 18; Meijer, H. E. H., Ed.; VCH: 1997; Chapter Flow Induced Orientation and Structure Formation.

Chapter 4 A Kinetic Pathway to Enhanced Anisotropic Nucleation: Implications for Nucleation Theory

4.1 Introduction

Investigations of nucleation and the factors that influence it are crucial to develop a better understanding and control of crystallization. Recent studies indicate that the formation of germ nuclei may be mediated by pathways not described by classical nucleation theory. For example, numerical simulations[1,2] were used to show that density fluctuations near the critical point for metastable fluid-fluid separation in solutions of globular protein-like colloids could lead to enhanced crystal nucleation. Such studies provide valuable insights into the fundamentals of crystallization and can help design optimal strategies for crystal growth. Very few experimental studies have probed the earliest events leading to the inception of crystallinity since the investigation of transient phenomena such as nucleation pose formidable challenges. Recently, Sirota and Herhold[3] used synchrotron WAXD to prove that crystallization of short n-alkanes is nucleated via a transient metastable rotator phase while n-odd alkanes crystallize directly into the stable triclinic crystal. They correlated this with the odd-even effect in the crystallization of n-alkanes, thus showing that this previously mysterious crystallization behavior is governed by the formation of the intermediate phase. The implications of intermediate states for crystallization kinetics and morphology have prompted investigations into the role of "non classical" pathways to nucleation in other systems[4] as well.

In semicrystalline polymers, the nature of crystal nucleation and growth are strongly influenced by the covalent connectivity along the polymer chain. Connectivity topologically frustrates crystallization, resulting in a hierarchy of kinetically determined structures.[5,6] The effects of chain connectivity are especially dramatic when flow is imposed, since readily accessible deformation rates perturb the configuration of the slow relaxing macromolecules: the crystallization kinetics are accelerated,[6] nucleation density is increased[7,8] and oriented crystalline morphologies often develop.[6,9,10] As discussed in Section 3.1, theoretical models to explain flow effects on crystallization have not enjoyed much success in predicting either the phase transformation kinetics or the morphology that develops: Models based on thermodynamic arguments[11,12] consistently underpredict the effects of flow and do not provide information about the formation of anisotropic semicrystalline morphologies while the current state-of-the-art models for flow induced crystallization[13,14] rely on geometric Avrami-type nucleation and growth phenomenology, and cannot be used predictively since they use an empirical coupling parameter to fit experimental data with no physical understanding of the factors responsible for enhanced nucleation. Thus, the fundamental nature of the earliest events in crystallization remain mysterious, particularly under the influence of flow. Considering that semicrystalline polymers represent about 65% of the volume of the entire polymer industry and virtually all are subjected to intense deformation as they are processed into final form, understanding flow-induced changes in nucleation density and morphological anisotropy which profoundly alter material properties[6,15] is of enormous technological importance.

While heterogeneous nucleation (through chemical[16] or epitaxial[17–19] interactions with heterogeneities in the melt) typically dominates in quiescent crystallization of polymers,[6] the dramatic increase in the number of nuclei per unit volume induced by flow appears to originate from the melt itself. Homogeneous nucleation has traditionally been viewed in terms of classical nucleation theory, which assumes that nuclei of the crystal phase develop directly from the melt as a result of density or conformational fluctuations. The model assumes that the nuclei are in contact with the crystallizing melt and estimates the critical size for the nucleus to grow based on the free energy penalty associated with this interface. Crystal growth then proceeds from these nuclei and the molecules order into superstructures at larger length scales.[5] Turnbull and Fisher[20] applied the theory of absolute reaction rates to the nucleation theories developed by Gibbs[21] and Becker and Doring[22] to determine the rate of nucleation, r^* as:

$$r^* = \frac{k_B\mathrm{T}}{h} exp[-\frac{(\Delta G^* + \Delta G_\eta)}{k_B\mathrm{T}}] \tag{4.1}$$

where k_BT is Boltzmann's constant times the absolute temperature, h is Planck's constant, ΔG^* is the bulk free energy difference associated with the formation of a crystal phase in the melt and ΔG_η is the energy of activation associated with diffusion across the phase boundary. For a polymer, $\Delta G_\eta / k_B\mathrm{T}$ can be assumed to follow Williams-Landel-Ferry (WLF)[23] behavior and, thus, diverges near the glass transition temperature, T_g, as chain mobility goes to zero.

$$\Delta G_\eta = \frac{c_1(\mathrm{T} - \mathrm{T}_0)}{c_2 + (\mathrm{T} - \mathrm{T}_0)} \tag{4.2}$$

where $\mathrm{T}_0 \approx (\mathrm{T}_g$ - 50) and c_1 and c_2 are material dependent constants. The free energy difference associated with formation of the crystal phase from the melt is negative for temperatures below the equilibrium melting point, T_{Mo}, of the polymer and decreases very rapidly below T_{Mo}. Thus, the nucleation rate, r^*, goes to zero near T_g and near T_{Mo} and has a maximum in between. Thus, according to classical nucleation theory, the nucleation rate for semicrystalline polymers far above T_g decreases exponentially as the temperature approaches the melting point.

Recent work has prompted a reexamination of classical nucleation theory for semicrystalline polymers to account for the possible role of metastable states.[4] For example, to account for the time dependence of scattering data from crystallizing polymers,[25–30] it has been suggested that the polymer melt might undergo a spinodal liquid-liquid phase transition when cooled from above the equilibrium melting point, and primary nucleation might occur from the metastable "dense" liquid phase.[31] An alternate "non-classical" theory invokes a size-dependent surface tension for the nucleus-melt interface[32–34] to postulate the formation of stable proto-crystalline aggregates (athermal nuclei) which develop into lamellae below an "activation" temperature. In addition to these thermodynamic approaches, others[35-37] have speculated that flow might lead to kinetics routes to crystallization. As the crystallization behavior (e.g., lamellar thickness, crystallization half time, final level of crystallinity) might be determined by the intermediate states that lead to nucleation, it is important to characterize the pathway to crystallization by *in-situ* real time studies. Here, we present evidence that flow induced nucleation is indeed mediated by a kinetic pathway.

4.2 Experimental

Shear enhanced crystallization of PP-300/6 was examined using the "short-term" shearing protocol described in previous Chapters. A combination of *in-situ*, real time rheo-birefringence and rheo-synchrotron WAXD was employed to investigate the events during a brief interval of flow. The experimental set-up for the *in-situ* rheo-birefringence studies is as described in Section 2.3.5. The flow cartridge was modified for the *in-situ* WAXD studies. In the modified cartridge, synchrotron radiation is incident on the polymer through ports in the sample cell sealed with 300μm thick beryllium windows (Figure 4.1). A conical aperture on one side of the sample cell allows us to observe diffraction to angles (2θ) of up to $\approx 35°$. For ease of alignment, the entire shear device was placed on a translation stage allowing us to move it perpendicular to the incident X-ray beam. Data was acquired using a liquid nitrogen cooled CCD (MAR-CCD) with a resolution of 1024 x 1024 pixels (pixel size = 128.8 μm). The detector was placed about 16 cm from the sample cell. The scattering angles were calibrated using an α-alumina NIST standard. Experiments were carried out at beamline X27C of the National Synchrotron Light Source, Brookhaven National Laboratory, using an X-ray wavelength of 1.307Å.

The iPP melt was sheared at a fixed wall shear stress ($\sigma_w = 0.06$ MPa) that is large enough to induce the transition to oriented growth,[38] and the transient orientation created during and after flow was observed as a function of temperature using birefringence and WAXD.

4.3 Results

In Chapter 3, we determined that the formation of the ordered "shear-induced structure" during flow at T_{cryst} = 141°C is manifested as an unusual monotonic increase in the birefringence after the nonlinear rheological overshoot upon startup of shearing and is correlated with the development of an oriented skin-core morphology. To understand the dynamics of creation of these crystallization precursors, we examine the effect of temperature. *In-situ* synchrotron WAXD is used to determine their nature.

Crystallization experiments at 150°C, at σ_w =0.06 MPa, showed the same trend as experiments at the lower crystallization temperature (141°C) and the same wall shear stress (Chapter 3): the crystallization kinetics were accelerated as the polymer was sheared, and the formation of oriented skin-core crystalline structures in the crystallized samples was found to correlate with formation of the "shear induced structure" during shear (data not presented). As expected, the quiescent crystallization kinetics at 150°C was slower than at T_{cryst} = 141°C by about an order of magnitude. The "shear induced structure," however, appeared at about the same shearing time as observed at T_{cryst} = 141°C (about $t_s \sim 5$ s, Figure 3.6).

In-situ WAXD was used to determine the nature of the oriented structures that are manifested in the upturn in the birefringence. At 141 and 163°C, crystalline peaks corresponding to the α-monoclinic phase of iPP[40] appear during shear in a matter of a few seconds (Figure 4.5 a,b)—orders of magnitude faster than the quiescent crytallization time (Figure 4.3). Two-dimensional WAXD patterns obtained as the polymer is sheared show that the crystallites induced by flow are highly oriented (Figure 4.6). The scattering patterns corresponded to a uniaxial distribution of the crystallites about the c-axis, which is predominantly parallel to the flow direction (See Section 5.4). As expected, at 141°C, these "parent" crystallites are accompanied by crystallographically branched "daughter" cross-hatched crystals,[41,42] unique to the α-form of iPP (Figure 4.6 a). Interestingly, these "daughters" form concurrently with the "parents," with little observable time lag (Chapter 5). These WAXD results suggest that the upturn in the birefringence during shear comes from oriented α-

iPP crystallites, making the earlier upturn at 150°C compared to 141°C even more surprising.

To examine the unanticipated temperature dependence of the formation of the "shear induced structure," we investigated the response of PP-300/6 to short-term shearing at various temperatures at a fixed wall shear stress (Figure 4.2). Experiments at fixed σ_w give rise to approximately the same average orientation of the polymer chain segments in the melt. At *higher* temperatures, viz. at lower undercoolings, the upturn in the birefringence develops at *shorter* shearing times (Figure 4.2 a). The "shear induced structure" is observed even at temperatures as high as 175°C (above the nominal melting temperature of about 170°C). Interestingly, the temperature dependence of the time for the birefringent upturn, t_u, is strikingly similar to that of the melt dynamics described by the rheological temperature dependent shift factor, a_T[23,24] (solid line, Figure 4.3). Therefore, the time for the upturn in the birefringence can be collapsed by rescaling the time axis for each experiment by a temperature dependent shift factor, a'_T, similar to the rheological shift factor ($a'_T \sim t_u$; Figure 4.2 b, Figure 4.3 inset).

Upon cessation of flow, the "shear induced structure" decays to a non-zero value at temperatures below 170°C (Figure 4.4), while it decays completely for temperatures of 170°C and above. These "melt" shearing experiments and the formation of the "shear induced structure" were found to be far less sensitive to temperature fluctuations during the experiment than might be expected for crystallization at low subcoolings (see strong temperature dependence of t_Q in Figure 4.3). Thus, reproducible results were obtained even with the ±1°C level of temperature stability and uniformity maintained for these experiments. While the overall shape of the birefringence traces is robust, details such as the inflection in the experimental trace at 160°C (Figure 4.4) were sensitive to subtle changes in experimental conditions (perhaps, temperature variations in the shear cell).

Having identified the oriented structures manifested in the upturn as crystalline, it is interesting to compare the time for the appearance of the birefringence upturn, t_u (filled symbols, Figure 4.3), to the time required for crystallites to appear in a quiescent sample (open symbols, Figure 4.3). The quiescent crystallization time is a strong function of temperature, slowing by two orders of magnitude with increasing temperature from 130 to 150°C; in contrast, the time for oriented crystallites to appear under the influence of flow, manifested in t_u, is a weak function of temperature—and occurs at *earlier* times as temperature *increases*. Thus, the inception of flow-induced crystallization appears to be regulated by the kinetics of development of a particular anisotropic orientation state of the melt; once this orientation state is reached, oriented crystallites appear to form immediately, regardless of the degree of subcooling.

Above 163°C, it is not possible to use WAXD to confirm that the birefringence upturn is associated with generation of oriented crystallites, since crystalline peaks cannot be resolved from the noise during shear (Figure 4.5 c,d). Nevertheless, the inference that highly oriented crystallites are generated during shear at 168°C is supported by the development of highly oriented crystallinity after cessation of flow (Figure 4.5 c and two-dimensional WAXD not shown) on timescales orders of magnitude faster than quiescent crystallization (extrapolated to be $t_Q \sim O(10^6 \text{ s})$ based on quiescent data shown in Figure 4.3). The peculiar birefringence upturn is observed at temperatures up to 175°C — above the nominal melting point for iPP ($T_{nom} \approx$ 170°C) (Figure 4.4). However, at 173°C, crystalline WAXD peaks are never observed (Figure 4.6 d). This observation accords well with *in-situ* birefringence development after cessation of flow[38] (Figure 4.4): at temperatures above 170°C, the upturn in the birefringence that is generated during shear relaxes to zero upon cessation of flow rather than leading to the subsequent growth of oriented crystals. At 170°C and above, the birefringent upturn that develops during flow simply relaxes away after cessation of flow and the polymer does not crystallize, as expected for temperatures at and above the nominal melting point. It was not possible to explore temperatures above 175°C due to the low viscosity of the sample at higher temperatures (the upper limit on the shearing time is dictated by the 100 strain unit maximum as explained in Chapter 2; above 175°C, even the longest admissible t_s became too short to achieve properly with our pneumatic system). Thus, we could not establish the upper limit in temperature for the creation of oriented precursors.

4.4 Discussion

4.4.1 Dynamics that Control the Formation of Oriented Structures

The effect of temperature on the development of the peculiar upturn in the birefringence during shear is quite surprising. With increasing temperature, the quiescent crystallization time increases strongly, due to the reduced subcooling. If the same physics played a significant role in determining the kinetics of formation of the highly oriented structures that form during flow, then they would form at later times with increasing temperature. Instead the opposite behavior is observed (Figure 4.2 a): with increasing temperature, the upturn in the birefringence occurs at earlier times. This trend continues to hold even to temperatures above the melting point observed by hot stage microscopy! Interestingly, the temperature dependence is very close to that of the rheological time-temperature shift factor (solid curve, Figure 4.3). This indicates that, while the "shear induced structure" shows crystalline WAXD reflections, its formation does not show the temperature dependence characteristic of a nucleated process. Rather, it appears to be strongly influenced by the dynamics of polymer chains in the melt. This temperature dependence is consistent with the rate-limiting step being the creation of a given orientational state of the melt. The stress-level largely sets the magnitude of the anisotropy that will be reached; the time required to reach a given point in the transient orientation distribution after the flow start-up decreases with increasing temperature.

The fate of the oriented structures induced during shear is very sensitive to temperature in the vicinity of the melting point observed by DSC or hot stage microscopy. For temperatures of 160°C or lower, the birefringence does not fully relax after cessation of flow and the birefringence that remains starts to grow as soon as relaxation is complete (Figure 4.4). At temperatures of 170°C or 175°C, the birefringence relaxes completely to zero after cessation of flow. Experiments by Mc Hugh and coworkers[44,43] on the crystallization of an HDPE droplet in planar extensional flow indicate that the development of strong orientation in the system during flow relaxes after the cessation of flow for temperatures above the nominal melting point of the polymer (while for lower temperatures, this leads to the development of oriented crystallites). In addition, Sakellarides and Mc Hugh[45] observed fibrillar crystals of HDPE at temperatures above the nominal melting point in the presence of localized, strong extensional gradients and found they were stable for a few minutes after cessation of flow after which they melted gradually.

4.4.2 Implications of Shear-Induced Structures Formed above the Nominal Melting Point

A recent theory proposed by Janeschitz-Kriegl and coworkers[32,33] may provide insight into the "shear induced structure" generated at high temperatures. They argue that the free energy penalty from classical nucleation theory associated with the formation of an interphase is a function of the size of nucleus, and goes to zero as the size decreases (leading to "athermal" nuclei). In the context of polymer crystallization, this surface free energy term physically represents the energy associated with fold surface at the amorphous-crystal interphase. On the basis of thermodynamic arguments, they estimate the upper bound for the formation of a stable athermal nucleus for iPP, $T_u \approx 170°C$ to 180°C. Athermal nuclei formed below this temperature are always stable, while they are metastable between T_u and the equilibrium melting temperature of the polymer. Our observations seem to accord well with this theory. The picture that emerges then is as follows: Upon shearing a polydisperse polymer melt below T_u, the high molecular weight chains in the melt are strongly distorted from their isotropic state. They can then form the "thread like precursors" that grow off heterogeneities in the melt or the athermal nuclei. The fraction of high molecular weight chains might determine the concentration of the "thread like precursors", which could account for the observed saturation behavior in $t_{1/2}$ as a function of t_s (Figure 3.5). At crystallization temperatures of 140°C or 150°C, crystalline structures might grow off the "thread like precursors" in a very short time compared to the quiescent crystallization times ($> 10^4$ s) giving rise to the observed crystalline diffraction spots that appear in a matter of a few seconds (Figure 4.5). This explanation is also consistent with the temperature dependence of the time of formation of the "shear induced structures." Further, it can be hypothesized that shearing the polymer melt increases T_u, and thus, at temperatures around to 170°C, the athermal nuclei (and consequently the "shear induced structures") may disappear upon cessation of shear.

The strong dependence of the "shear induced structures" on rheological parameters indicates a direction for future studies to understand the molecular underpinnings of the "thread like precursors" in the shear induced crystallization model of Janeschitz-Kriegl (described in Section 3.1). Our results suggest that the "missing" time scale and the arbitrary critical shear strain rate in their model might be related to the rheological time scales of relaxation of the melt. Our data also suggests that the coupling parameters in the flow-induced crystalliztaion model of Mc Hugh et al.[14] (described in Section 3.1) might depend on the chain length polydispersity of the system. Thus, further studies with binary blends of low polydispersity "long" and "short" chains might provide clues that could lead to a better understanding of the model parameters.

4.4.3 The Role of Molecular Mass Polydispersity in the Creation of Precursors to Oriented Crystallization

The precursors created during flow template the structures that grow after cessation of flow at temperatures below the nominal melting point. A detailed investigation (see Chapter 5) of the development of the oriented morphology at 141°C reveals that the crystals that grow after cessation of flow retain the same fiber-like orientation distribution as those induced during flow. *Ex-situ* optical[38] and electron[46] micrographs of corresponding specimens quenched after shear crystallization reveal that the highly oriented crystallites develop in a row nucleated or "shish-kebab" morphology: "parent" lamellae (kebabs) grow radially from central line nuclei (shish) until they impinge. Thus, the generation of the threadlike precursors governs the morphology and kinetics of development of highly oriented semicrystalline structure.

Ex-situ microscopy (see Chapters 3, 5) shows that the shish-kebabs form only in "skin" layers near each wall where the stress and deformation rates are highest during flow. The spatial transition from skin to core regions in these micrographs is sharp, indicating that the induction of the shish kebab morphology is a highly non linear function of the stress. Highly oriented shish-kebab morphologies are observed only for polymers with a broad distribution of chain lengths. For shear crystallization experiments with relatively narrow polydispersity iPPs ($M_w/M_n \sim$ 2-3) of M_w above and below that of the polymer investigated here, strongly oriented semicrystalline morphologies are not observed. However, blending a small amount of high molecular weight chains ($M_w \sim 825$ kg/mol; PDI ≈ 2.8; tacticity index based on a ratio of the IR peaks at 998 and 973 $\text{cm}^{-1} = 0.906$) into lower molecular weight material ($M_w \sim 186$ kg/mol, PDI ≈ 2.16; IR tacticity index $= 0.913$) restores the tendency to form oriented morphologies (Figure 4.7). These results accord well with qualitative observations in the literature,[47] showing that the slowest relaxing chains in a broad distribution material are crucial for the formation of oriented morphologies.

The role of dilute long chains suggests a molecular mechanism for flow mediated anisotropic nucleation. While a fixed σ_w generates approximately the same average level of orientation of chain segments, the slow relaxing, high molecular weight species in a flowing polydisperse sample are more strongly perturbed from their equilibrium configuration than the lower molecular weight species. We speculate that the oriented local configurations generated in the vicinity of the highly distorted slowly relaxing species preferentially form the precursors for oriented nucleation. This molecular insight into flow-induced nucleation can be used to guide materials design enabled by recent advances in catalyst chemistry[48–50] that provide exquisite control over synthesis of semicrystalline polymers. Systematic control over polymer chain architecture translates to control over the macromolecular relaxation time distribution, and consequently to control over the semicrystalline morphology of processed polymers.

4.5 Conclusions

Observations of the earliest events that lead to anisotropic nucleation in semicrystalline polymers subjected to flow reveal a kinetic, "non-classical" route to anisotropic polymer crystallization. The formation of order in a subcooled isotactic polypropylene melt subjected to a brief interval of shear was examined using a combination of *in-situ* structural probes (rheo-birefringence and rheo-synchrotron-WAXD). Oriented crystallization precursors develop during flow, even at temperatures exceeding the nominal melting temperature, T_{nom} of the polymer. These precursors form at timescales that are governed by the dynamics of development of an oriented chain configuration in the melt. Thus, the transition to highly oriented crystallization, over a wide temperature range, is predominantly governed by the development of this anisotropic orientation distribution of polymer chain segments rather than the subcooling. The line-like precursors template the formation of oriented crystallites which grow after flow cessation at temperatures below the nominal melting point, T_{nom}. At temperatures above T_{nom}, no crystalline growth is observed, indicating that the precursors that develop during the short-term shearing relax after flow cessation. Preliminary results with bidisperse blends of high and low molecular weight isotactic polypropylenes implicate the slowest relaxing species (the high molecular weight chains) play a critical role in the formation of the oriented precursors, proving that chains whose conformation becomes much more distorted than the average are needed to form these precursors.

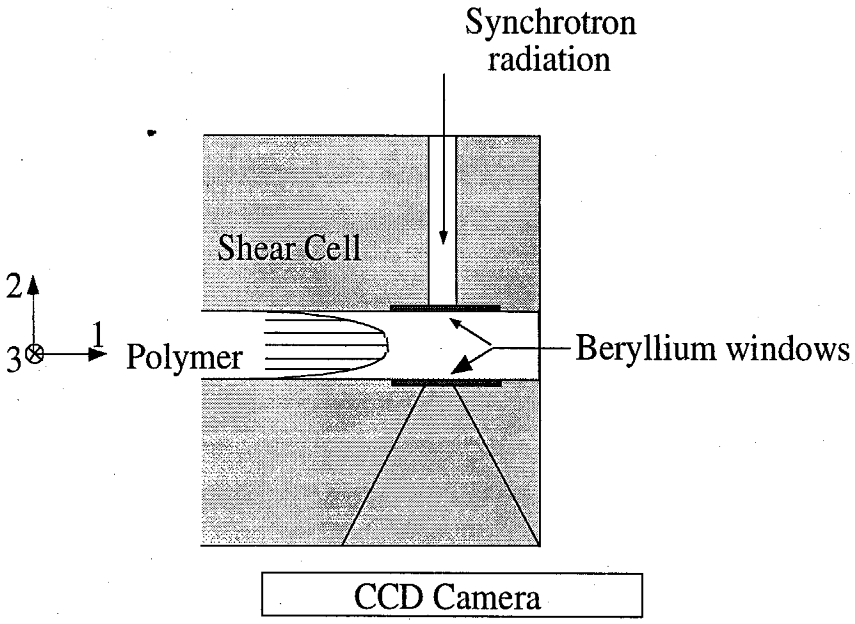

Figure 4.1: Schematic of the shear cell used for *in-situ* synchrotron X-ray WAXD. The beryllium windows are flush with the flow channel. The flow (1), velocity gradient (2) and vorticity (3) axes are as indicated in the figure. Light propagates down the gradient direction (2) in all *in-situ* optical experiments.

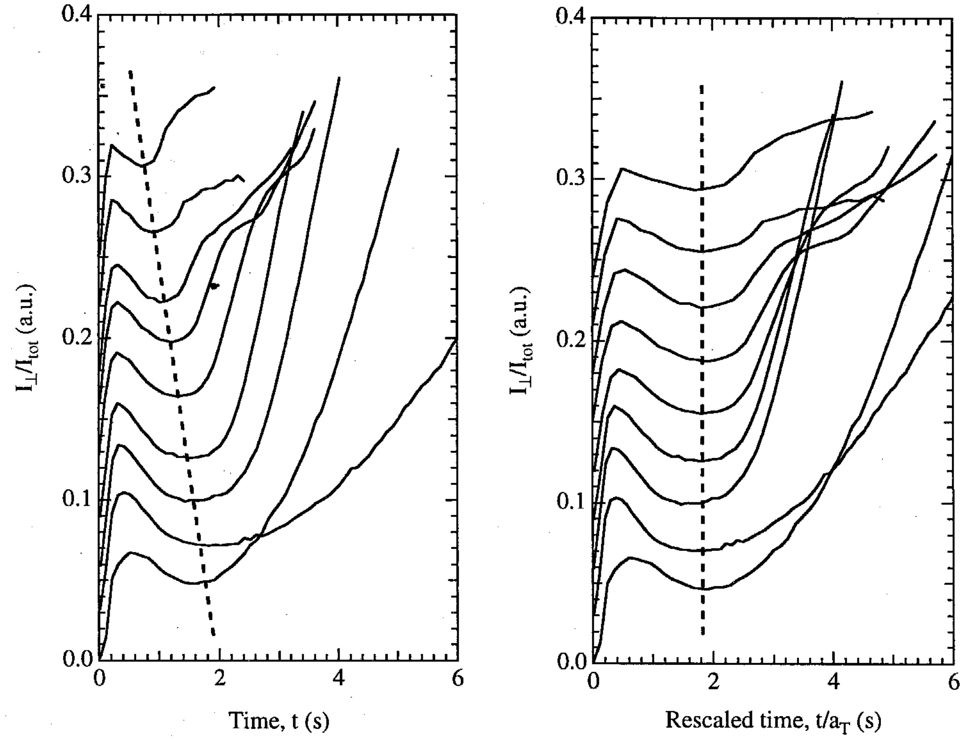

Figure 4.2: Temperature dependence of the shear induced structure manifested in the upturn in the birefringence during shear. In both plots the curves represent experiments at 135, 140, 145, 150, 155, 160, 165, 170 and 175°C starting from the bottom. The higher viscosity at lower temperatures meant that the polymer was sheared for a longer time before a shear strain of 100 was reached. Birefringence traces are shown as a function of (a) time and (b) rescaled time using a temperature dependent shift factor, a'_T, to superimpose the upturn in the birefringence. The magnitude of the initial transient overshoot in $I_\perp/I_{tot}$ overlaps to within 25% with the peak height decreasing with increasing temperature.

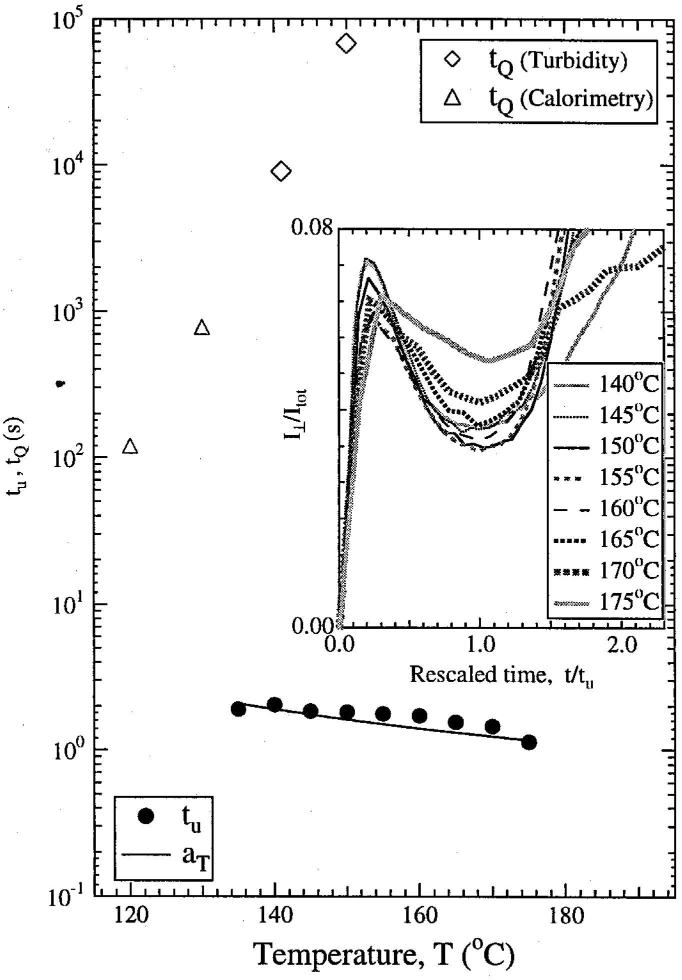

Figure 4.3: Temperature dependence of the timescale for quiescent crystallization, t_Q, and of the time to inception of the unusual upturn in birefringence during shear, t_u. The triangles are peak times for crystallization measured using differential scanning calorimetry while the diamonds are the time to reach turbidity of 0.5 from quiescent experiments in our flow device. t_u was obtained as the lowest point of a parabola fitted to the birefringence trace near the upturn. The solid line is the WLF rheological shift factor with respect to a reference temperature of 190°C. The inset shows birefringence traces during shear plotted against rescaled time as a function of temperature.

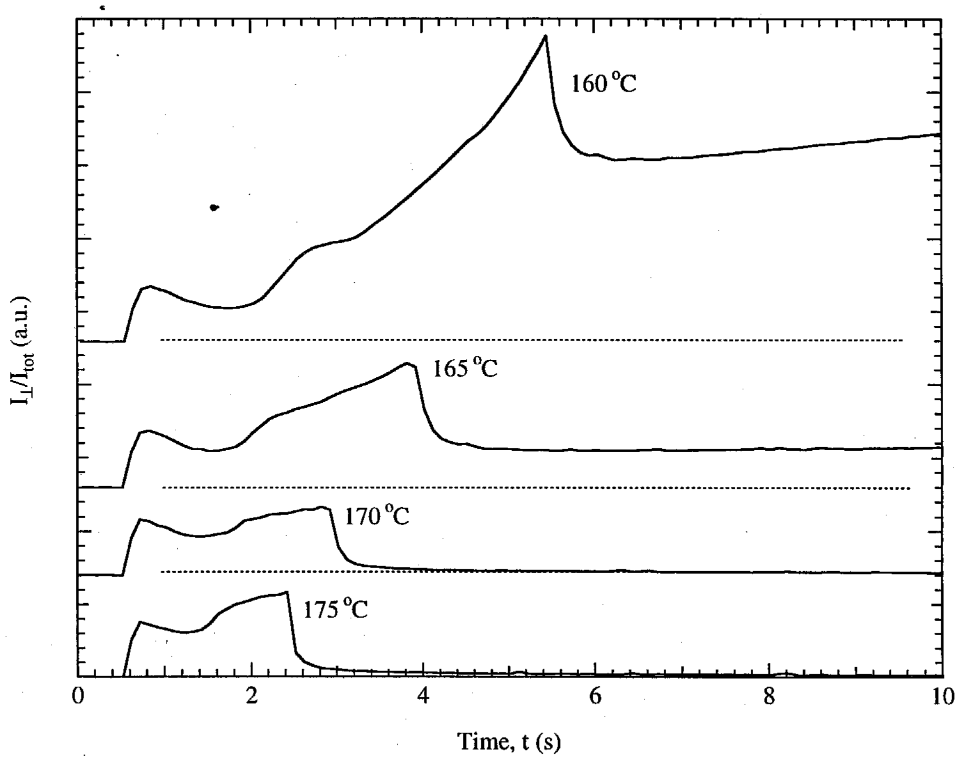

Figure 4.4: The intensity of light through crossed polarizers during shearing at σ_w =0.06 MPa to approximately 100 strain units at the wall and after cessation of flow. Note that the birefringence observed during shear decays completely after shear cessation only at temperatures higher than 170°C.

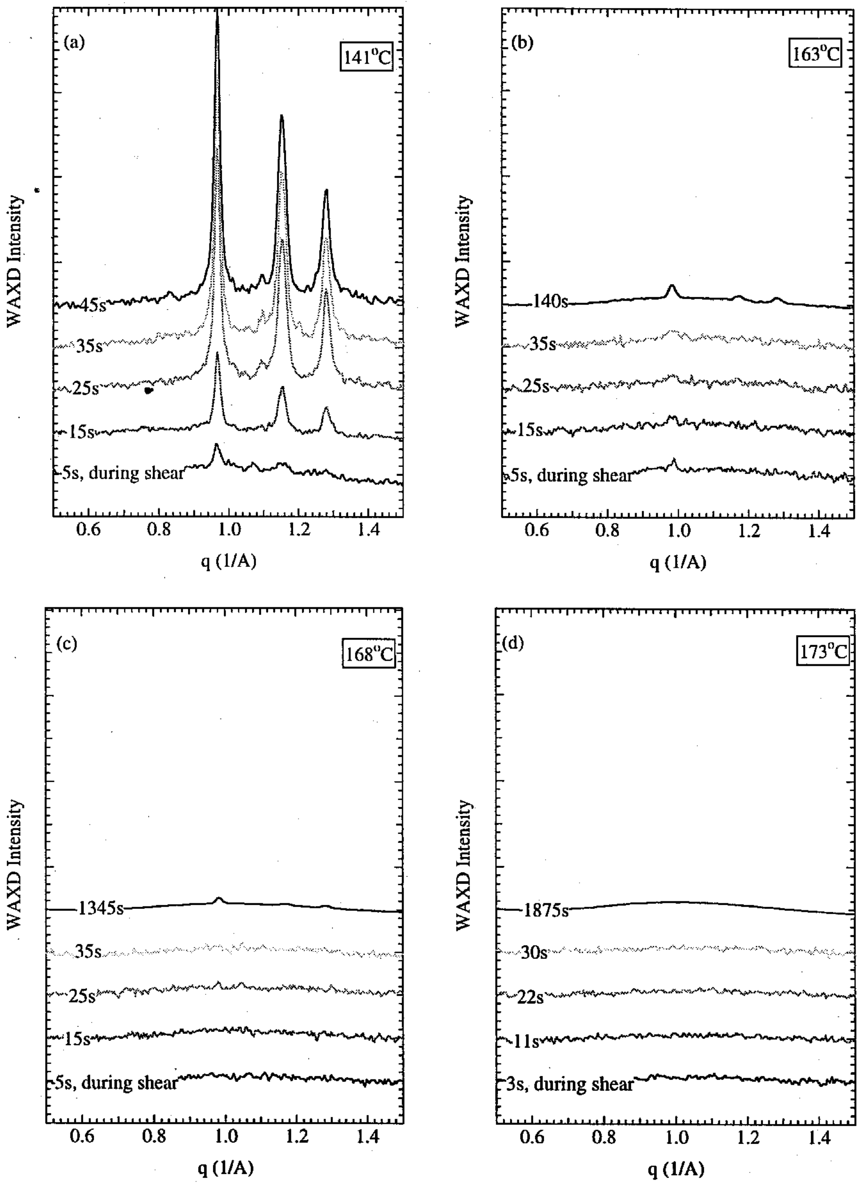

Figure 4.5: Evolution of WAXD intensity during and after cessation of shear at (a) 141°C, (b) 163°C, (c) 168°C and (d) 173°C. Traces have been normalized for acquisition time at each temperature.

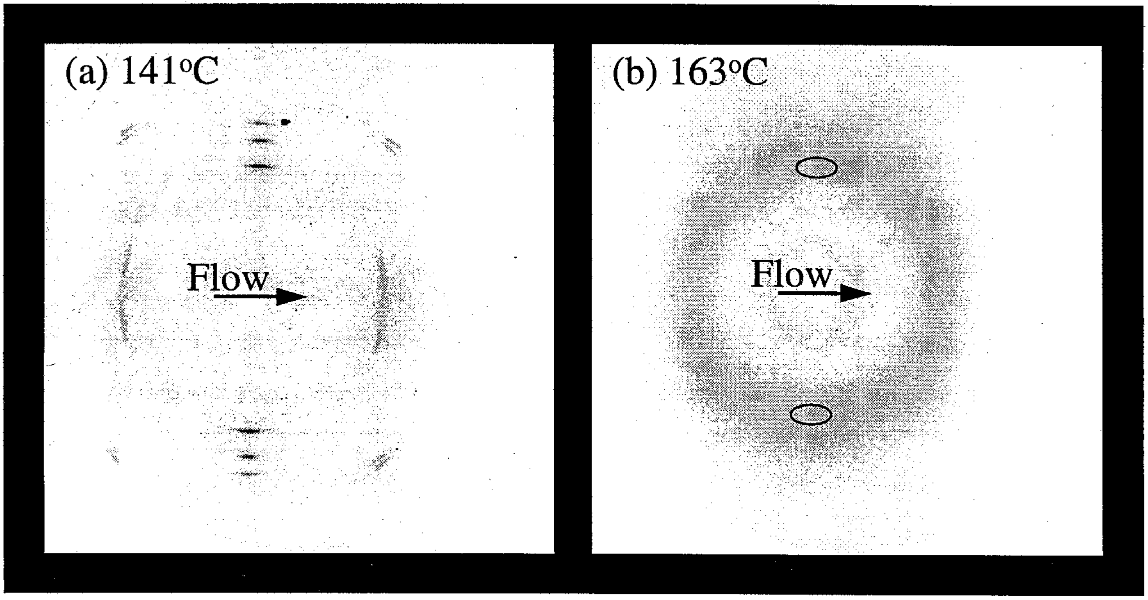

Figure 4.6: Two-dimensional oriented WAXD patterns obtained during shear at (a) 141°C and (b) 163°C. Peaks from "parent" and "daughter" are evident in (a). Faint 110 peaks from the "parent" crystals can be seen in the indicated areas in (b).

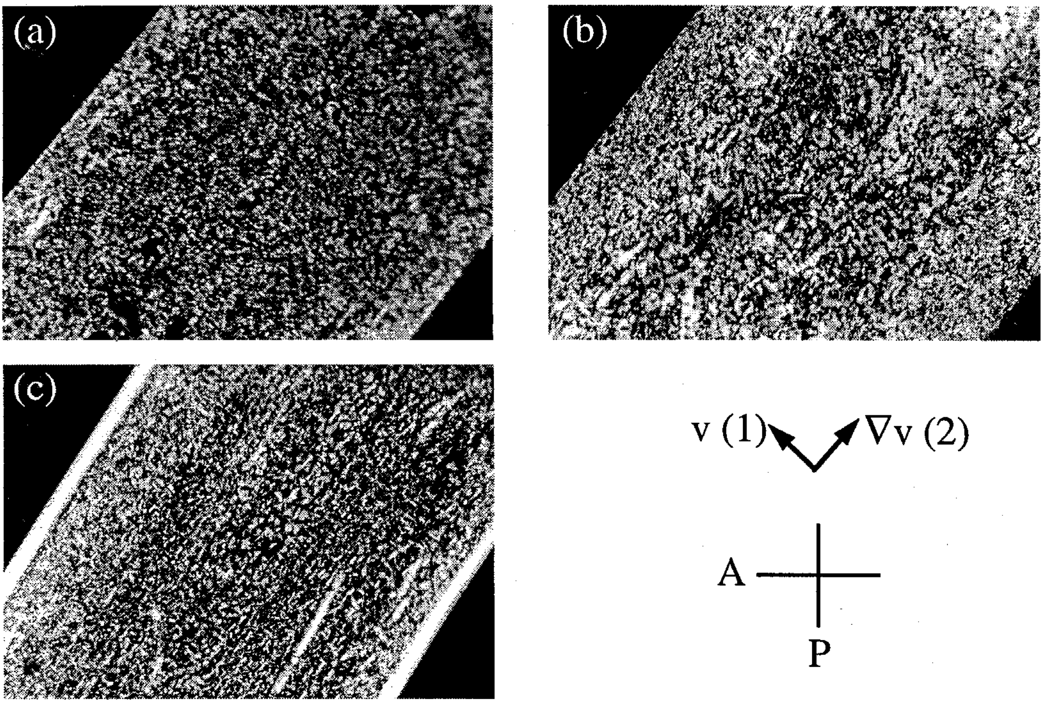

Figure 4.7: *Ex-situ* optical micrographs of shear crystallized isotactic polypropylene viewed in the flow-velocity gradient plane through crossed polarizers (the direction of the analyzer and the polarizer are as indicated). Strongly anisotropic skin-core morphology is not observed when the narrow polydispersity, model materials are subjected to extreme shearing: (a) shows the results when the low molecular weight material ($M_w \sim 186$ kg/mol) is sheared at $\sigma_w \approx 0.1$ MPa for $t_s = 1.2$ s (total strain at the wall, $\gamma \approx 100$ and (b) shows the results for the high molecular weight material ($M_w \approx 825$ kg/mol) sheared at $\sigma_w \approx 0.1$ MPa for $t_s = 300$ s. However, in (c), we observe formation of an oriented skin for short term shearing ($\sigma_w \approx 0.1$ MPa; $t_s = 1.25$ s; $\gamma \approx 100$) of a bidisperse blend of the model resins containing just 2% of the high molecular weight material.

Bibliography

1. tenWolde, P. R.; Frenkel, D. *Science* **1997,** *277,* 1975.
2. Talanquer, V.; Oxtoby, D. W. *J. Chem. Phys.* **1998,** *109,* 223.
3. Sirota, E. B.; Herhold, A. B. *Science* **1999,** *283,* 529.
4. Keller, A.; Cheng, S. *Polymer* **1998,** *39,* 4461.
5. Bassett, D. *Principles of Polymer Morphology,* Cambridge University Press: 1981.
6. van Krevelen, D. *Chimia* **1978,** *32,* 279.
7. Haas, T.; Maxwell, B. *Polym. Eng. Sci.* **1969,** *9,* 225.
8. Wolkowicz, M. *J. Polym. Sci. (Polym. Symp.)* **1978,** *63,* 365.
9. Binsbergen, F. L. *Nature* **1966,** *211,* 516.
10. Keller, A.; Machin, M. J. *J. Macromol. Sci. (B)* **1967,** *1,* 41.
11. Flory, P. J. *J. Chem. Phys.* **1947,** *15,* 397.
12. Krigbaum, W.; Roe, R. *J. Polym. Sci. (A)* **1964,** *2,* 4391.
13. Bushman, A.; McHugh, A. *J. Polym. Sci. (Polym. Phys.)* **1996,** *34,* 2393.
14. Doufas, A. K.; Dairanieh, I. S.; McHugh, A. J. *J. Rheol.* **1999,** *43,* 85.
15. Meijer, H., Ed.; *Processing of Polymers,* volume 18 VCH (NY): 1997.
16. Legras, R.; Mercier, J.; Nield, E. *Nature* **1983,** *304,* 432.
17. Wittman, J. C.; Lotz, B. *J. Polym. Sci. (Polym. Phys.)* **1981,** *19,* 1837.
18. Wittman, J. C.; Lotz, B. *J. Polym. Sci. (Polym. Phys.)* **1981,** *19,* 1853.

19. Wittman, J. C.; Hodge, A. M.; Lotz, B. *J. Polym. Sci. (Polym. Phys.)* **1983,** *21,* 2495.

20. Turnbull, D.; Fisher, J. C. *J. Chem. Phys.* **1949,** *17,* 71.

21. Gibbs, J. W. *Trans. Conn. Acad.* **1878,** *III,* 343.

22. Becker, R.; Doring, W. *Ann. d. Physik* **1935,** *24,* 719.

23. Ferry, J. D. *Viscoelastic Properties of Polymers,* John Wiley, NY: 3 ed.; 1980.

24. Eckstein, A.; Suhm, J.; Friedrich, C.; Maier, R.-D.; Sassmannshausen, J.; Bochmann, M.; Mulhaupt, R. *Macromolecules* **1998,** *31,* 1335.

25. Imai, M.; Mori, K.; Mizukami, T.; Kaji, K.; Kanaya, T. *Polymer* **1992,** *33,* 4451.

26. Imai, M.; Mori, K.; Mizukami, T.; Kaji, K.; Kanaya, T. *Polymer* **1992,** *33,* 4457.

27. Imai, M.; Kaji, K.; Kanaya, T. *Macromolecules* **1994,** *27,* 7103.

28. Cakmak, M.; Teitge, A.; Zachmann, H.; White, J. *J. Polym. Sci. (Polym. Phys.)* **1993,** *31,* 371.

29. Ezquerra, T. A.; Lopez-Cabarcos, E.; Hsiao, B.; Balta-Calleja, F. *Phys. Rev. E* **1996,** *54,* 989.

30. Ryan, A.; Patrick, J.; Fairclough, A.; Terrill, N.; Olmstead, P.; Poon, W. *Faraday Discuss.* **1999,** *112,* 13.

31. Olmstead, P.; Poon, W.; McLeish, T.; Terrill, N.; Ryan, A. *Phys. Rev. Lett.* **1998,** *81,* 373.

32. Janeschitz-Kriegl, H. *Colloid Polym. Sci.* **1997,** *275,* 1121.

33. Janeschitz-Kriegl, H.; Ratajski, E.; Wippel, H. *Colloid Polym. Sci.* **1999,** *277,* 217.

34. Tolman, R. C. *J. Chem. Phys.* **1949,** *17,* 333.

35. Lagasse, R.; Maxwell, B. *Polym. Eng. Sci.* **1976,** *16,* 189.

36. Sherwood, C.; Price, F.; Stein, R. *J. Polym. Sci. (Polym. Symp.)* **1978,** *63,* 77.

37. Wunderlich, B. *Macromolecular Physics,* volume 2. Crystal Nucleation, Growth, Annealing Academic Press (NY): 1976.

38. Kumaraswamy, G.; Issaian, A. M.; Kornfield, J. A. *Macromolecules* **1999,** *32,* 7537.

39. Menezes, E.; Graessley, W. *J. Polym. Sci. (Polym. Phys.)* **1982,** *20,* 1817.

40. Jones, A. T.; Aizlewood, J. M.; Beckett, D. R. *Makromol. Chem.* **1964,** *75,* 134.

41. Lotz, B.; Wittmann, J. C. *J. Polym. Sci. (Polym. Phys.)* **1986,** *24,* 1541.

42. Lovinger, A. J. *J. Polym. Sci. (Polym. Phys.)* **1983,** *21,* 97.

43. Bushman, A. C.; McHugh, A. J. *J. Appl. Polym. Sci.* **1997,** *64,* 2165.

44. McHugh, A.; Guy, R.; Tree, D. *Colloid Polym. Sci.* **1993,** *271,* 629.

45. Sakellarides, S. L.; McHugh, A. J. *Rheol. Acta.* **1987,** *26,* 64.

46. Kumaraswamy, G.; Verma, R. K.; Issaian, A. M.; Wang, P.; Kornfield, J. A.; Yeh, F.; Hsiao, B. S.; Olley, R. H. submitted to *Polymer.*

47. Bashir, Z.; Odell, J. A.; Keller, A. *J. Mater. Sci.* **1984,** *19,* 3713.

48. Horton, A. D. *TRIP* **1994,** *2,* 158.

49. Hamielec, A.; Soares, J. *Prog. Polym. Sci.* **1996,** *21,* 651.

50. Guan, Z.; Cotts, P. M.; McCord, E. F.; McLain, S. J. *Science* **1999,** *283,* 2059.

Chapter 5 Analysis of the Formation of the Oriented "Skin"

5.1 Introduction

Experiments that monitor transient morphological development en route to the final microstructure in a polymeric product provide valuable clues regarding the influence of flow-induced nuclei on the kinetic and geometrical aspects of semicrystalline structure formation. There is enormous commercial value in understanding the development of semicrystalline morphology during and after flow: such understanding can potentially enable the design of processing strategies guided by insight into the interplay between macromolecular flow dynamics and crystallization. For example, while the role of flow in generating the row nucleated crystals had been recognized,[1,2] it was physical insight into the nature of transient structure development that led Keller and coworkers[3] to develop a route to high modulus polyethylene fibers with superior thermal and mechanical properties. By decreasing the subcooling as the polymer crystallized after extrusion, they were able to generate an interlocked "shish kebab" morphology of tapering interdigitated lamellae leading to exceptional performance. A detailed understanding of the fundamentals of structure development during processing remains elusive despite a vast literature[4–10] that examines the effect of changing resin composition (polymer characteristics and/or additives) or processing variables on specific material properties. Most experiments that examine row nucleated structures mimic the high strain and strain rates typical of polymer processing operations, but the complicated thermal and flow history imposed make it difficult to infer the molecular variables that control the semicrystalline morphology that develops.

In contrast to the processing-like protocols, the recent "short term" shearing experiments devised by Liedauer et al.[11] investigate flow effects on crystallization of a semicrystalline polymer under model experimental conditions by subjecting a fully relaxed polymer melt to a short burst of shear isothermally. Studies of the anisotropic morphologies developed in the skin region under these model experimental conditions revealed row nucleated structures similar to those formed under "strong" extensional flows[11,12] or during injection molding.[9] Our *in-situ* WAXD and rheo-birefringence studies of the initial stages of structure development using a similar experimental protocol indicate that the melt anisotropy generated by flow provides a pathway to enhanced nucleation of these oriented crystals (Chapter 4). Here we examine the kinetics and geometry of development of row nucleated crystals during and subsequent to the formation of the flow-induced nuclei. To develop insight into the factors that influence morphological development, it is important to characterize the semicrystalline morphology as it develops. Our rheo-turbidity results (Chapter 3) indicate that the growth of crystals from the flow-induced nuclei saturates within a small fraction of the quiescent crystallization time for shearing times greater than a critical shearing time, t_s^*. However, since turbidity is sensitive to other factors (such as the shape and size of the scatterers) in addition to the degree of crystallinity, rheo-optical results can only be interpreted qualitatively. To better understand the nature of crystallization (kinetics, crystallinity index and crystallite anisotropy), two-dimensional wide angle X-ray diffraction (WAXD) is required. Further, *ex-situ* electron microscopy of samples extracted from the shear device at the end of the experiment provide detailed morphological information that is required to verify the model suggested by the X-ray studies. A combination of *in-situ* turbidity, birefringence and WAXD with *ex-situ* optical and electron microscopy provides us information about structural development at various length scales of interest.

In Chapter 3, *in-situ* birefringence and *ex-situ* polarized optical microscopy investigations showed that certain "extreme" shearing conditions led to the development of a highly anisotropic skin-core morphology. Here, we examine the transient development of the oriented skin under "extreme" shearing ($T_{cryst} = 141°C$ for $\sigma_w = 0.06$ MPa and $t_s = 12$ s in PP-300/6). We present *in-situ* synchrotron WAXD data and *ex-situ* TEM micrographs that show that (i) highly oriented crystallites appear very rapidly (10^{-3} t_Q at 141°C) during the shear pulse, and retain their orientation distribution as crystallization proceeds (ii) cross-hatching is apparent from the beginning, and the ratio of parent to daughter lamellae remains constant with t_{cryst}, (iii) most of the crystallization in the skin region takes place in the first 100 s, the same time taken for the sample to turn turbid, and (iv) the morphology of the skin consists of parent lamellae that radiate out from threads along the flow direction consistent with the model of Liedauer et al.[11]

5.2 Experimental

Guided by our previous rheo-birefringence and optical microscopy (Chapter 3) we have selected a specific experimental condition that leads to the development of highly oriented semicrystalline morphology. The experimental protocol for the condition thus selected is as follows: the flow cell was initially held at $T_{relax} = 225°C$ and filled with polymer melt from the reservoir. After holding at this elevated temperature for 5 minutes (to erase the memory of the filling process and to melt any residual crystallites), the cell is cooled to the crystallization temperature, $T_{cryst} = 141°C$, and held isothermal to within ±0.3°C thereafter. Once the sample was at T_{cryst}, the relaxed, subcooled polymer melt was extruded at $\sigma_w = 0.06$ MPa for a shearing time, $t_s = 12$ s.

In-situ synchrotron WAXD was used to follow the development of semicrystalline morphology in PP-300/6 during and after the cessation of shear. The experimental setup for the synchrotron WAXD measurements is as described in Section 4.2.

Ex-situ electron microscopy was used to study the morphology of the sample extracted from the shear device at $t_{cryst} = 1200$ s and quenched into cold water. The TEM images in this thesis were obtained by Ani Issaian (Caltech) in collaboration with Prof. R. H. Olley (University of Reading, UK). Samples were prepared for TEM using the permanganic etching method developed by Bassett and Olley[14] or a modification of the same procedure.[15] In both cases, a smooth surface in the 1-2 plane is created by a diamond knife and then brought into relief by etching; the resulting topography is replicated using cellulose acetate, which is then shadowed and coated with carbon. The cellulose acetate is then removed by solvent extraction, and the replica is examined using transmission electron microscopy. In the original procedure,[14] etching is performed by vigorously shaking the sample with a 0.7% w/v solution of potassium permanganate in a mixture of 2 volume parts concentrated sulphuric acid and 1 part phosphoric acid for 30 minutes and the shadowing is performed using platinum-carbon. In the modified procedure,[15] etching is performed by vigorously shaking the sample in a 1% solution of potassium permanganate in a mixture of 10 volume parts concentrated sulphuric acid, 4 parts orthophosphoric acid (85%), and 1 part water for 60 minutes and the shadowing is performed using tantalum-tungsten. Compared with the previous method, the modified etchant is better for revealing fine lamellar detail.

5.3 Results

The evolution of crystallinity and its transient orientation distribution in PP-300/6 sheared at T_{cryst} = 141°C for 12 s at a wall shear stress of 0.06 MPa is monitored using *in-situ* synchrotron WAXD. We begin by examining the two-dimensional WAXD patterns generated *in-situ* as the polymer crystallizes.

Shearing PP-300/6 at a wall shear stress of 0.06 MPa for 12 s at T_{cryst} = 141°C gives rise to a strongly oriented fiber-like diffraction pattern (Figure 5.1). This pattern appears during shear (Figure 5.1 a) and is essentially unchanged in shape at much longer times (t_{cryst} = 1200 s, Figure 5.1 b). A very weak near-isotropic ring is observed for the 110 peak at 1200 s, resulting from a small fraction of crystallites that are not highly oriented. The bimodal[16–18] diffraction patterns in Figure 5.1 are characteristic of the monoclinic crystalline unit cell of the α phase. This distinctive pattern is unique to isotactic polypropylene and is attributed to the crystallographic branching of "daughter" lamellae growing epitaxially with their a and c axes parallel to the c and a axes of the "parent" lamellae respectively.[14,19–24] The diffraction patterns in Figure 5.1 may be interpreted in view of the uniaxial symmetry evident *ex-situ* by polarized optical microscopy,[33] and can be explained in terms of parent lamellae that have their chain (c) axis aligned along the flow direction with a uniaxial distribution about that direction and the b axes of parent and daughter lamellae parallel (Figure 5.2). It has been suggested in the literature[25,26] that the imposition of shear on isotactic polypropylene leads to an increased tendency to form the β crystal phase. However, in our experiments, the hexagonal diffraction pattern characteristic of the β phase[27,28] is not observed. Further, neither the γ phase[26] nor the mesomorphic phase[29,30] are observed.

Two-dimensional WAXD patterns (such as those in Figure 5.1) can be circularly averaged to generate plots of diffracted intensity as a function of the scattering vector q ($= \frac{4\pi}{\lambda}\sin\theta$) where λ is the wavelength of the radiation used and 2θ is the scattering angle (Figure 5.3). Well established unit cell parameters for the α form of isotactic polypropylene (a = 6.65 Å, b = 20.96 Å, c = 6.5 Å, $\beta = 99°80$)[27,31] can be used to index the crystalline reflections as indicated in Figure 5.3. The absence of a clearly resolved feature at q = 1.14Å^{-1} (where the 300 peak of the β phase is expected to appear) indicates that no detectable β crystals are present. At T_{cryst} = 141°C , crystalline WAXD peaks appear by the end of ten seconds of shear (our time resolution in this data set is limited by the acquisition time, which was set to 10 s; other experiments at this T_{cryst} and σ_w show that WAXD peaks emerge during the first 5 s of shearing; note that at this T_{cryst}, the quiescent crystallization time by optical methods is on the order of 10^4 s, Figure 3.2). The peaks grow rapidly until $\approx$ 100 s (Figure 5.3), after which they "saturate" and grow relatively slowly (Figure 5.3, inset). This accords well with our *in-situ* rheo-optical turbidity data.[33] The time scale for the level of crystallinity to "saturate" corresponds to the time taken for the sheared polymer to become turbid.

This "saturation" behavior is also seen in the azimuthal scans at the 110 peak (Figure 5.4), which show a rapid initial increase in amplitude followed by a more gradual change. Furthermore, since the parent and daughter peaks are resolved in azimuthal angle, their respective full widths at half maximum (FWHM) can be used to qualitatively assess the orientation distribution of the two populations (Figure 5.5).

The FWHM for the parent and daughter peaks do not change significantly with time (Figure 5.5) indicating that the orientation distribution of anisotropic crystallites set up during shear (12 s) does not change substantially up to 1200 s. The fraction of daughter crystals relative to the parent population is proportional to the ratio of the areas under the respective peaks.[32] This area ratio is also roughly constant (Figure 5.5) with time up to 1200 s.

The sheared sample is quenched into cold water at about 1200 s, much after the time for the rapid growth in crystallinity to "saturate." The sample is then sectioned and the 1-2 surface is examined by TEM using the method developed by Bassett and Olley.[14] A low magnification image shows an oriented morphology in the skin layer that transitions sharply into a region that has anisotropic spherulitic structures (Figure 5.6). At greater depths, the spherulites become progressively more isotropic and larger in size. The skin region extends for about 60μm (the grid bar in Figure 5.6 obscures part of the skin). We infer that the oriented structures in the skin have uniaxial symmetry since polarized optical microscopy[33] reveals the skin is birefringent in the 1-2 plane and isotropic in the 2-3 plane. Thus, the skin is comprised of row nucleated structures extending in the flow direction. Similar structures have been observed in the skin layers in the experiments of Liedauer et al.[11] and also by White and Bassett.[34] The spacing between the line-like structures, d_{line}, observed increases from the wall inwards. The region of the skin near the walls was examined at a higher magnification (Figure 5.7) to determine an inter-line spacing, $d_{line} \approx 260$ nm in the outer 15 microns of the oriented skin. Due to the dense crystalline morphology in this region, the detailed structure of the line like features could not be observed. In a region of the skin further away from the wall, near the boundary with the less oriented region (Figure 5.8), the lines were less dense ($d_{line} \approx 700$ nm). The lamellae that grow perpendicular to the line-like features are clearly evident and show an interlamellar spacing of about 30 nm. Cross hatched lamellar branches can also be observed in some regions.

5.4 Discussion

The present X-ray and electron microscopy experiments aim to answer specific questions raised by rheo-optical observations made during flow and subsequent crystallization of the present sample under these specific conditions. Rheo-optical results presented in Chapter 3 (Figure 3.4) indicate that a long-lived, oriented structure is induced during shear of PP-300 at the present conditions of T_{cryst}, σ_w and t_s; however, birefringence measurements do not enable identification of this structure (e.g., discriminating between anisotropic density fluctuations, an oriented rotator phase, or a particular crystalline morphology of iPP). The observed correlation between the induction of this type of anisotropic structure *during* shear and the growth of anisotropic crystallites after cessation of flow manifested in a large birefringence suggests some sort of templating of the orientation of the crystallites formed after flow by the long-lived structure created during flow; however, the optical data cannot suggest the mechanism of templating. The development of turbidity, sufficient to effectively extinguish the transmitted beam of light in the rheo-optical experiments, occurs at approximately 100 s; this indicates the development of a crystalline microstructure that strongly scatters visible light, but does not provide information on the morphology of this microstructure or the extent of crystallization. Once the transmitted beam is extinguished, no further information can be gained using these *in-situ* optical measurements. *Ex-situ* polarized optical microscopy gives some information on the region of the sample that might be responsible for the optical anisotropy observed during the first 100 s. The 55 micron-thick oriented skin that is observed in the resulting images provides an upper bound on the thickness of the region that contributes to the large birefringence observed in real time during crystallization; however, polarized optical microscopy does not allow us to more quantitatively describe the orientation distribution of the crystallites, nor the morphological arrangement of the semicrystalline microstructure within the oriented layer.

in-situ WAXD data presented here show that crystallinity develops during shear, indicating that the birefringent precursor observed in the rheo-optical experiments is crystalline α isotactic polypropylene. The crystals that grow after shear cessation retain the orientation distribution that develops during shear indicating that the crystalline precursor formed during flow templates crystal growth after shear cessation. After the initial rapid increase in the crystallinity, the WAXD peaks "saturate" at about 100 s. This accords well with the time scale for turbidity manifested in the rheo-optical experiments. *ex-situ* TEM and optical microscopy[33] provide us with a morphological interpretation of the WAXD "saturation" and rheo-optical turbidity. "Saturation" of WAXD occurs due to the impingement of lamellae that are nucleated on uniaxial thread-like precursors in the skin, growing out radially. The spacing between these thread-like structures (260 tp 700 nm) is on the order of the wavelength of the light used in the rheo-optical experiments explaining why they scatter strongly and cause the development of strong turbidity in $\sim$ O(100 s). In this section, we discuss these observations and their implications for a geometric model of shear enhanced crystallization.

One of the remarkable features of our data is that the orientation distribution of crystallites growing from the thread-like precursors that formed during shear does not change even after the cessation of shear. The uniaxial orientation in the skin layer leads to a separation of the diffraction from parent and epitaxial daughter crystallites for some reflections which can be exploited to determine the ratio of the individual crystal populations and their orientations. Branched daughter peaks develop at the same time as the parent peaks (within the resolution of our experiment) and grow in proportion as the sample crystallizes. Electron micrographs show that the less oriented layer that is observed adjacent to the oriented "skin" has a very different lamellar orientation distribution from the skin (Figure 5.6). Therefore, the observation that the orientation distribution of the crystallites remains essentially unchanged during the first 1200 s implies that little crystallization occurs in the less oriented regions on a timescale of O(10^3 s). That only a small amount of crystallinity develops in the core regions over this time (which experience very low shear strain rates[35]) accords well with our quiescent *in-situ* WAXD and turbidity measurements[33,36] (quiescent crystallization time, $t_Q \approx 10^4$ s). Thus, we interpret the optical and X-ray signals during the first 1200 s as arising predominantly from the outermost 60μm skin region near each wall of the shear cell. The "saturation" of the crystallinity after 100 s suggests that crystallization of these outer layers reaches very nearly its ultimate extent at 141°C within approximately 100 s.

A physical explanation for the rapid "completion" of the skin (in one hundredth of t_Q) and the correlation between the turbidity and WAXD crystallization times (both $\sim$ 100 s) emerges from the morphology of the skin seen in the electron micrographs. The spacing between the shear lines in the skin increases from about 260 nm near the wall of the flow cell to about 700 nm near the inner boundary. The time taken for crystals growing radially from lines separated by 700 nm to impinge can be estimated to be around 105 s using a literature value for the linear growth rates of α iPP $\approx$ 0.2 μm/min at T $\approx$ 140°C (obtained from quiescent DSC studies of polymers with similar levels of tacticity[37,26] to PP-300/6). Use of the quiescent value for the linear growth velocity is justified since it has been shown that the growth velocity of crystals is unchanged by the imposition of flow[38] or a change in the nucleation geometry.[34] An impingement time of 105 s agrees remarkably well with the duration of the initial rapid growth in crystallinity from our WAXD data, and suggests that the thread-like precursors generated during shear nucleate the growth of oriented crystals in the skin. Even though the growth velocity of lamellae in row structures is not discernibly different from that in spherulites, the simple geometrical factor of growing from row nuclei means that the cylindrical semicrystalline structures that result will tend to occupy a larger volume fraction–even when the row nucleation is sparse and of similar spacing to that of the spherulites.[34] These crystals then grow at their quiescent growth rate until they impinge.

The resemblance between the oriented crystallites observed in injection molding or fiber extrusion experiments and the shear experiments described here and in the literature[11] is striking. The crystalline structures observed in the skin region in our samples are similar to the row nucleated shish kebab structures typically observed in the "shear zone" in injection molded samples.[9,17,39–41] It is commonly believed that the fibrillar nuclei for these oriented crystals are created by the extensional fountain flow at the advancing flow front as the mold is filled. The oriented crystallites in our experiments also resemble those present in high modulus polyethylene fibers studied by Keller and coworkers among others.[3,42,2] In their studies, oriented crystal precursors were produced in the extrusion direction due to extensional flow imposed on polyethylene; these served as row nuclei for lamellae that grow out from the central precursor until they impinge, leading to the formation of high modulus materials. Since extensional flows are excluded by the short term shearing experimental protocol, these experiments, in accord with earlier work by Liedauer et al.,[11] demonstrate that shear is sufficient for the formation of these oriented crystallites. The fact that thread-like precursors can be generated by various flows and that there is a sharp skin to core transition (Figure 5.6) suggests that their formation is governed by a "critical" configurational distortion of the melt.[12,43–46]

Our experiments argue for rheological control of the formation of the oriented skin: (i) the skin has uniaxial symmetry (*ex-situ* optical micrographs[33]) with row nucleated structures growing along the flow direction (TEM presented here); (ii) the temperature dependence of creation of the oriented precursors follows that of the melt rheology – in stark contrast to the temperature dependence of quiescent crystallization.[33] Taken together, these results indicate that chain elongation in the flow direction generated during flow governs the morphological and kinetic transition to skin formation. In rheological terms, the primary normal stress difference plays a dominant role, in accord with the strong nonlinearity of flow-induced effects. Further, this suggests a molecular perspective on the role of chain length polydispersity which strongly affects the generation of skin-core morphologies.[13] When flow is imposed on a polymer with a broad distribution of molecular weights, high overall deformation rates can be accessed since the average chain length, and consequently, the viscosity are modest. This deformation rate is fast compared to the relaxation time of the longest chains, causing their conformation to become particularly distorted. These chains, which become elongated in the flow direction, appear to play a critical role in the cascade of events that leads to the row nucleated structures.

The data presented here supports the physical picture captured by the phenomenological model of Liedauer et al.[11] Thread-like precursors oriented in the flow direction are generated during shear. These precursors lead to the formation of oriented lamellae with their chain axes along the flow direction that grow radially from these lines until they impinge. In isotactic polypropylene, the α parent lamellae are also accompanied by the associated daughter lamellae. However, the molecular variables that control the density of these lines, their generation and relaxation rates, and the "critical" shear stress that leads to oriented growth are not fully understood. Experiments with model systems that are underway in our laboratory hold promise for providing important clues regarding these unsolved puzzles.

5.5 Conclusions

By observing the growth of the oriented skin induced by a brief "pulse" of shear, we not only see that the crystallization of the skin is essentially completed in roughly 1% of the quiescent crystallization time (for the present conditions), but further gain insight into how this rapid "completion" occurs. In a matter of seconds, thread-like precursors are generated during shear in the high stress regions (less than about 55 microns from the wall); these thread-like precursors develop with a high density (a mere 250 to 700 nm apart). Primary lamellae are nucleated on these threads and forced to grow radially (with little non-crystallographic splaying) due to the geometric constraint imposed by the dense lateral packing of lamellae. Consequently, the orientation distribution created during flow persists to the point where lamellae from adjacent thread-like precursors impinge. Thus, we have been able to observe in real time the events that have been hypothesized to explain the row nucleated morphology since Keller and Machin.[12]

By the end of the shear pulse (12 s), the relative degree of crystallinity in the skin reaches 20% of its saturated value which is reached in 100s; thereafter it remains nearly constant to over 1000s. The saturated degree of crystallinity reflects a densely crystallized, fully impinged structure. The time for impingement accords with literature values of the quiescent growth velocity.

The strong orientation of the crystallites exposes the interesting fact that cross hatched lamellae appear almost immediately, growing simultaneously and in proportion to the parent lamellae.

5.6 Summary

In-situ synchrotron WAXD was used to follow crystallization in a polydisperse isotactic polypropylene during and after a brief interval of shear under isothermal conditions. A specific flow history was selected from the range that induces a highly oriented skin core morphology.[33] At the chosen crystallization temperature ($T_{cryst} = 141°C$, characteristic time for quiescent crystallization, $t_Q \sim 10^4$ s), crystalline WAXD peaks emerge during the brief interval of shear ($\sigma_w = 0.06$ MPa, $t_s = 12$ s) showing a highly oriented fiber-like diffraction pattern; primary lamellae with c-axis orientation were present, along with their associated crosshatched daughter lamellae. The crystallinity grew rapidly during the next 100 s ($\sim 10^{-2} t_Q$) after cessation of shear, and very slowly after that. Further, for the first 1200 s, the orientation distribution did not change from that generated during the shear pulse. *ex-situ* transmission electron microscopy showed a characteristic skin-core morphology with a thin skin region consisting of oriented crystallites near the walls of the shear device, adjacent to weakly anisotropic spherulites farther from the walls. This indicates that the *in-situ* WAXD arose from crystallites in the oriented skin. The skin consisted of densely nucleated thread-like line structures from which α-phase crystalline lamellae radiated. The spacing between the row nuclei in the skin increased as a function of distance from the wall of the shear device. Our data suggest that the lamellae grow from a central thread until they impinge at about 100 s to form the dense crystalline structure in the skin.

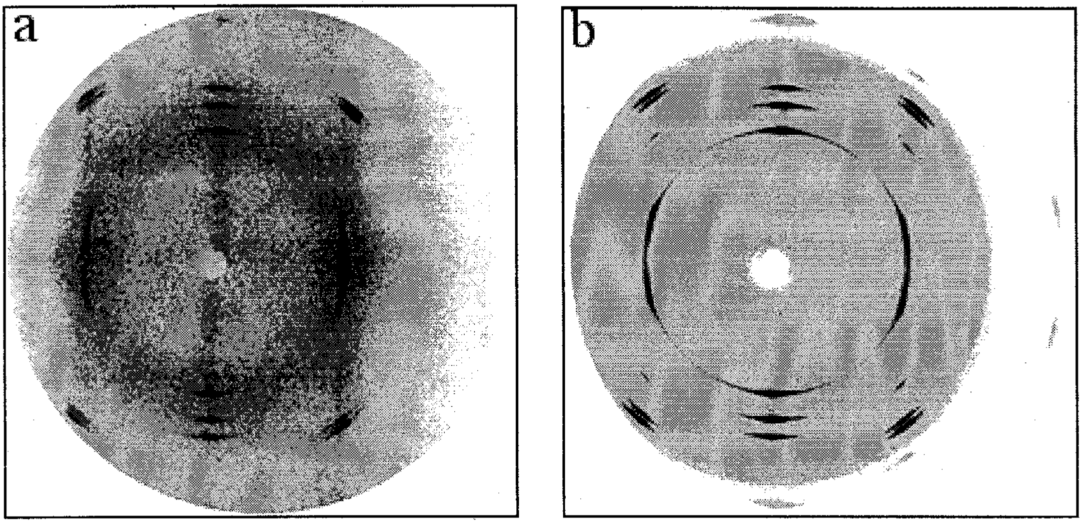

Figure 5.1: *In-situ* two-dimensional WAXD patterns obtained as PP-300/6 crystallizes under shear (T_{cryst} = 141°C, σ_w = 0.06 MPa, t_s = 12 s). The flow direction is horizontal. (a) is obtained by acquiring data for 10 s as the polymer is being sheared and (b) is the diffraction pattern obtained at t_{cryst} = 1200 s using an acquisition time of 40 s. The data have been normalized for acquisition time; the normalized intensity at the 040 peak is 85 for (a) relative to 518 for (b).

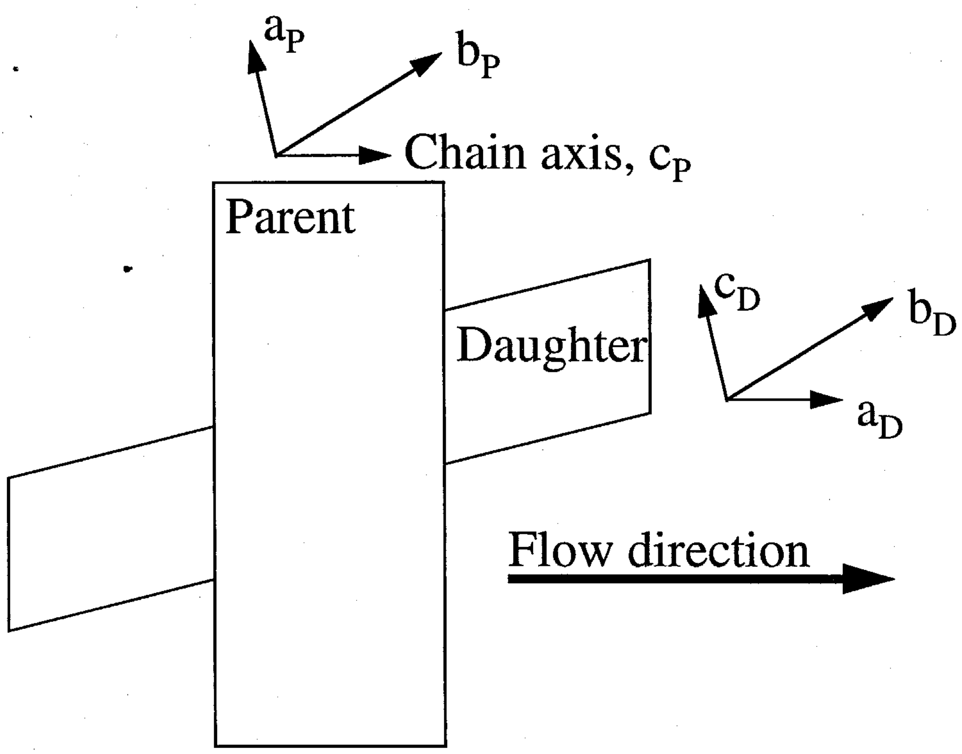

Figure 5.2: A schematic model for the alignment of the parent and daughter lamellae in the oriented crystallites that explains the diffraction patterns in Figure 5.2 (see text). The crystallites have uniaxial symmetry about the flow direction.

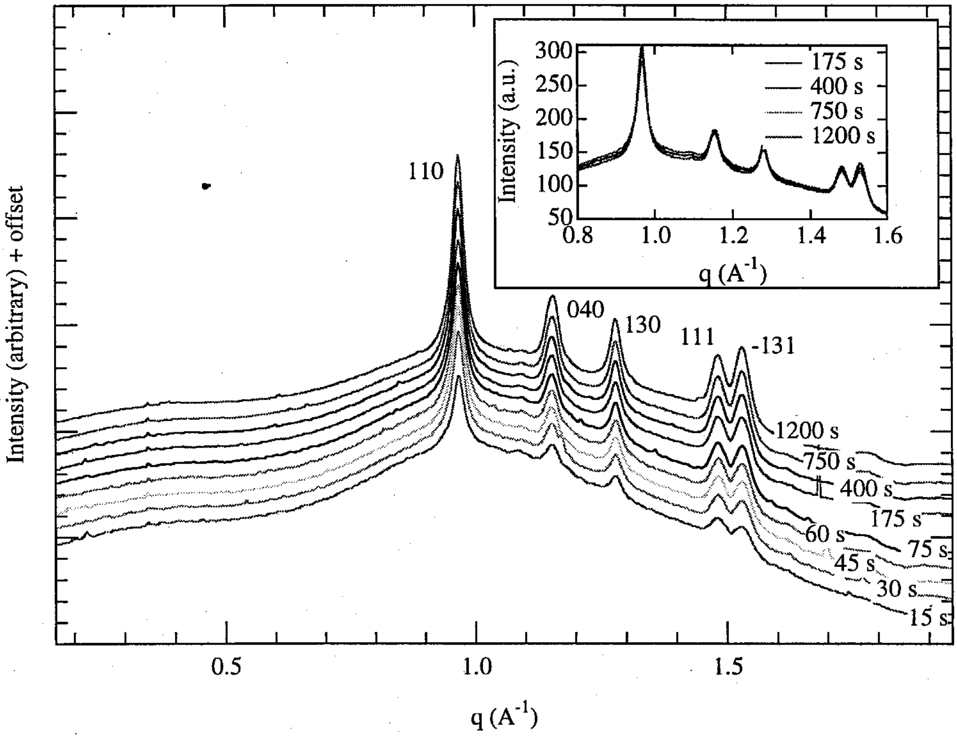

Figure 5.3: As PP-300/6 crystallizes, the evolution of crystallinity can be monitored using circularly averaged "powder" patterns, normalized for data acquisition time. The data is vertically offset for clarity. The inset shows scans at t_{cryst} = 175 s, 400 s, 750 s and 1200 s without an offset.

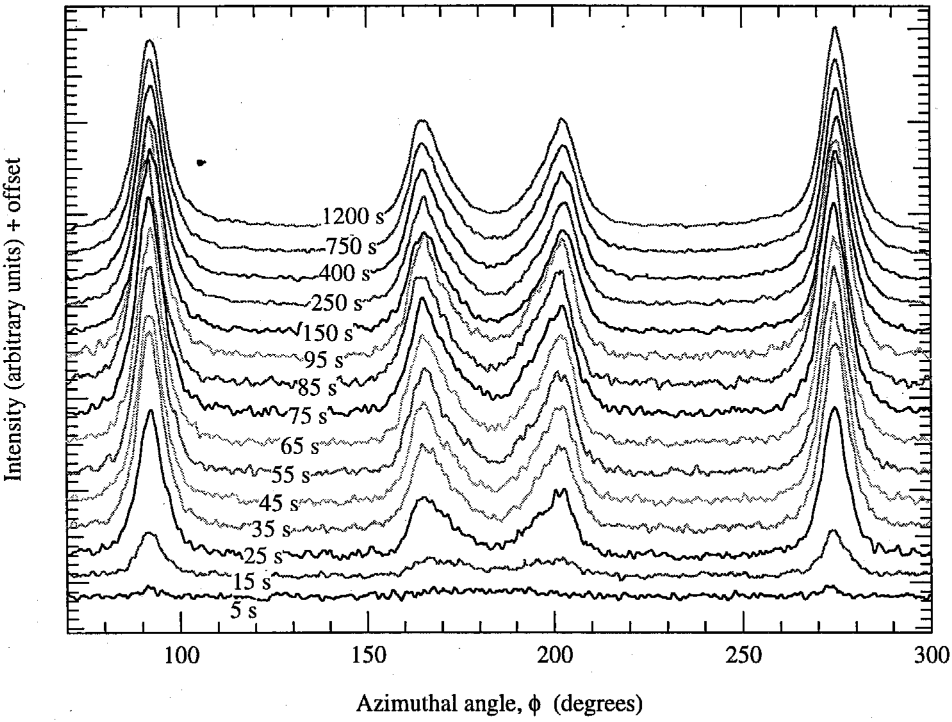

Figure 5.4: Azimuthal scans at the 110 peak show the change in the crystallinity and the orientation distribution of crystallites as PP-300/6 crystallizes. The data is scaled for acquisition time and vertically offset for clarity.

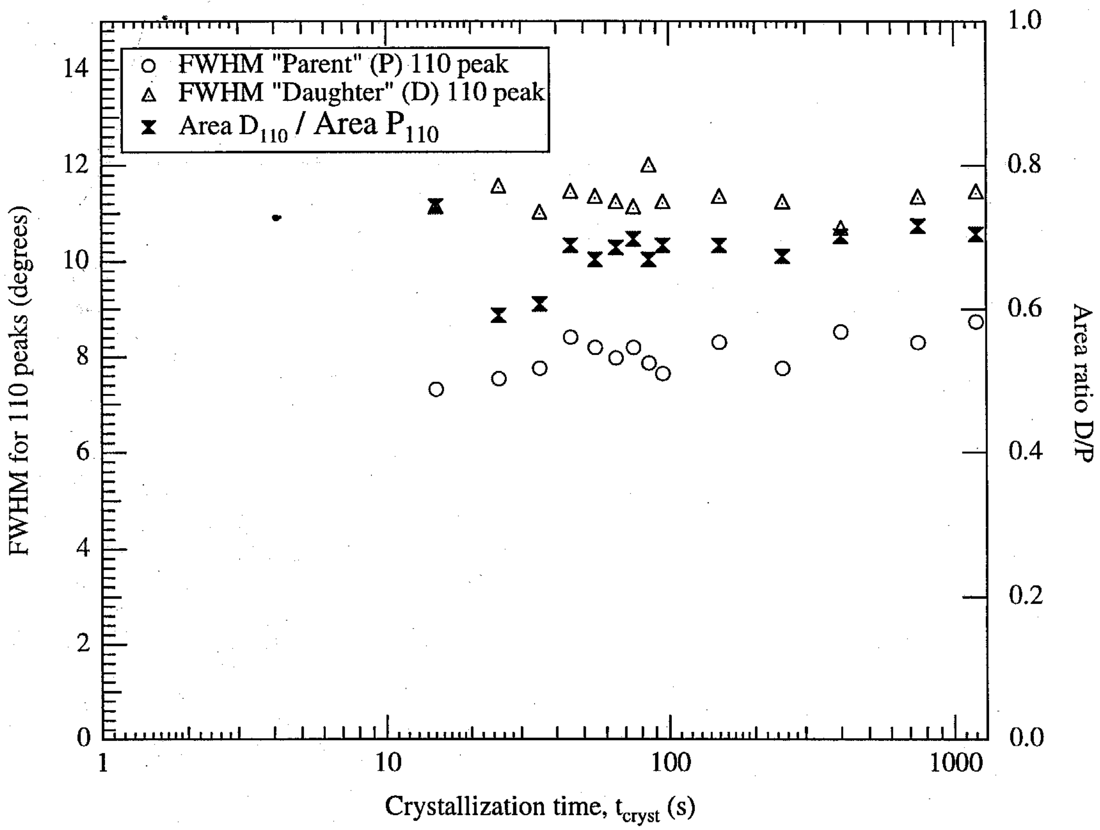

Figure 5.5: Characteristics of the orientation distributions: the full width at half maximum (FWHM) for parent and daughter peaks and the ratio of the areas under daughter and parent peaks as a function of time. The first data point is at 15 s.

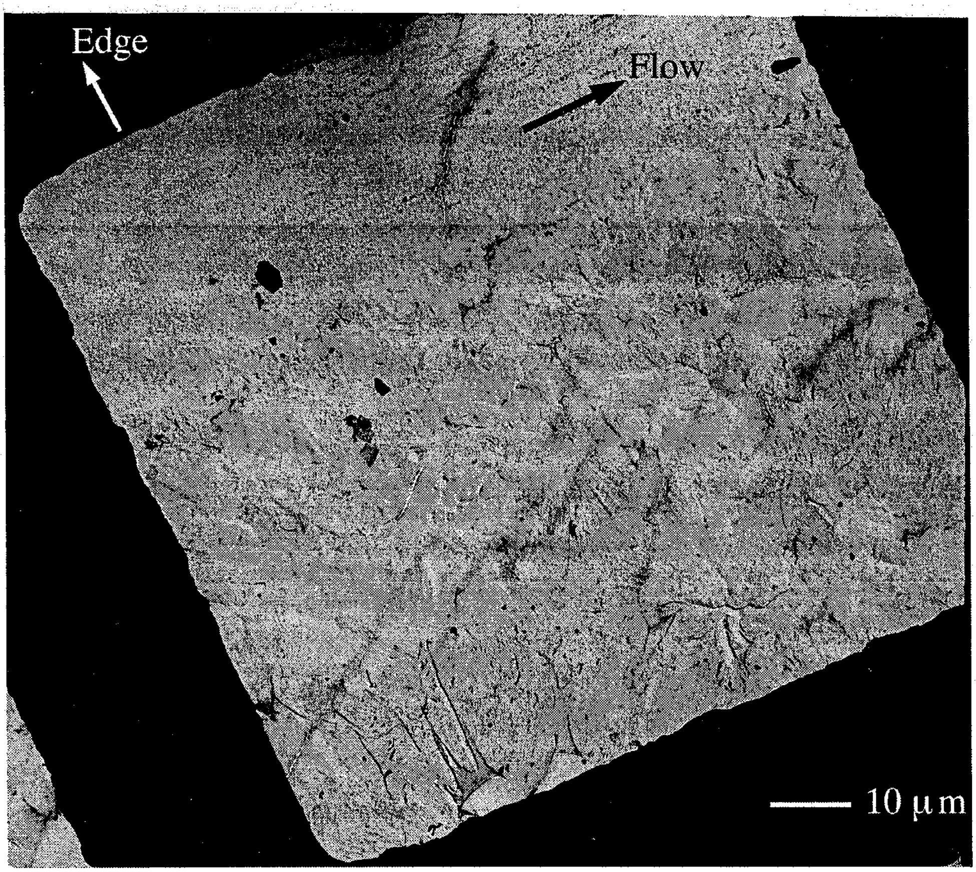

Figure 5.6: A low magnification TEM that shows the skin-core structure in shear crystallized PP-300/6. Note that the transition from the oriented skin region to the less oriented region appears sharp even at this magnification. The modified etching procedure was used to prepare the replica for this TEM image (see Experimental section).

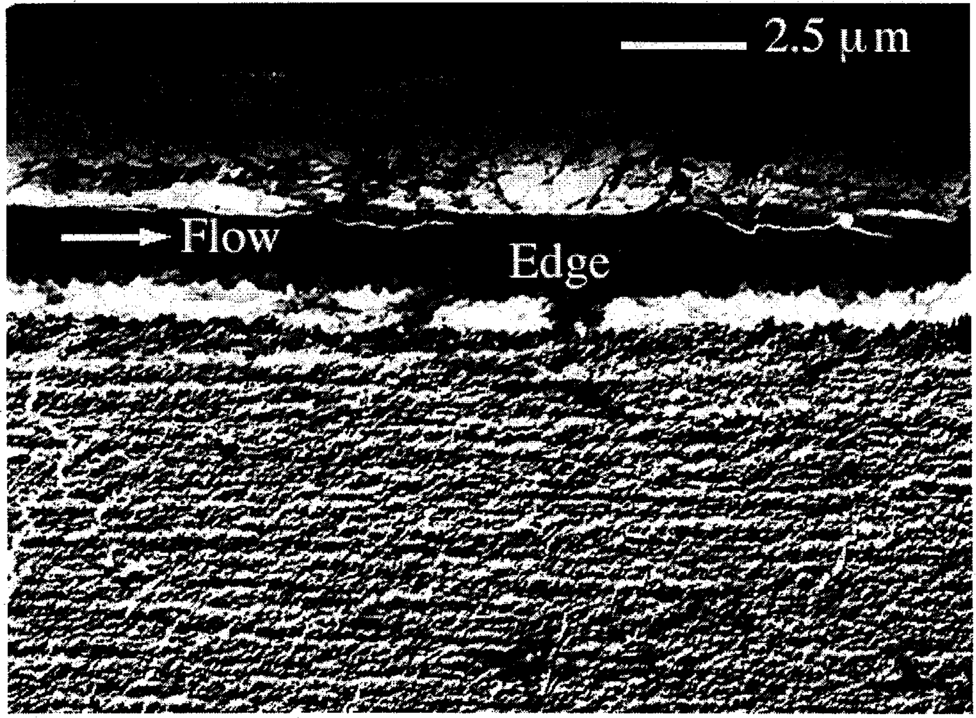

Figure 5.7: A magnified image of the oriented skin near the edge of the sample. The inter-line spacing, d_{line}, is about 260 nm in this image. The Bassett and Olley etching procedure was used to prepare the replica for this TEM image (see Experimental section).

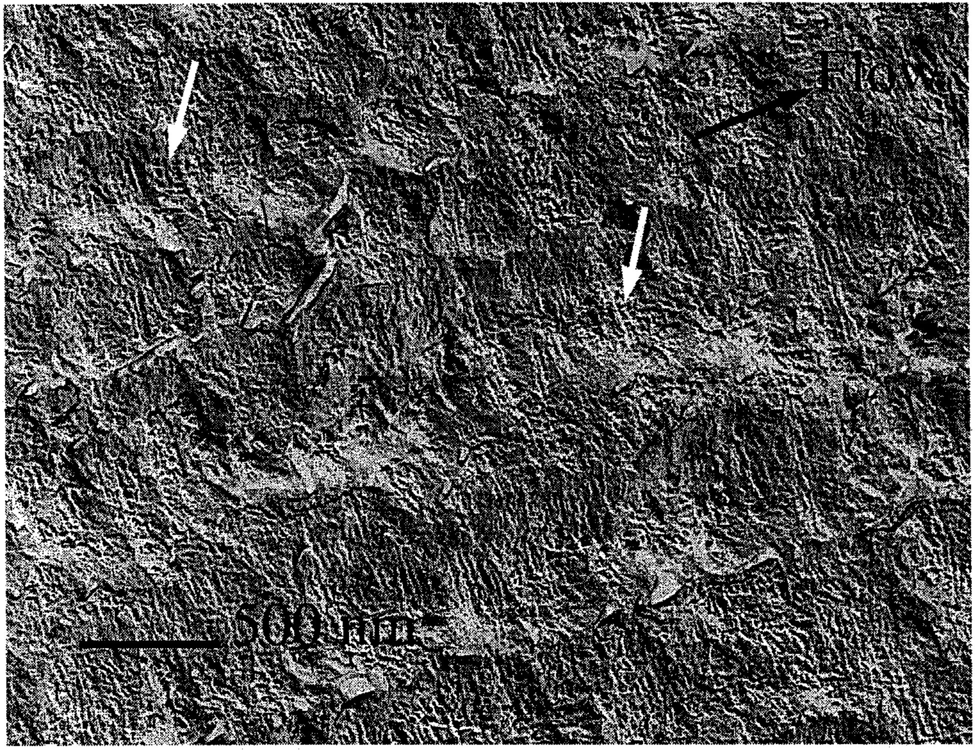

Figure 5.8: A magnified view of the oriented skin far from the sample edge, near the transition to unoriented structures, shows details of the lamellar structures in the skin. The primary lamellae are perpendicular to the flow direction. The inter-line spacing, $d_{line} \approx 700$ nm. The white arrows indicate regions where cross-hatching is apparent. The Bassett and Olley etching procedure was used to prepare the replica for this TEM image (see Experimental section).

Bibliography

1. Binsbergen, F. L. *Nature* **1966,** *211,* 516.

2. Southern, J. H.; Porter, R. S. *J. Appl. Polym. Sci.* **1970,** *14,* 2305.

3. Odell, J. A.; Grubb, D. T.; Keller, A. *Polymer* **1978,** *19,* 617.

4. Mencik, Z.; Fitchmun, D. R. *J. Polym. Sci. (Polym. Phys.)* **1973,** *11,* 973.

5. Fitchmun, D. R.; Mencik, Z. *J. Polym. Sci. (Polym. Phys.)* **1973,** *11,* 951.

6. Peterlin, A. *Colloid Polym. Sci.* **1987,** *265,* 357-382.

7. Gupta, R. K.; Auyeung, K. F. *J. Appl. Polym. Sci.* **1987,** *34,* 2469.

8. Ulcer, Y.; Cakmak, M. *Polymer* **1997,** *38,* 2907.

9. Fujiyama, M.; Wakino, T.; Kawasaki, Y. *J. Appl. Polym. Sci.* **1988,** *35,* 29.

10. Fujiyama, M.; Wakino, T. *J. Appl. Polym. Sci.* **1991,** *43,* 57.

11. Liedauer, S.; Eder, G.; Janeschitz-Kriegl, H.; Jerschow, P.; Geymayer, W.; Ingolic, E. *Intern. Polym. Proc.* **1993,** *8,* 236.

12. Keller, A.; Machin, M. J. *J. Macromol. Sci. (B)* **1967,** *1,* 41.

13. Meijer, H., Ed.; *Processing of Polymers,* Vol. 18 VCH (NY): 1997.

14. Bassett, D. C.; Olley, R. H. *Polymer* **1984,** *25,* 935.

15. Shahin, M. M.; Olley, R. H.; Blissett, M. J. *J. Polym. Sci. Part B (Polym. Phys.)* **1999,** *37,* 2279.

16. Andersen, P. G.; Carr, S. H. *J. Mater. Sci.* **1975,** *10,* 870.

17. Clark, E. S.; Spruiell, J. E. *Polym. Eng. Sci.* **1976,** *16,* 176.

18. Masada, I.; Okihara, T.; Murakami, S.; Ohara, M.; Kawaguchi, A.; Katayama, K. I. *J. Polym. Sci. (Polym. Phys.)* **1993,** *31,* 843.

19. Padden, F. J. (Jr.); Keith, H. D. *J. Appl. Phys.* **1966,** *37,* 4013.

20. Padden, F. J. (Jr.); Keith, H. D. *J. Appl. Phys.* **1973,** *44,* 1217.

21. Binsbergen, F. L.; DeLange, B. G. M. *Polymer (London)* **1968,** *9,* 23.

22. Lovinger, A. J. *J. Polym. Sci. (Polym. Phys.)* **1983,** *21,* 97.

23. Lotz, B.; Wittmann, J. C. *J. Polym. Sci. (Polym. Phys.)* **1986,** *24,* 1541.

24. Norton, D. R.; Keller, A. *Polymer* **1985,** *26,* 704.

25. Wenig, W.; Herzog, F. *J. Appl. Polym. Sci.* 1993 **50,** 2163.

26. Karger-Kocsis, J., Ed.; *Polypropylene,* vol. 1. Structure and Morphology Chapman and Hall: 1995.

27. Lotz, B.; Wittmann, J. C.; Lovinger, A. J. *Polymer* **1996,** *22,* 4979.

28. Dorset, D. L.; Court, M. P.; Kopp, S.; Schumacher, M.; Okihara, T.; Lotz, B. *Polymer* **1998,** *39,* 6331.

29. Natta, G.; Corradini, P. *Nuovo Cimento (Suppl.)* **1960,** *15,* 40.

30. Corradini, P.; Petraccone, V.; Rosa, C. D.; Guerra, G. *Macromolecules* **1986,** *19,* 2699.

31. Jones, A. T.; Aizlewood, J. M.; Beckett, D. R. *Makromol. Chem.* **1964,** *75,* 134.

32. Dean, D. M.; Rebenfeld, L.; Register, R. A.; Hsiao, B. S. *J. Mater. Sci.* **1998,** *33,* 4797.

33. Kumaraswamy, G.; Issaian, A. M.; Kornfield, J. A. *Macromolecules* **1999,** *32,* 7537.

34. White, H. M.; Bassett, D. C. *Polymer* **1997,** *38,* 5515.

35. Nonlinear viscoelastic data obtained using a capillary rheometer indicate that PP-300/6 is shear thinning with a power law exponent of 0.38. Under pressure driven flow, a blunted velocity profile develops with high strain rates near the walls and much lower strain rates as we move away from the wall.

36. Kumaraswamy, G.; Verma, R. K.; Issaian, A. M.; Wang, P.; Kornfield, J. A.; Yeh, F.; Hsiao, B. S.; Olley, R. H. submitted to *Polymer.*

37. Janimak, J. J.; Cheng, S. Z. D.; Giusti, P. A.; Hsieh, E. T. *Macromolecules* **1991,** *24,* 2253.

38. Wolkowicz, M. *J. Polym. Sci. (Polym. Symp.)* **1978,** *63,* 365.

39. Kantz, M. R.; Jr., H. D. N.; Stigale, F. H. *J. Appl. Polym. Sci.* **1972,** *16,* 1249.

40. Folkes, M. J.; Russell, D. A. M. *Polymer* **1980,** *21,* 1252.

41. Kalay, G.; Bevis, M. *J. Polym. Sci. (Polym. Phys.)* **1997,** *35,* 265.

42. Bashir, Z.; Odell, J. A.; Keller, A. *J. Mater. Sci.* **1984,** *19,* 3713.

43. Hill, M.; Keller, A. *J. Macromol. Sci. (Phys)* **1971,** *B5,* 591.

44. Keller, A.; Kolnaar, H. W. H. Processing of Polymers. In Vol. 18; Meijer, H. E. H., Ed.; VCH: 1997; Chapter Flow Induced Orientation and Structure Formation.

45. McHugh, A.; Guy, R.; Tree, D. *Colloid Polym. Sci.* **1993,** *271,* 629.

46. Bushman, A. C.; McHugh, A. J. *J. Appl. Polym. Sci.* **1997,** *64,* 2165.

47. Meijer, H., Ed.; *Processing of Polymers,* Vol. 18; VCH (NY): 1997.

Chapter 6 Analysis of *In-situ* Synchrotron X-ray Data

6.1 Introduction

The properties of a semicrystalline polymer product are determined by the level of crystallinity and the hierarchical arrangement of crystallites[1] at the unit cell (Å-scale), lamellar (nano-scale) and gross macroscopic-level (micron-scale). In isotactic polypropylene, for example, it is well known[2] that the unusually long flex life of injection molded hinges is due to the unique epitaxially-branched morphology[3,4] (also called crosshatching) exhibited by the α-crystalline form. Thus, it is reasonable to expect that the frequency and extent of crosshatching influence the mechanical properties of the final product, and it is of great interest to ascertain the factors that determine crosshatch density and the spatial distribution of the lamellar branches. *Ex-situ* investigations of quiescently crystallized samples suggest[5] that the nucleation geometry (point-like versus surface versus line-nucleation, i.e., spherulitic, transcrystalline or row-nucleated) does not influence the lamellar thickness or cross hatching frequency in the crystallites. However, the influence of flow history on crosshatching has not been investigated.

Other interesting aspects of processing-induced structure development in semicrystalline polymers also remain incompletely understood, making it very challenging to realistically model processing operations. For example, during injection molding, the crystallizing polymer experiences spatially-dependent levels of stress and total accumulated strain that could lead to undesirable skin-core morphologies.[6,7] Further, processing operations are typically nonisothermal[8]: crystallinity develops in films as they cool during blowing,[9,10] and in extrusion, as the hot polymer melt contacts the cold walls of the mold during filling.[7,11,12] Therefore, there is a need for well defined experiments to separately characterize the roles of flow history and crystallization temperature in the development of semicrystalline morphology, before we can understand their cumulative effect. Our previous investigations revealed that the transition to oriented growth during flow-induced crystallization is mediated through a rheologically-controlled kinetic pathway (Chapter 4). Thus, the critical anisotropic chain configuration required to generate precursors to anisotropic crystallites is accessed at earlier times after start-up of flow at higher temperatures.[13] However, the consequences of the generation of these precursors on the temperature-dependence of subsequent morphological development remain to be investigated. Therefore, this chapter examines the effects of stress, duration of shear and temperature on the crystallization kinetics and morphology development.

X-ray scattering[14,15] provides a tool to characterize the semicrystalline microstructure from the unit cell level (Wide angle X-ray Diffraction, WAXD) to the ordering of lamellar stacks (Small Angle X-ray Scattering, SAXS). Intense X-ray radiation available at synchrotron sources, having photon fluxes roughly two orders of magnitude higher than conventional laboratory rotating anode sources, reduce the data aquisition time required to achieve reasonable signal to noise, and permit us to acquire time-resolved information about the evolution of structure *in-situ.*[16]

For semicrystalline polymers, WAXD can be used to determine an estimate of the crystallinity by comparing the intensity of the crystalline peaks from the sample to those from standards (external comparison), or from the ratio of the crystalline peak intensity to the amorphous halo (internal comparison).[14,15] Two-dimensional WAXD patterns can also be used to estimate the degree of orientation of the crystallites from an analysis of the distribution of intensity from the diffraction peaks along the azimuthal angle.[17]

SAXS is used to characterize semicrystalline morphology at a length scale on the order of 10 to 100 nm. The periodicity of semicrystalline lamellae (long spacing) can be determined based on the scattering angle at which the SAXS peak appears, while the integral intensity of SAXS scattering (called the invariant) is a measure of the crystallinity in a spatially homogeneous sample.[14,15] Examining the distribution of intensity along the azimuthal angle at the peak position for two-dimensional SAXS patterns provides information about orientation distribution of the lamellar stacks.

Thus, a wealth of information can be obtained by combining information from the *in-situ* evolution of SAXS and WAXD as a sample crystallizes and interpreting the scattering based on *ex-situ* morphological investigations using electron microscopy. While, crystallization of polymers under quiescent or near-quiescent conditions has been studied using a combination of synchrotron SAXS and WAXD,[18–20] there are very few studies in the literature that adopt this experimental approach to flow-induced crystallization. Recent work by Pople et al.[21] examined structural development in polyethylene subjected to shear under isothermal conditions, using a combination of *in-situ* WAXD and *ex-situ* TEM. They found that a high degree of orientation was observed in the final morphology when the polymer melt was subjected to a shear rate above a critical value. They noted that the formation of row nucleated structures observed in the TEM depends on the molecular weight distribution in the sample. Further investigations of this nature are required to elucidate the route to crystallization in polymers subject to flow, and to develop a model for the development of anisotropic crystalline structures.

In this Chapter, we focus on *in-situ* synchrotron SAXS and WAXD that complements our previous *in-situ* rheo-optical and *ex-situ* microscopy. We re-examine the shearing condition analyzed in detail in Chapter 5, that gives rise to a strongly oriented skin-core morphology to outline the method of data analysis used to extract structural information from the X-ray data. These methods are then used to examine the influence of shearing conditions (wall shear stress, shearing duration and crystallization temperature) on the development of semicrystalline morphology. Finally, we examine the implications of the combination of *in-situ* rheo-optics and X-ray scattering with *ex-situ* microscopy for a mechanistic description of semicrystalline microstructure development in polymers subjected to flow.

6.2 Experimental

The effects of wall shear stress (σ_w), shearing duration (t_s) and crystallization temperature (T_{cryst}) on development of semicrystalline morphology are studied using the short-term shearing approach[22,23] described previously (Chapter 3). We use *in-situ* synchrotron X-ray scattering (λ = 1.307 Å, to probe the development of semicrystalline order: both SAXS and WAXD are employed to elicit detailed structural information about the extent of crystallization and its orientation.

The experimental setup for the synchrotron WAXD measurements is the same as in previous Chapters and is described in Section 4.2. The setup for small angle studies is similar to WAXD. Our modified shear cell has a conical aperture to enable observation of scattered X-rays to angles (2θ) of up to 35°, and the flow cartridge is sealed with 300μm-thick beryllium windows (see Figure 4.1). As before, the shear device is placed on a translation stage for ease of alignment. A liquid nitrogen cooled two-dimensional CCD detector (MAR-CCD) is used to acquire data for both small and wide angle experiments. An α-alumina NIST standard is used to calibrate the scattering angle for WAXD, while a silver behenate standard is used for SAXS. The CCD is placed about 16 cm from the shear cell for the WAXD measurements. For the SAXS, the CCD is placed at a distance of about a meter from the shear cell, and an evacuated chamber is used between the shear cell and the CCD to reduce air scattering.

All the synchrotron X-ray scattering experiments were conducted at beamline X-27C of the National Synchrotron Light Source (NSLS), at the Brookhaven National Laboratory, in collaboration with Prof. B. S. Hsiao and Dr. F. Yeh (both SUNY-Stony Brook), and Dr. R. Verma and P. Wang (Caltech).

6.3 Results

We begin this section with a detailed examination of synchrotron SAXS and WAXD data that trace the evolution of semicrystalline microstructure for a particular shearing condition that gives rise to anisotropic skin-core morphology (T_{cryst} = 141°C; σ_w = 0.06 MPa; t_s = 12 s; see Chapters 3,5). The method of analysis used to extract structural parameters is outlined, setting the stage for investigating the effects of shearing conditions (σ_w, t_s and T_{cryst}) on the time course of morphological development.

6.3.1 Analysis of Synchrotron SAXS and WAXD

Upon subjecting PP-300/6 to conditions severe enough to induce the formation of skin-core morphology, the crystallization kinetics are tremendously accelerated; highly oriented WAXD and SAXS patterns develop in a matter of seconds (Figure 6.1) at a temperature at which the characteristic time for quiescent crystallization (based on rheo-optical data[24]) is $t_Q \approx 10^4$ s. The two-dimensional WAXD patterns indicate the formation of a bimodal population of crystals – consisting of parent lamellae (showing c-axis orientation along the flow direction) and their associated epitaxial daughter lamellae (See Chapter 5). The strong uniaxial symmetry of the oriented crystals generated during flow is preserved as the polymer crystallizes after flow cessation (Figure 6.1 d, top row, t_{cryst} = 1200 s, analyzed in detail in Chapter 5).

Under these shearing conditions, the SAXS also develops a highly oriented pattern with lobes along the flow direction (Figure 6.1, bottom row). Faint second order peaks along the flow direction can be observed for data acquired over long acquisition times (viz. improved signal to noise ratio; Figures 6.1 c,d, bottom row) indicating the high degree of ordering of the oriented parent lamellae. Weak lobes due to scattering from the daughter lamellae can also be observed in the SAXS at about 80° to the flow direction. During the initial stages of crystallization, data is acquired with a time resolution of 10 s. Given this resolution, the development of SAXS and WAXD appear simultaneous.

Analysis of SAXS

Structural information can be extracted from the two-dimensional SAXS patterns by analyzing sections along different directions of interest: for example, the development of lamellar stacks with normals along the flow direction can be probed by examining a section in that direction, i.e., I(q) along the line marked F in Figure 6.1 c, bottom. Similarly, we also examine sections along the direction perpendicular to flow ($F_\perp$) and along the lobes from the daughter lamellae (D). Due to the large angle made by the daughter lobes with respect to the flow axis, their overlap contributes to the intensity along $F_\perp$; thus there is no substantial difference between analysis of data along $F_\perp$ and D. Comparing the growth of scattering intensity in these sections versus the circularly-averaged powder pattern provides information regarding the rate of development of oriented crystalline lamellae versus overall development of crystalline structure. The powder patterns are analyzed after performing the Lorentz correction which accounts for differences in scattered intensity based on the geometrical orientation of the scatterer. The Lorentz corrected intensity is given by $q^2 I_P$, where I_P is the raw circularly-averaged powder pattern data.

Analysis of the correlation function[25] or the interface distribution function[26,27] have been in the literature[28,29] used to obtain detailed structural information regarding the thickness of crystalline and amorphous stacks, and the nature of the crystal-amorphous interface. However, these methods typically assume a lamellar stack morphology with variation of electron density along one dimension. Applying these advanced methods of analysis to the α-form of isotactic polypropylene is complicated since the one-dimensional model is not applicable to the crosshatched morphology.[30] However, information regarding the long spacing and the invariant can be conveniently extracted.[31,32]

The position of the maximum in the SAXS intensity (q^*) is used to determine the long spacing, L_B ($= 2\pi/q^*$). As an example of our analysis we present data acquired at $t_{cryst} = 3250$ s (Figure 6.2). As expected, the long spacing determined from the Lorentz-corrected powder pattern is shifted to a lower value ($L_B = 25.4$ nm) compared to the uncorrected powder pattern (L_B = 29.2 nm). From the sections along the F, $F_\perp$ and D-directions (plotted on the same scale as each other), it is obvious that the SAXS peak intensity is much stronger along the F-direction, and therefore, dominates the powder-averaged pattern. Analysis of the F-section yields a value of L_B = 26.8 nm, similar to that from the Lorentz corrected powder pattern. Since the intensity of the SAXS peak along the $F_\perp$ and D-directions is comparable to the intensity around the beamstop, the peaks are not well resolved and appear as shoulders making it difficult to analyze the data along those sections. Thus, the uncertainty in our estimate of L_B = 28.9 nm along $F_\perp$ and D is large. As the polymer crystallizes after shear, the L_B calculated from the Lorentz-corrected powder pattern and from the F-section remains essentially constant (Figure 6.2, inset).

The SAXS patterns can also be used to obtain an estimate of the orientation distribution of the crystalline lamellae by examining the azimuthal intensity at the peak radial value. A Lorentzian peak shape was determined to give a good fit to the azimuthal data (Figure 6.3, inset shows an example of the fit). The full width at half maximum (FWHM) obtained from the fit increases gradually from about 6° to 8° indicating that the pronounced orientation of the parent lamellar stacks along the flow direction that develops during the 12 s of shear remains substantially unchanged to $t_{cryst} \approx$ 3000 s, after cessation of flow.

Having examined the geometrical aspects of the morphology such as the long spacing and degree of orientation, we now focus on the SAXS invariant and compare it to the WAXD crystallinity index (Figure 6.4). The invariant, $Q = \int_0^\infty I \, dq$ (where I is either the intensity along the F, $F_\perp$ or D-sections, or the Lorentz-corrected intensity of the circularly-averaged powder pattern) is a measure of the mean-square fluctuation of the electron density in a scattering system. For a spatially inhomogeneous lamellar two-phase sample such as in our experiment, Q is proportional to $< x_l(1 - x_l)\Delta\rho^2 >$ where x_l is the *local* crystallinity, $\Delta\rho$ is the electron density difference between the crystal and amorphous phases and $< .. >$ represents a spatial average over the scattering volume.[14,15] Since we cannot collect SAXS data over the entire q-range required to calculate the invariant ($0 \leq q \leq \infty$), in practice the data is extrapolated linearly to 0 at low q[29] and using Porod's law[14,15] in the limit $q \to \infty$. According to Porod's law:

$$\lim_{q\to\infty} q^4(I - I_l) = K \tag{6.1}$$

where I is the experimental SAXS data, I_l is the liquid scattering (fitted with a constant) and K is the Porod constant.

The invariant calculated from the F-section, Q_F, rises sharply over the first 100 s of crystallization and then remains approximately constant to about 1000 s, after which it shows a gradual decrease. We attribute the rapid increase to the development of crystalline lamellae along the flow direction, while the slow decrease in Q_F at longer t_{cryst} might be due to development of crystallinity in the interlamellar regions or perfection of the daughter lamellae which would lead to a decrease in the effective $\Delta\rho$ within the oriented parent crystallites. The invariant computed from the powder analysis, Q_P, rises quickly over the first 100 s, and continues rising at a slower rate thereafter. Analysis of the invariant along the daughter direction, Q_D, is less reliable since the intensity around the beamstop makes it difficult to extrapolate the SAXS data to $q = 0$. The growth of Q_D shows a similar trend to Q_P, increasing rapidly in the first 100 s and then gradually at longer times. As expected, the magnitude of the Q_D is about an order of magnitude smaller than Q_F due to the irregularities in spacing between the daughter lamellae and the small size of the correlated daughter-stacks. The increase of Q_P and Q_D at large t_{cryst} in contrast to the decrease in Q_F indicates the gradual development of crystallinity, probably in the less oriented regions of the sample. This accords with *ex-situ* TEM (Figure 5.6) that indicates the formation of less oriented crystallites at greater depth than the oriented skin, towards the center of the shear cell.

Analysis of WAXD

Rigorous methods for determining the degree of crystallinity are based on internal comparison and involve correcting the WAXD data acquired from an isotropic sample for thermal motions and lattice distortions, in addition to geometric contributions and polarization.[33,14,15] Further, this analysis requires data to be acquired with high signal to noise up to very large scattering angles. More commonly, a crystallinity index is determined from correlations for specific polymers based on the areas under major diffraction peaks at lower scattering angles.[34] Here, we define a crytallinity index simply as a ratio of the crystalline intensty of the powder-WAXD pattern to the total (crystal + amorphous) intensity.

Thus, the WAXD crystallinity index, x_c, is calculated from the circularly averaged powder pattern (Figure 6.5) and is given by:

$$x_c = \frac{\int_0^\infty q^2 I_c dq}{\int_0^\infty q^2 I dq} \tag{6.2}$$

where I_c is the intensity of the crystalline peaks above the baseline and I is the total scattered WAXD intensity. The crystallinity index is dominated by the crystalline peaks at low q values and does not account for distortions of the crystalline lattice that suppress the crystalline intensity at high q values. Intensities of the crystalline peaks were obtained from the WAXD pattern by fitting: an "amorphous" baseline was fit by rescaling the magnitude of a function that fit the experimental WAXD from an amorphous melt, and a set of crystalline peaks were represented by a combination of Gaussian and Lorentzian line shapes chosen by visually determining the quality of the fit. The "amorphous" halo includes scattering from air and the beryllium windows of the flow cell.

The crystallinity index increases rapidly in the first 150 s to a value of about 0.06 and then increases to about 0.12 over $t_{cryst} = 1200$ s. Since our estimate of x_c does not account for the distortions of the crystalline lattice that lead to a "loss" of crystalline intensity, and since the amorphous halo includes scattering from air and the beryllium windows, x_c represents a lower bound for the crystallinity. In the initial $t_{cryst} \approx 150$ s, crystallites develop only in ≈ 55 μm skin regions near each wall of the 500 μm shear cell, while very little if any crystallization takes place in the near-quiescent core (Chapters 3, 5). Since x_c represents a spatial average over the entire width of the shear cell, the crystallinity developed in the skin at the end of 150 s exceeds 0.27 ($0.06 \times \frac{500}{2\text{x}55}$).

The WAXD x_c data shows an abrupt break at 150 s which is an artifact of the data acquisition system: the first 10 data points (up to $t_{cryst} = 150$ s) were acquired rapidly to capture the sharp initial increase (acquisition time = 10 s/ data point) after which longer acquisition times were used to improve signal:noise. However, we observe a change in the shape of the amorphous halo in the WAXD after the first stage of data acquisition which is manifested as a break in x_c. We do not know the reason for this change in the shape of the halo.

Based on a qualitative analysis of the WAXD data and *ex-situ* TEM, we infer (Chapter 5) that crystallization under these shearing conditions proceeds via the rapid formation of oriented crystals in the skin regions. Lamellae grow radially from central "shish" structures and impinge at about 100 s after which crystallization continues at a slower rate in the less oriented regions of the sample. Our analysis of the SAXS invariant agrees well with this model (Q_F and Q_P grow rapidly during the first 100 s, but at longer times Q_F shows a small gradual decline, while Q_P shows a gradual and modest increase). For the WAXD x_c too, growth in the initial ≈ 150 s is rapid, and slows down at later times. However, the rate of growth of x_c beyond $t_{cryst} = 150$ s is more rapid than we would expect based on the SAXS. We analyze the reasons for this in the last part of Section 6.3.2.

We examine the intensity at the 110 and 040 peak positions due to diffraction from crystals by subtracting the appropriate baseline value (indicated in Figure 6.5). The diffraction from the parent and daughter 110 planes are separated in azimuthal angle for the 110 peak, but are both at the same azimuthal position (along the meridian) for the 040 peak. For increased confidence in the fit, we fit the 110 and 040 peaks simultaneously. The same ratio of the widths of parent and daughter peaks is used to fit both the 110 and 040 data, and the ratio of the areas under the parent and daughter peaks is the same after a geometrical correction for the angle made by the plane normal to the axis of symmetry. We present the data and the fits for the WAXD data at $t_{cryst} = 1200$ s as an example (Figure 6.6). The data was fitted with a constant baseline value and Lorentzians for each of the parent and daughter peaks. The baseline represents scattered intensity from the non-oriented crystals while the area under the Lorentzians represents scattering from the oriented crystals. The angular separation between the daughter crystal peaks, δ, (Figures 6.1 b, 6.6) is $\approx$ 34°, lower than the expected value of 36.8° for the idealized case of perfect uniaxial orientation. Such deviations have been explained in the literature[17] to arise due to curving and twisting of crystal lamellae that give rise to the broadening of the crystal peaks along the azimuthal direction.

The azimuthal widths of the 110 and 040 parent and daughter peaks obtained from the fits remain essentially constant with crystallization time (Figure 6.7 and Chapter 5) and compare well with the FWHM obtained by fitting the SAXS azimuthal scans. Further, the amplitude of the Lorentzians fitted to the parent and daughter peaks (which are proportional to the intensity since the widths of the peaks are unchanged with t_{cryst}) increase rapidly and in concert for the first $\approx$ 100 s after which they saturate (Figure 6.8). On the other hand, the amplitude of the baseline (which is proportional to the fraction of unoriented crystals) increases slowly with time after about 100 s. Thus, the ratio of the baseline value to the area under the oriented parent and daughter peaks, which is a measure of the ratio of the unoriented crystal fraction to the oriented, increases with crystallization time to $t_{cryst} = 1200$ s.

Using the methods of analysis developed in this section, we now examine the effect of shearing conditions–shearing duration (t_s), wall shear stress, (σ_w) and temperature (T_{cryst})–on the rate and morphology of crystallization.

6.3.2 Effect of Shearing Conditions on Crystallization

In terms of the effects of shear history on the morphology of crystallization, the qualitative trends are evident by inspection of the two-dimensional WAXD and SAXS patterns (Figure 6.9). Increasing the applied stress from below ($\sigma_w = 0.03$ MPa) to above ($\sigma_w = 0.06$ MPa) the threshold value for inducing highly anisotropic crystallization (($\sigma_{crit} \approx 0.047$ MPa at 141°C, Chapter 3) causes the structure to change from a modestly aligned orientation distribution (even for t_s as long as 20 s at $\sigma_w = 0.03$ MPa) to strong fiber-like orientation (even for t_s as short as 2 s at $\sigma_w = 0.06$ MPa). Increasing the shearing time increases the degree of orientation while reducing the ratio of daughter to parent crystals. Increasing the crystallization temperature from 141°C to 150°C for $\sigma_w = 0.06$ MPa reduces the ratio of daughter to parent crystals while retaining the strong fiber-like orientation.

Geometrical Aspects:

The long spacing is unaffected by σ_w and t_s and remains essentially constant at the same value as for quiescent crystallization at a given T_{cryst} (Figure 6.10).

The extent of orientation that develops when the polymer crystallizes is very sensitive to the wall shear stress and shearing duration. Azimuthal scans of SAXS at q^* and WAXD at the 110 and 040 peaks were fitted with Lorentzians to determine the FWHM, a qualitative measure of the orientation distribution. The angular distribution of the oriented crystal population is largely established during the shearing duration and varies weakly if at all after cessation of flow. A separate population of poorly oriented or isotropic crystallites grows in as well, but on a longer timescale. With increasing shearing time, the degree of alignment of oriented crystals and their rate of formation both increase. At 141°C, for $\sigma_w = 0.06$ MPa, the orientation sharpens dramatically as t_s increases from 0.5 to 12 s (Figure 6.11): for $t_s \leq 1$ s, the 110 peaks are too broad to determine the FWHM[35] ; for $t_s = 2$ s, the 110 peaks for the parent crystallites have a FWHM that increases gradually from 10° to 13° over approximately 2000 s; and for $t_s = 12$ s, these peaks have a FWHM of only 7-8°, remaining essentially unchanged from 15 s to 2000 s. The timescale for growth of the oriented crystal population decreases from roughly 1700 s for $t_s = 0.5$ s to approximately 100 s for $t_s = 12$ s (Figure 6.11 a versus d). The ratio of parent to daughter crystals associated with the oriented material increases with increasing shearing duration: for $t_s \leq 1$ s, the daughter peaks appear more prominent than the parents; the two sets of peaks have similar heights for $t_s = 2$ s; and for $t_s = 12$ s of shear, the parent peaks are stronger than the daughters. In this most oriented case, an estimate of the ratio of parent to daughter crystallite content can be computed to be 3.65 – based on the areas of their respective peaks after accounting for a geometrical factor for the angle made by respective crystals to the symmetry axis.[17,36]

The wall shear stress, σ_w, has a much more pronounced impact on shear enhanced orientation than the shearing duration, t_s. A comparison of the azimuthal scans for crystallization of PP-300/6 at T_{cryst} = 141°C, σ_w = 0.03 MPa and t_s = 20 s with experiments at a higher wall shear stress, σ_w = 0.06 MPa reveals that much lower shearing durations, t_s between 0.5 s and 1 s, are required to produce the same extent of orientation at the higher σ_w (compare Figures 6.11 a,b and Figure 6.12 b). It is interesting to note that while the total strain at the wall (estimated by measuring the amount of sample extruded during shear) is approximately 100 for t_s = 20 s at σ_w = 0.03 MPa, the total strain for t_s = 1 s at σ_w = 0.06 MPa is only about 10. Thus, at constant T_{cryst} and either constant t_s or γ_{tot}, crystallites are much more strongly oriented and develop much more rapidly and have higher parent to daughter ratio following shear at higher σ_w.

At higher T_{cryst} (150°C), the trends with shearing duration are similar to those at the lower crystallization temperature (Figure 6.13): with increase in shearing duration, there is an increase in the extent of orientation and in the ratio of oriented parent to daughter lamellae in the oriented population; the FWHM of the oriented azimuthal peaks remains essentially constant with t_{cryst}. The most noticeable effects of increasing T_{cryst} are to decrease the ratio of daughter to parent crystals (cf., t_s = 12 s for 141°C/0.06 MPa and t_s = 6 s for 150°C/0.06 MPa), and to slow crystallization kinetics. This trend in daughter to parent ratio accords with literature reports of a decrease in the density of crosshatches with temperature.[37,38,4,5] The ratio of the unoriented crystal fraction to the oriented increases very gradually at 150°C compared to 141°C since the quiescent crystallization kinetics slow down by close to an order of magnitude with the increase in T_{cryst}.

SAXS Invariant and WAXD Crystallinity Index:

Our SAXS invariant and WAXD crystallinity data confirm our previous rheo-optical results (Chapter 3) and accord well with the literature[1,22]: shearing the polymer leads to a rapid acceleration in crystallization kinetics. It is not possible to quantitatively compare the numerical values of the invariant, Q_P and the WAXD x_c calculated from powder patterns for different shearing conditions even after normalizing the data for acquisition time and incident X-ray intensity due to the effect of the orientation distribution on scattering, and due to the change in the ratio of parent to daughter crystals with shearing conditions (see end of Section 6.3.2). Nevertheless, it is instructive to examine the buildup of various measures of crystallinity following different shearing conditions and compare their relative growth rates.

The acceleration of the growth of the overall crystallinity vis a vis that of the oriented population can be assessed by examining the transient growth of the SAXS invariants, Q_F and Q_P, and the crystallinity index computed from the WAXD data. With increasing shearing duration, the rate of formation of lamellar stacks with normals along the flow direction increases (Figure 6.14). For sufficiently short shearing durations, the acceleration in formation of the oriented lamellae is similar to the acceleration of crystallization as a whole: for the shortest t_s shown for each σ_w and T_{cryst}, the time course of Q_F and Q_P have similar shapes (i.e., the flow-induced acceleration is roughly isotopic).

With increasing shearing duration, a separation of timescales emerges, with the oriented crystallites growing rapidly in the early stages. This change is evident in differences in the shapes of $Q_F(t)$ and $Q_P(t)$; the oriented population shows a relatively fast initial rise, then flattens; whereas the overall population grows not only with the oriented population at first, but continues to build up even after Q_F plateaus. The inception of the plateau is evident in Q_F at 141°C for $\sigma_w = 0.03$ MPa; $t_s = 20$ s and $\sigma_w = 0.06$ MPa; $t_s = 0.5$ s. For strongly oriented cases (e.g., 141°C, $\sigma_w = 0.06$ MPa, $t_s = 2$ s or 12 s or 150°C, $\sigma_w = 0.06$ MPa, $t_s = 8$ s), the long time plateau in Q_F is quite pronounced. During the long time plateau in Q_F, the overall crystallinity continues to grow in a manner similar to quiescent crystallization (for example, during the Q_F plateau at 141°C, Q_P rises with time at a rate between that of the quiescent case and perhaps double that rate).

The qualitative trends in the time course of overall crystallization indicated by Q_P are also evident in the WAXD crystallinity index, x_c. At the end of Section 6.3.2, we discuss the change in the relative rates of increase of x_c and Q_P with the transition from oriented growth at early time to unoriented growth at later times.

The overall trends in the invariant and x_c at 150°C are qualitatively similar to those at lower T_{cryst}: for lower t_s, the SAXS invariants increase gradually as does the WAXD crystallinity index, while for shearing durations that lead to highly oriented crystallization ($t_s \geq 6$ s), Q_P and x_c increase monotonically, while Q_F increases over about 400 s after which it starts declining gradually.

For milder shearing conditions at 150°C (for example, $t_s = 1$ s) where crystallinity does not develop as rapidly as for $t_s = 8$ s, the proximity of the SAXS scattering to the beamstop makes the SAXS peak appear as a shoulder close to the beamstop. This makes it difficult to extract the SAXS invariants since extrapolation of the intensity to low q cannot be done reliably. Thus, while x_c data (at $t_s = 1$ s) indicate the gradual development of crystallinity with t_{cryst}, the SAXS invariants show, at best, a very modest increase.

The SAXS invariant along the F-section (0.06 MPa, $t_s = 8$ s) is considerably higher compared to lower temperature 141°C (0.06 MPa, $t_s = 12$ s). However, the magnitudes of Q_P are comparable in the two cases: this is because at a higher T_{cryst}, the SAXS peak appears at lower q, and in the Lorentz-corrected powder invariant ($q^2 I_P$), the increase in I_P is offset by the shift to smaller q. While the extent of orientation (Figures 6.11 d and 6.13 c) and the WAXD x_c (Figure 6.14) that develop under these conditions are similar, the almost threefold higher magnitude of the plateau of Q_F at 150°C than at 141°C is surprising. We speculate that the increased scattering intensity at higher T_{cryst} might arise due to a change in the local crystallinity, x_l in the lamellar stacks and/or due to the decreased extent of crosshatching at the higher temperature, which would give rise to a higher effective electron density difference within the parent lamellar stacks.

It is more difficult to interpret the difference in the height of the Q_F-plateau with increasing t_s (t_s = 2 s to t_s = 12 s at 141°C and σ_w = 0.06 MPa, Figure 6.11 c,d) simply in terms of the increase in effective electron density resulting from a change in cross hatching since there is also a change in the orientation distribution for the two shearing conditions. This change in the orientation distribution affects both the WAXD and the SAXS. For WAXD, there is a decrease in the total diffracted intensity from the crystalline peaks with increase in the extent of uniaxial orientation (see next Subsection). Thus, we expect that the ratio of the "true" crystallinity after ≈ 100 s for t_s = 12 s compared to t_s = 2 s is greater than $\frac{x_c(t_s=12s, t_{cryst}=100s)}{x_c(t_s=2s, t_{cryst}=100s)}$ (≈ 2.5, Figure 6.14). As the degree of crosshatching is lower at t_s = 12 s compared to 2 s, the effective electron density contrast within the oriented parent lamellar stacks increases with shearing duration. Consequently, we would expect that the ratio of the Q_F-plateau for t_s = 12 s compared to 2 s at ≈ 100 s would be greater than 2.5. However, we find that this ratio is ≈ 2 (Figure 6.14). Thus, the decrease in crosshatching alone is not enough to explain the difference in the SAXS Q_F plateau values with shearing duration. For this, we need to consider the effect of the change in the orientation distribution on the SAXS invariants relative to the WAXD x_c.

Changes in SAXS Relative to WAXD

There is an interesting change in the SAXS patterns with increase in the extent of crystallinity relative to the corresponding change in the WAXD. For samples subjected to "strong" shearing, the rate of increase of Q_P is slower relative to x_c at longer times when less oriented crystallization takes place (Figures 6.4, 6.14). The most significant contribution to this effect probably arises from the change in the orientation distribution on the scattering intensity: for SAXS, the intensity from isotropically distributed lamellar stacks is greatly reduced as compared to oriented lamellae with their normals along the flow direction; however, for α-phase isotactic polypropylene, there is an increase in the diffracted crystalline intensity for an isotropic distribution of crystalline unit cells compared to uniaxial orientation about the c-axis for the parent crystals. Another contribution to this effect is that WAXD diffraction from crystalline units in the daughter lamellae for c-axis oriented samples is comparable to that from parent crystals while the SAXS intensity from the daughter lamellae is much weaker relative to the parents (Figures 6.1, 6.4 and 6.6). This might be due to the weaker degree of long range ordering of the daughter lamellae relative to the parents leading to a decrease in the SAXS intensity, but which does not significantly affect the WAXD.

We examine the effects of orientation distribution on the WAXD and SAXS in detail. In the WAXD experiment, for uniaxial orientation of crystals along the flow direction, the geometry of the Ewald sphere dictates that the density of crystal plane normals is lowest when the crystals are oriented along the flow direction. Since the diffracted intensity is proportional to the number of crystal planes that are in the Bragg condition, an isotropic distribution gives rise to a 10 to 30% higher average intensity from the significant WAXD peaks for the α-form as compared to uniaxially orientation along the flow direction (see Equation 6.3). The ratio of the diffracted crystal intensity from oriented crytals relative to that from an isotropic distribution of the same number of plane normals is given by[17]:

$$\frac{\text{oriented}}{\text{isotropic}} = \frac{2}{\pi cos(\theta) sin(\phi)} \tag{6.3}$$

where θ is the Bragg diffraction angle and ϕ is the angle made by the normal of the crystal plane to the symmetry (flow) direction. Thus, a smaller number of crystal planes distributed isotropically could give rise to the same WAXD crystal intensity as a larger number oriented in the flow direction. For SAXS, it is easy to see that the scattering intensity from lamellae arranged such that all their normals are along the flow direction will be much higher to lamellae with their normals distributed isotropically. Thus, as a less oriented population of crystals begins to grow, the relative increase in the SAXS powder invariant, Q_P, will be smaller than the increase observed for the WAXD x_c.

6.4 Discussion

6.4.1 Comparison of X-ray Scattering with Rheo-Optics

Our *in-situ* synchrotron SAXS and WAXD data on the influence of shearing conditions on microstructural development accord qualitatively with and provide new insights into results from *in-situ* rheo-optical measurements (Chapters 3, 4) and *ex-situ* microscopy (Chapters 3, 5). Previously, we observed that for "mild" shearing conditions (viz. low wall shear stress, σ_w = 0.03 MPa or short shearing durations, t_s < 4 s at σ_w = 0.06 MPa) at 141°C, we do not observe the formation of transient oriented structures manifested in the birefringence during flow (Chapter 3), nor an anisotropic skin-core morphology in *ex-situ* microscopy. WAXD shows that weak anisotropy is present and strong daughter populations form; the combination of these two characteristics leads to the observation of negligible birefringence. On the other hand, for "strong" shearing, viz. t_s > 4 s at σ_w = 0.06 MPa, the birefringent upturn is observed during shear due to the formation of unaxially oriented crystallites in the high shear skin regions. The birefringent upturn correlates with *ex-situ* evidence for formation of an oriented skin near the walls of the shear cell and a relatively less oriented core farther from the walls (Chapter 3).

In the corresponding X-ray scattering experiments, we observe that the extent of orientation increases with the wall shear stress and duration: shearing at σ_w = 0.03 MPa leads to only modest orientation even for t_s = 20 s (Figure 6.12), correlating with the absence of strongly oriented crystallites from rheo-optical data and microscopy. The crystallites formed at σ_w = 0.06 MPa get progressively more oriented with increase in t_s (Figure 6.12). Comparing the SAXS invariants, Q_P and Q_F with the WAXD x_c at σ_w = 0.06 MPa and t_s = 2 s, we observe that crystallites oriented along the flow direction form in the initial $t_{cryst} \approx$ 100 s (Figure 6.14), but the extent of orientation of these crystals (from the FWHM of the WAXD 110-azimuthal data; Figure 6.11) is lower than for "strong" shearing, viz. t_s = 12 s at the same σ_w. From the absence of skin-core morphology in the *ex-situ* micrographs at $t_s s$ = 2 s, it appears that the nucleation density and orientation of the crystals that develop under these conditions is insufficient to give rise to a skin-core morphology. For "strong" shearing, the oriented α crystals of isotactic polypropylene that are observed by WAXD during shear (correlating with the formation of the birefringent upturn; Chapter 4) are densely nucleated and template the formation of highly oriented crystals after flow cessation (correlating with the skin-core morphology observed *ex-situ*; Chapter 4).

A comparison of the *in-situ* birefringence to the WAXD immediately prior to and following the cessation of shear provides further information regarding the nature of the birefringent upturn. Our WAXD evidence (Chapter 4) unambiguously correlates the upturn in birefringence during flow with the formation of oriented α crystallites. However, after cessation of shear, the birefringence decays rapidly to a non-zero residual value for "strong" shearing (Figures 3.6 and 4.4). Since our WAXD x_c data does not exhibit a corresponding drop immediately after cessation of shear, we conclude that the decay in the birefringence is not due to melting of oriented crystallites formed during flow. Rather, we speculate that it is due to the elastic "snapping back" of polymer molecules distorted by the imposed flow, that are tethered to the growing crystal. The rapid decay of the birefringence, is then, in good accord with the timescales for stress relaxation expected at these temperatures. This distortion of the polymer chain configuration due to flow might also account for the rapid increase in crystallinity during flow, evident for "strong" shearing (e.g. $\sigma_w = 0.06$ MPa, $t_s = 12$ s at $T_{cryst} = 141°C$, Figure 6.6).

The increase in the ratio of parent to daughter lamellae observed in the azimuthal distribution of WAXD intensity for the 110-reflection (Figure 6.12), with increase in shearing duration is interesting. While it is tempting to rationalize the change in parent:daughter ratio by recourse to the high nucleation density and high degree of orientation of the line-like precursors for higher shearing durations, this is not satisfactory since White and Bassett[5] have demonstrated that, under quiescent conditions, the degree of cross-hatching and the thickness of the cross-hatched lamellae are independent of the anisotropy of nucleation. Instead, we speculate that the increase in parent:daughter ratio with shearing duration arises due to the enhanced nucleation and growth of parent crystals compared to daughters during flow. Polymer chains stretched out in the flow direction lead to rapid nucleation and growth of the parent lamellae (chain axis in the crystal along flow direction) relative to the daughters (chain axis in the crystal nearly normal to the flow direction). Crystals formed after flow cessation are however, expected to form with a lower parent:daughter ratio, typical of quiescent crystallization, since the stresses relax very rapidly after cessation of flow. As a considerable fraction of the crystallization in the skin develops during flow (especially for "strong" shearing), the enhanced parent:daughter ratio generated for the crystals during flow skews the overall ratio in the final crystalline structure, giving rise to the observed effect of shearing duration on parent:daughter ratio. The decrease in parent:daughter ratio with t_{cryst} from cessation of flow to impingement in the skin, that is expected from this picture, is evident in Figure 6.11 d.

The large daughter population explains why we do not see the *in-situ* birefringence rise to high values for $\sigma_w = 0.06$ MPa and $t_s = 2$ s, even though the X-ray data indicates the formation of oriented crystallites (Figure 3.3). Since the crossed-polarizer intensity is a measure of the difference in the refractive indices along the flow direction and perpendicular to it, an increase in the density of crosshatched lamellae, that grow almost perpendicular to the flow-aligned parent lamellae, will lead to a decrease in the overall optical anisotropy. Thus, for these strongly cross-hatched crystallites, $I_\perp/I_{tot}$ does not go "over orders" and only rises gradually to 0.5 at long times due to depolarization caused by multiple scattering from developed crystallites. Such morphological insight cannot be obtained from optical data alone.

Since scattering of visible light by the crystallites that leads to turbidity in the *in-situ* rheo-optical measurements is dependent on the shape, size and optical anisotropy of the scatterers, it is very difficult to interpret the origin of the turbidity based on the invariant or x_c. However, it is interesting to note that for "strong" shearing conditions (141°C, $\sigma_w = 0.06$ MPa, $t_s = 12$ s), x_c builds up very rapidly at short times (≈ 100 s), and in fact, by the end of the shear pulse, it attains about 25% of the value ultimately attained at ≈ 1000 s. For milder shearing conditions, the growth in x_c is more gradual.

The *ex-situ* electron microscopy of the skin-core structure for the "strong" shearing experiment (141°C, $\sigma_w = 0.06$ MPa, $t_s = 12$ s; see Figures 5.6 - 5.8) provide us with a morphological model for interpretation of the *in-situ* X-ray scattering. The TEM indicates the formation of row nucleated structures with lamellae that radiate from the central line. The spacing between these rows increases as we move away from the wall from about 260 nm near the wall to about 700 nm at the transition from the skin to the core. Since the periodicity of these structures is similar to the wavelength of light used in the rheo-optical experiments, they scatter light strongly. Thus the development of these structures correlates with the sample turning turbid in the rheo-optical experiment and with the increase in x_c and the invariants in WAXD and SAXS respectively. Such morphological insight cannot be obtained from optical and X-ray data alone, and requires the incorporation of *ex-situ* TEM.

6.4.2 A Mechanistic Description of Shear Enhanced Crystallization

Our rheo-optical, X-ray scattering and microscopy data, taken together, suggest a mechanistic model for shear enhanced crystallization. As PP-300/6 is sheared at 141°C at $\sigma_w = 0.06$ MPa, the chains in the polymer melt are distorted and exhibit a nonlinear overshoot due to stretching of chains in the flow direction upon start up of flow. This overshoot is observed at about 2 s in the *in-situ* rheo-birefringence experiments (Figure 3.6). The temperature dependence of the upturn in the birefringence indicated that the transition to oriented "shish-kebab" structures is rate limited by the attainment of a critical level of orientation of the chains locally, and thus, is controlled by the melt rheology (Chapter 4). At $\sigma_w = 0.06$ MPa, the critical oriented chain configuration for transition to oriented growth is reached by the highly distorted high molecular weight chains in PP-300/6 and line like precursors develop (Chapters 4, 5). These precursors immediately nucleate the development of lamellae that grow radially away from the center.

Rheological control of the route to anisotropic nucleation mediated by the formation of oriented precursors (suggested by our rheo-optical X-ray scattering and TEM data) indicates that the slow relaxing high molecular weight species in the sample play a prominent role in anisotropic crystallization. In a polydisperse sample, even though the average level of chain orientation is constant at a fixed σ_w, not all the chains are equally distorted. The strongest conformational distortion is suffered by the slowest relaxing species in the melt (for example, the high molecular weight chains).[39] We speculate that the highly anisotropic chain segment distribution in the vicinity of these high molecular weight species leads to the formation of the oriented precursors. This speculation accords well with literature reports of the effect of high molecular weight species in the formation of oriented structures during flow induced crystallization,[40,41,21] and is supported by recent work from our laboratory using model narrow distribution isotactic polypropylenes[42] and bidisperse blends of the model resins (see Chapter 4).

In the short term shearing experiments on PP-300/6, we speculate that these precursors are nucleated at a constant rate in the high shear regions as the polymer is sheared for longer durations until the high molecular weight species is "used up." The nucleation density at short shearing durations (for example, $t_s \approx 2$ s) is low, and consequently, only a modest overall orientation is developed (Figure 6.11), and a pronounced skin-core morphology does not develop (Figure 3.4). For "strong" shearing ($t_s = 12$ s; t_{cryst} at saturated plateau value), line-like precursors are densely nucleated in the skin region. As a consequence, the orientation distribution set up during shear persists as crystallization ensues to develop a highly anisotropic skin. Once the line-like precursors form, lamellae start growing radially. The increase in WAXD x_c (Figure 6.14) suggests that, for "strong" shearing conditions, a significant amount of the crystallization in the skin takes place *during* flow (probably due to the distortion of the chain configuration which promotes crystallization), and crystallization is essentially complete when the crystallites grow to impingement. The parent to daughter ratio during flow is also observed to be higher than after flow-cessation. After cessation of flow, the polymer melt relaxes rapidly, and further crystallization from the "precursor templates" proceeds under quiescent-like conditions with the corresponding parent to daughter ratio.

To verify whether the crystallites do indeed show the transition from sparsely nucleated and less-oriented to densely nucleated and highly oriented, we examine *ex-situ* micrographs of PP-300/6 subjected to short-term shearing for increasing durations of shear, at $T_{cryst} = 141°C$ and $\sigma_w = 0.06$ MPa (Figure 6.15). All the samples were quenched after holding for $t_{cryst} = 21600$ s, long enough for the sample to become turbid even under quiescent conditions. Since our supply of PP-300/6 had been depleted by our previous experiments, these experiments had to be performed on a sample which showed slight visible discoloration after sample preparation. This sample crystallized more rapidly than the original PP-300/6 (quiescent $t_{1/2}$ smaller by a factor of less than 2); however, the trends observed for the dependence of $t_{1/2}$ with t_s are similar to those for the original PP-300/6, despite the shift to lower values. Also, similar to the behavior of the original sample, the upturn in the birefringence appears at about $t_s \approx 4$ to 5 s, and the formation of strong orientation *in-situ* correlates with the formation of this upturn. Thus, we feel that inferences drawn from the trends observed for the development of microstructure in the *ex-situ* micrographs are robust and would qualitatively hold for the original PP-300/6. Polarized optical micrographs of sections in the 1-2 (flow and velocity gradient) plane for samples subjected to t_s = 1 s, 2 s, 4 s and 8 s indicate that there is no orientation for $t_s < 2$ s (Figures 6.15 a,b). For $t_s = 2$ s (Figure 6.15 b), mild orientation is noticed as sparsely nucleated lines appear near the walls of the shear cell. For $t_s \geq 4$ s (Figure 6.15 c,d), a fully developed skin-core morphology is evident. The thickness of the skin region remains essentially constant with $t_s \geq 4$ s and is similar to the thickness observed for the skin in our previous experiments for $t_s = 12$ s (Figure 3.4). The voids in the middle of the samples observed in the micrographs is due to rupture of the sample near the center of the shear cell in response to stresses set up in the sample as it contracts and the volume shrinks. These micrographs suggest that the model captures the essential physics that underlies shear-enhanced crystallization. Electron micrographs that document the detailed microstructural details of the crystallites with t_s are required to confirm our speculation about the geometrical development of the morphology. This work is ongoing in our laboratory.

6.5 Conclusions

Synchrotron SAXS and WAXD are used to follow the evolution of crystallinity and orientation for PP-300/6 subjected to different shearing conditions using the short-term shearing protocol.

We find that while the SAXS long spacing is influenced only by the crystallization temperature, the orientation distribution and rate of crystallization are strongly influenced by the shear stress imposed and by the duration of shear. Under conditions which lead to the formation of strongly oriented skin-core morphologies ("strong" shearing), anisotropic crystallites develop rapidly in high-shear regions near the walls of the shear cell, followed by gradual growth of less oriented crystallites farther from the wall. Under conditions of milder shear, the rate of growth of crystallinity is gradual compared to strong shearing, and less oriented morphologies develop. Interestingly the ratio of parent to daughter lamellae for the oriented crystallite population increases with increase in shearing time, imposed wall shear stress and temperature.

Our data suggests a mechanistic model for shear-enhanced crystallization: the growth of oriented crystallites are nucleated by the formation of a strongly anisotropic distribution of chain segments in the melt upon imposition of flow. These template the formation of oriented row-nucleated structures in the flow direction. The orientation grow during flow persists due to the densely nucleated central lines from which lamellae develop radially. These lamellae grow at quiescent growth speeds until a fully impinged crystalline structure is formed. For milder shearing conditions, less oriented structures are formed. We speculate that the lower nucleation densities under these conditions lead to the development of less oriented structures.

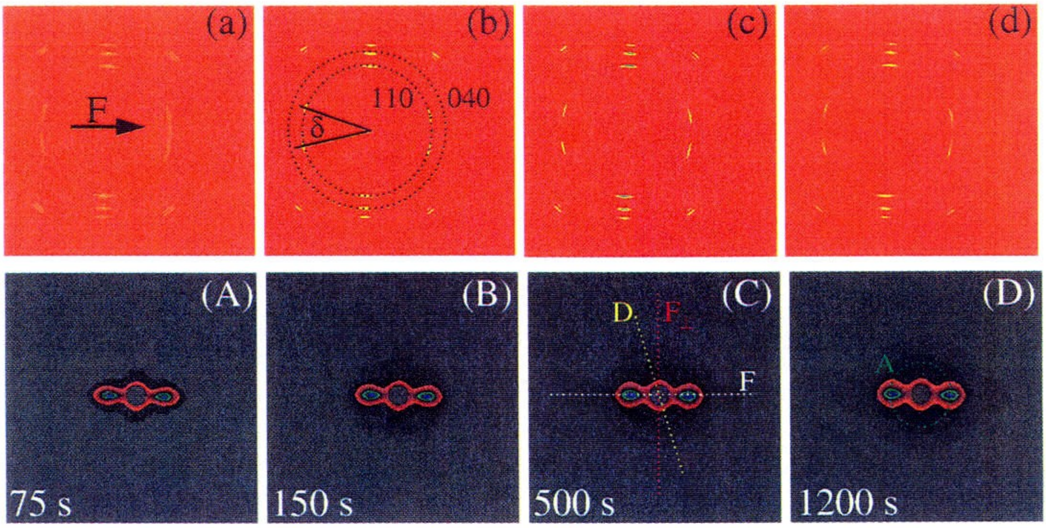

Figure 6.1: Two-dimensional WAXD (top row) and the corresponding SAXS (bottom row) patterns showing the evolution of crystallinity with crystallization time after cessation of shear for $T_{cryst} = 141°C$, $\sigma_w = 0.06$ MPa, $t_s = 12$ s. The time at which these patterns were acquired is indicated on the SAXS. The flow direction is horizontal (indicated for the WAXD at 75 s). The development of lamellae with normals along the flow direction (F), along the daughter lobes (D) and perpendicular to the flow ($F_\perp$) is examined by analyzing the SAXS intensity along the respective directions.

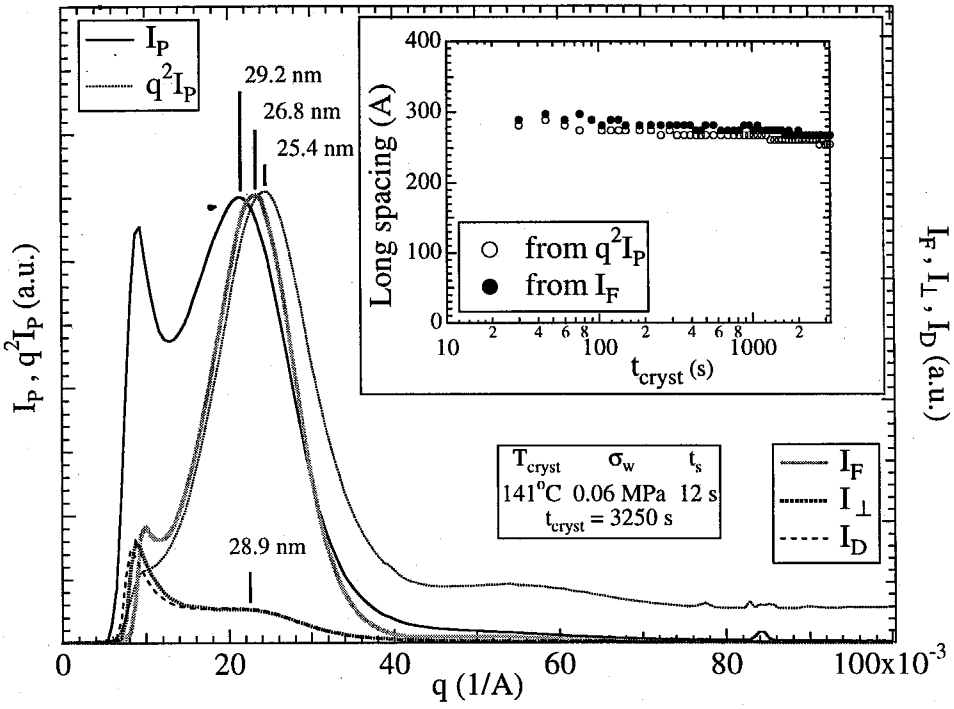

Figure 6.2: Lamellar long spacing calculated from the powder-average, the Lorentz-corrected powder patterns as well as from sections along F, D and $F_\perp$ (defined in Figure 6.1) for data acquired at t_{cryst} = 3250 s (T_{cryst} = 141°C, σ_w = 0.06 MPa, t_s = 12 s). The inset shows that the long spacing from the Lorentz-corrected powder pattern and from the section along the flow direction are in good agreement and are nearly constant over the crystallization time, t_{cryst}.

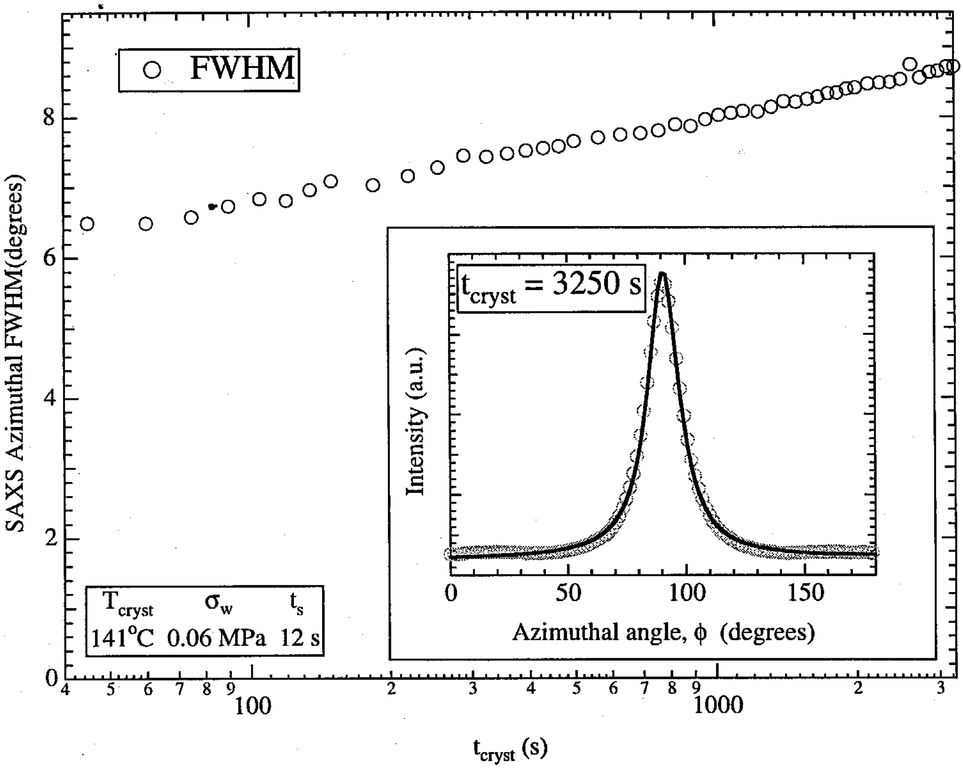

Figure 6.3: The FWHM calculated from the azimuthal intensity of the SAXS at the peak value, q*, increases gradually as a function of the crystallization time (T_{cryst} = 141°C, σ_w = 0.06 MPa, t_s = 12 s). The inset shows an example of the Lorentzian fit to the SAXS azimuthal scan acquired at t_{cryst} = 3250 s.

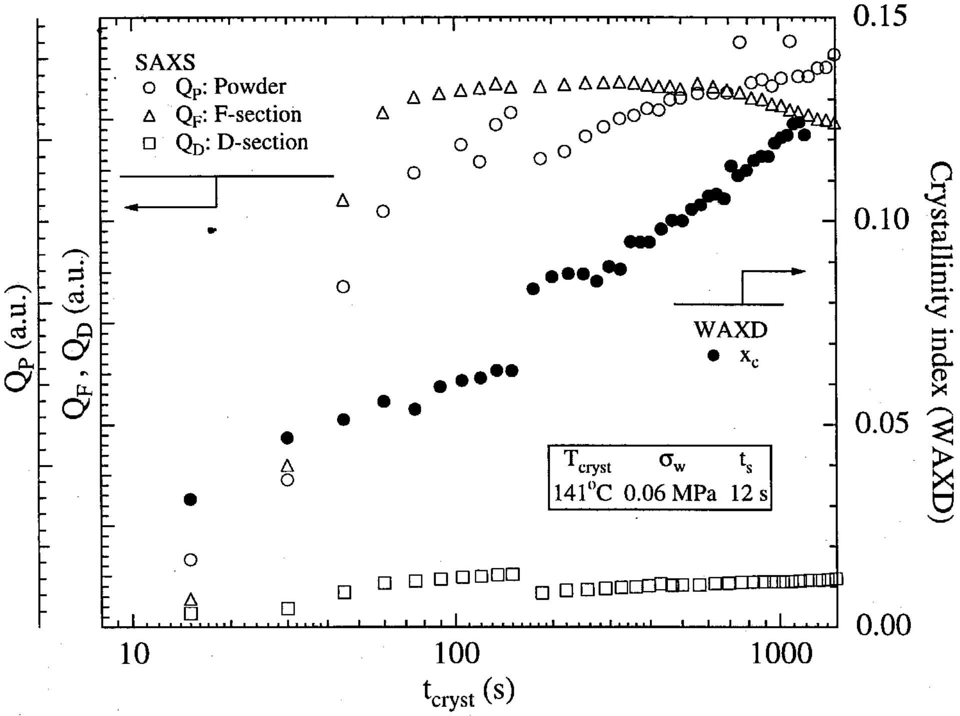

Figure 6.4: Comparison of the SAXS invariants from the Lorentz-corrected powder pattern, Q_P, and from directions along the flow and daughter sections (Q_F and Q_D respectively) with the crystallinity index computed from the WAXD, x_c (T_{cryst} = 141°C, σ_w = 0.06 MPa, t_s = 12 s). Q_F, Q_P and Q_D rise sharply in the first ≈ 100 s; after that, Q_P and Q_D show a modest gradual increase, while Q_F plateaus and then decreases gradually. The trends in x_c parallel those for Q_P, except that the rate of increase beyond 100 s is steeper for WAXD compared to SAXS.

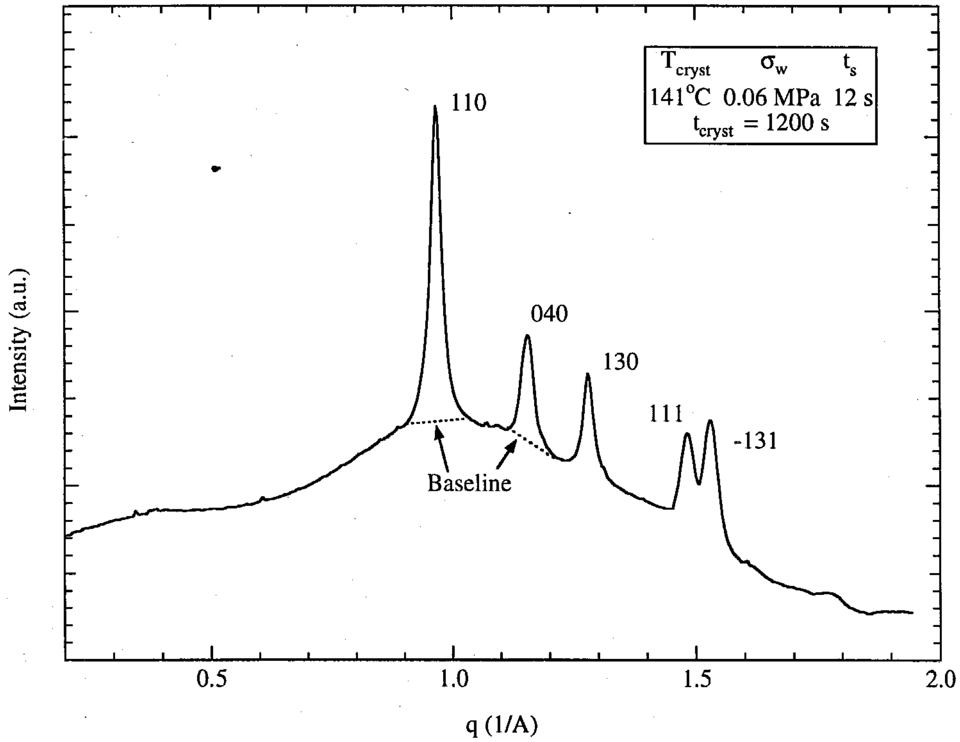

Figure 6.5: The circularly-averaged WAXD powder pattern with the crystalline peaks indexed for $T_{cryst} = 141°C$, $\sigma_w = 0.06$ MPa, $t_s = 12$ s at $t_{cryst} = 1200$ s. The "amorphous" value of the baseline is indicated for the 110 and 040 reflections.

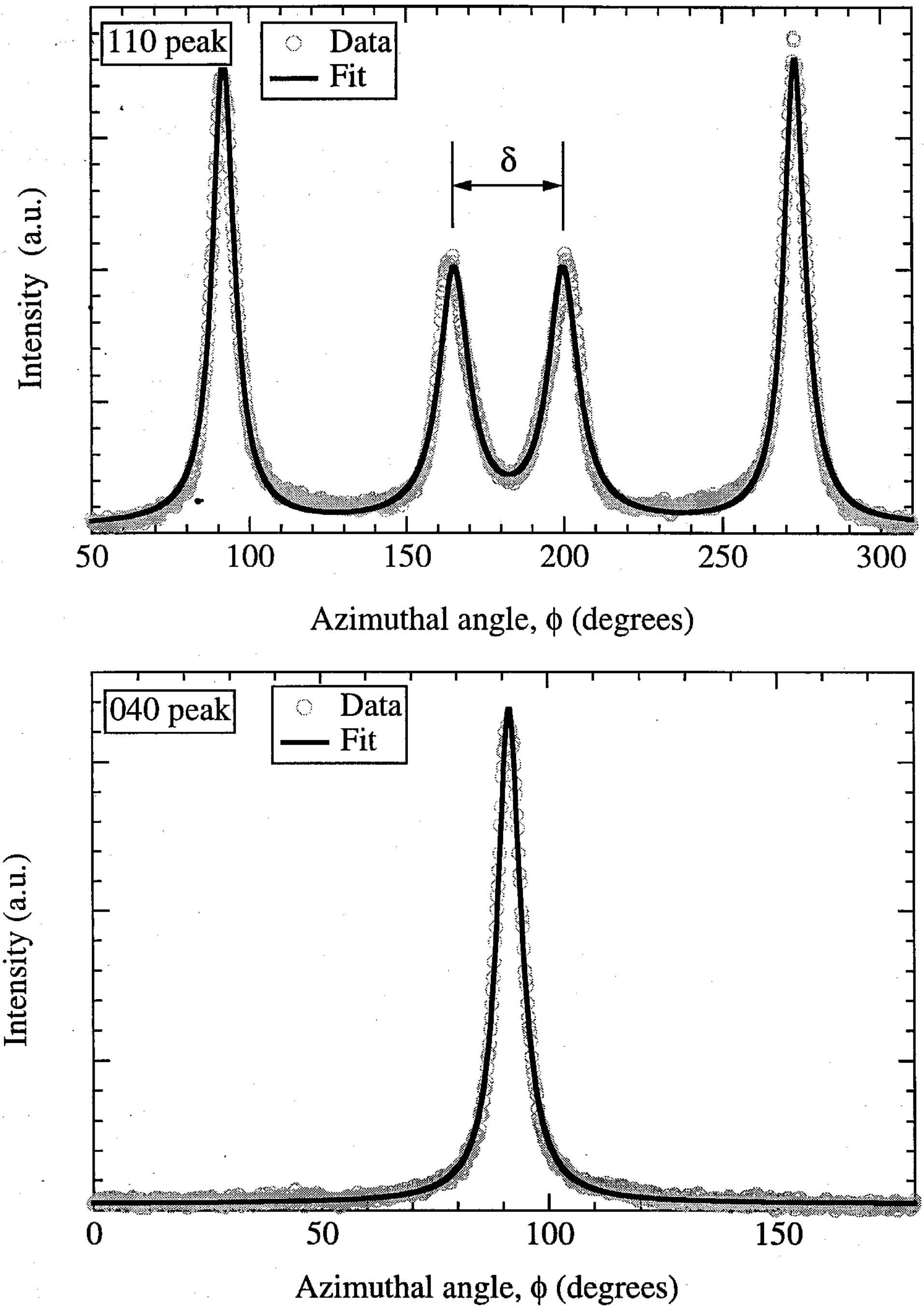

Figure 6.6: The azimuthal data at the 110 and 040 WAXD peak locations with the appropriate baseline value subtracted are shown with the fit for t_{cryst} = 1200 s (T_{cryst} = 141°C, σ_w = 0.06 MPa, t_s = 12 s). The two data sets are fitted simultaneously as explained in the text. The azimuthal separation of the crosshatched peaks, δ (see Figure 6.1) is $\approx$ 34°.

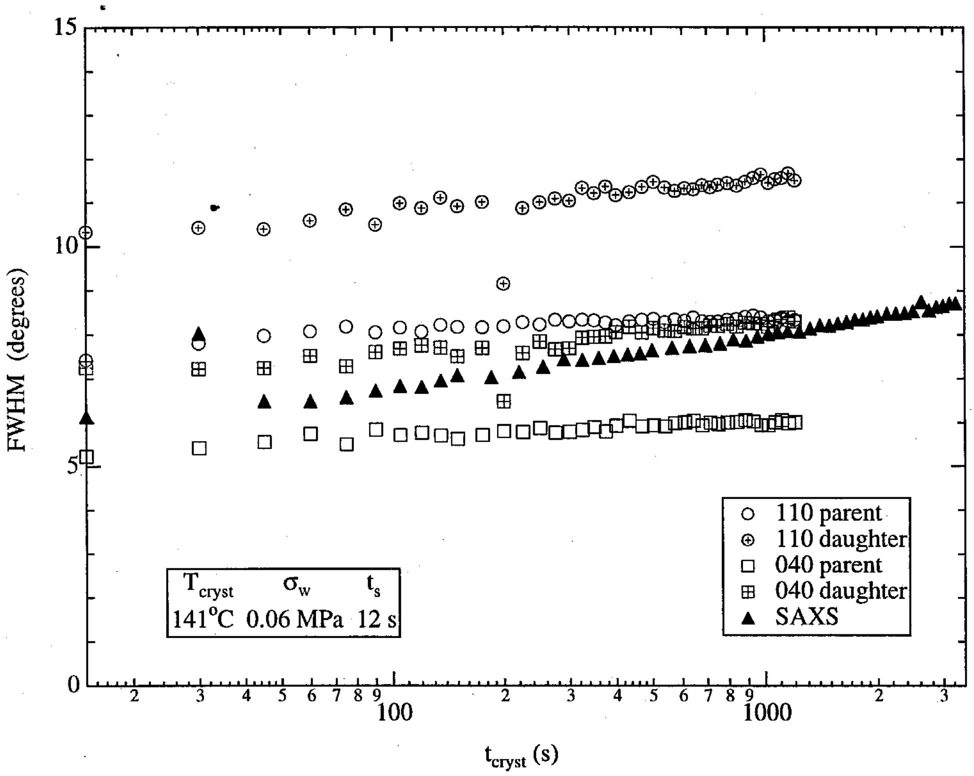

Figure 6.7: For $T_{cryst} = 141°C$, $\sigma_w = 0.06$ MPa, $t_s = 12$ s, the change in the FWHM for the azimuthal WAXD intensity for the parent and daughter peaks at the 110 and 040 reflections (determined by fitting, see Figure 6.6) are very weak functions of the crystallization time, t_{cryst}.

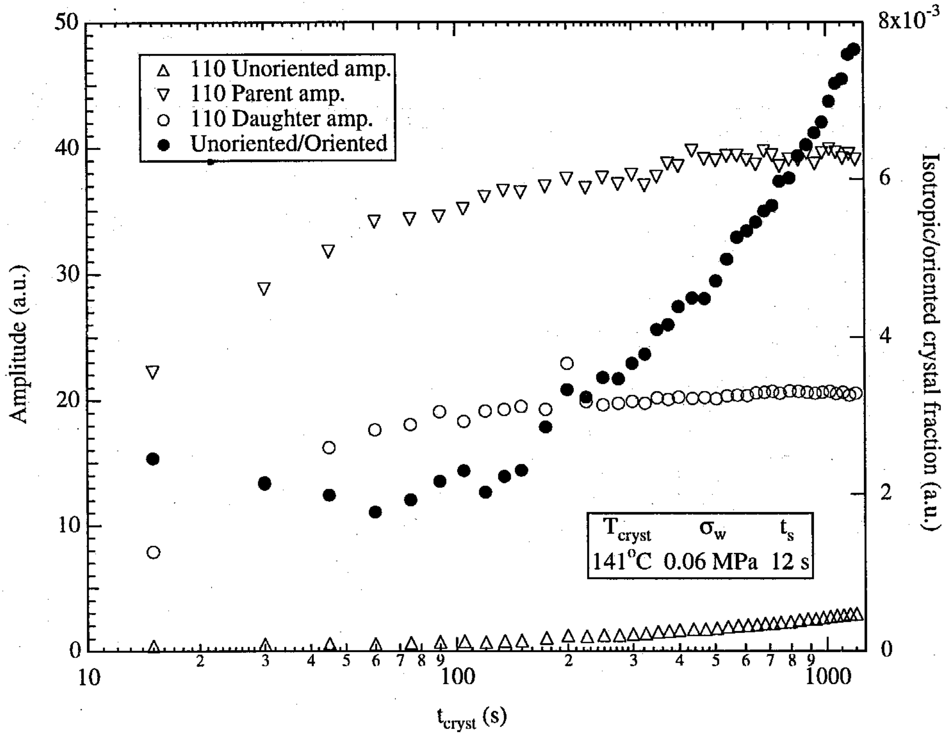

Figure 6.8: Change in the amplitude of the fits to the parent and daughter 110-peaks, and to the unoriented crystal component with crystallization time for $T_{cryst} = 141°C$, $\sigma_w = 0.06$ MPa, $t_s = 12$ s.

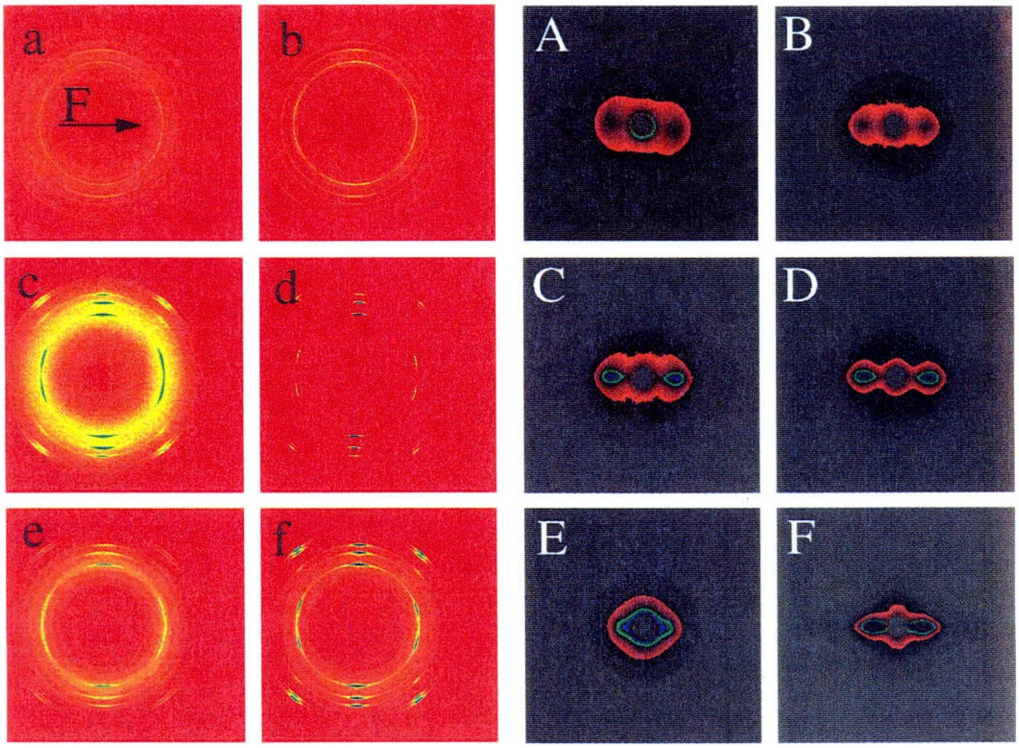

Figure 6.9: Two-dimensional SAXS and the corresponding WAXD showing the influence of σ_w, t_s and T_{cryst} on crystallization. The last patterns acquired for each experiment (viz. well developed crystallinity) is shown. **A** (t_{cryst} = 2525 s) and **a** (t_{cryst} = 3350 s) show data for T_{cryst} = 141°C and σ_w = 0.03 MPa for t_s = 1 s and 2 s respectively; **B** (2360 s) and **b** (1700 s) show data for 141°C, σ_w = 0.03 MPa, t_s = 20 s; **C** (2525 s) and **c** (1700 s) show data for 141°C, σ_w = 0.06 MPa, t_s = 2 s; **D** (3250 s) and **d** (1200 s) show data for 141°C, σ_w = 0.06 MPa, t_s = 12 s; **E** (3750 s) and **e** (4500 s) show data for 150°C, σ_w = 0.06 MPa, t_s = 1 s; and **f** (7350 s) shows WAXD data for 150°C, σ_w = 0.06 MPa, t_s = 6 s while **F** (1520 s) shows SAXS data for 150°C, σ_w = 0.06 MPa, t_s = 8 s.

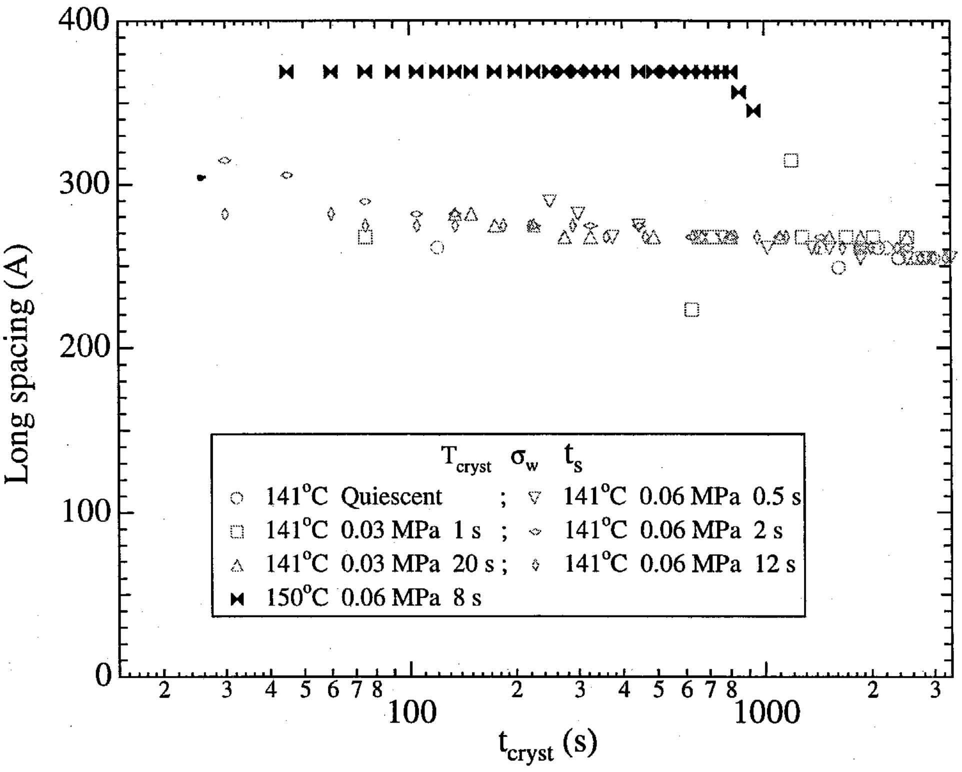

Figure 6.10: The SAXS long spacing is not affected by σ_w or t_s. The lamellar spacing at a particular T_{cryst} does not change for sheared samples compared to the value for quiescent crystallization.

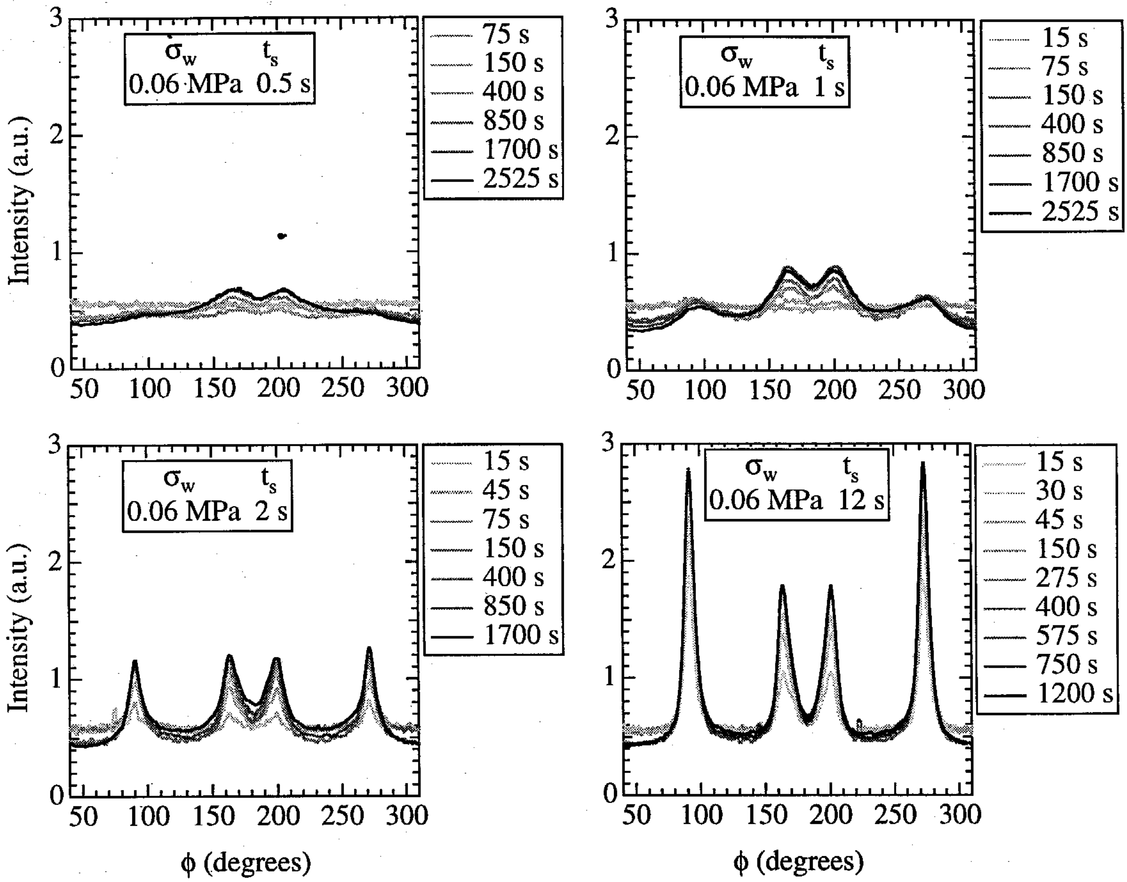

Figure 6.11: Evolution of azimuthal intensity at the 110-WAXD peak with crystallization time for t_s = 0.5 s, 1 s, 2 s and 12 s at T_{cryst} = 141°C and σ_w = 0.06 MPa.

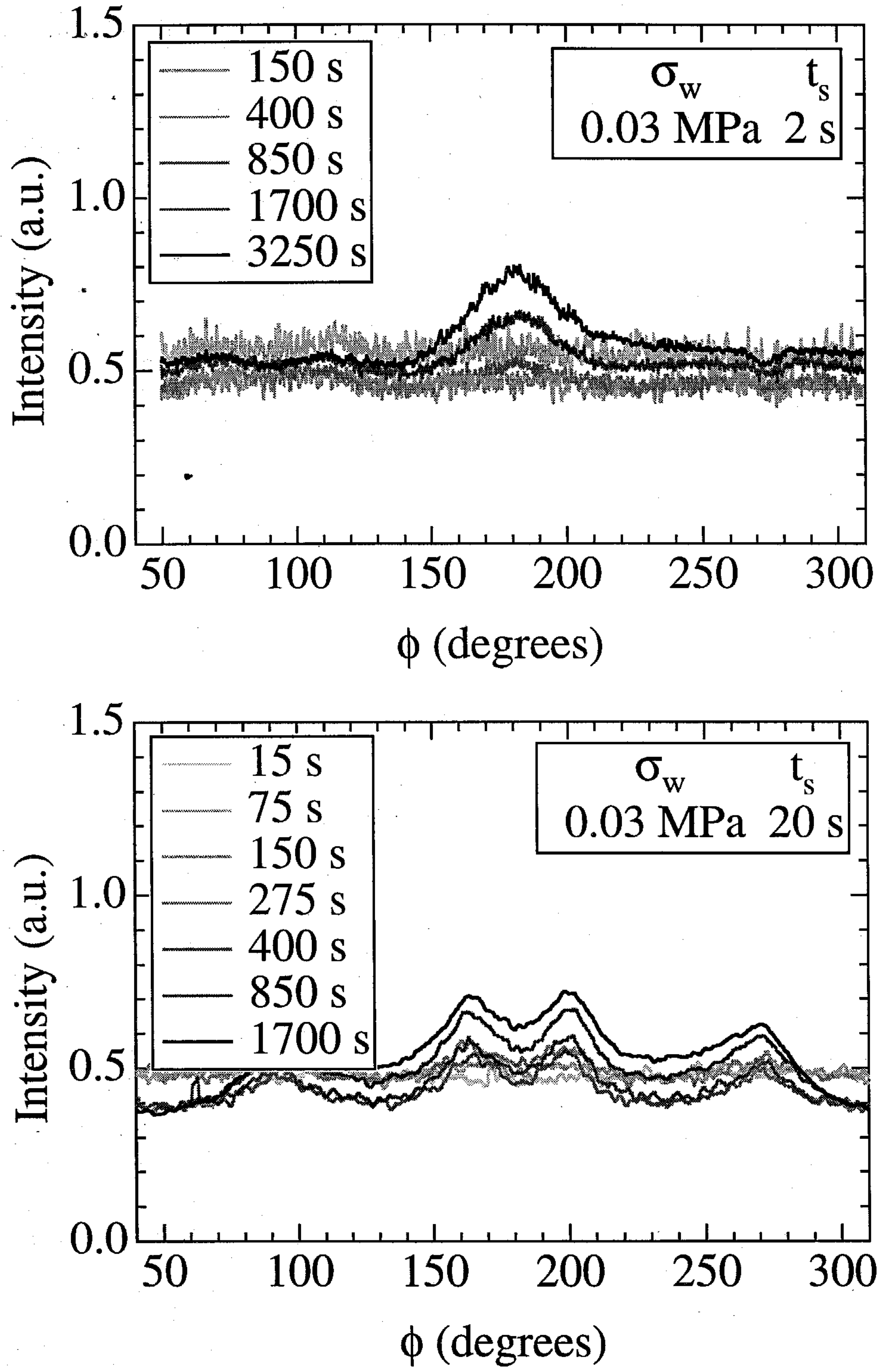

Figure 6.12: Evolution of azimuthal intensity at the 110-WAXD peak with t_{cryst} for t_s = 1 s and 20 s at T_{cryst} = 141°C and σ_w = 0.03 MPa.

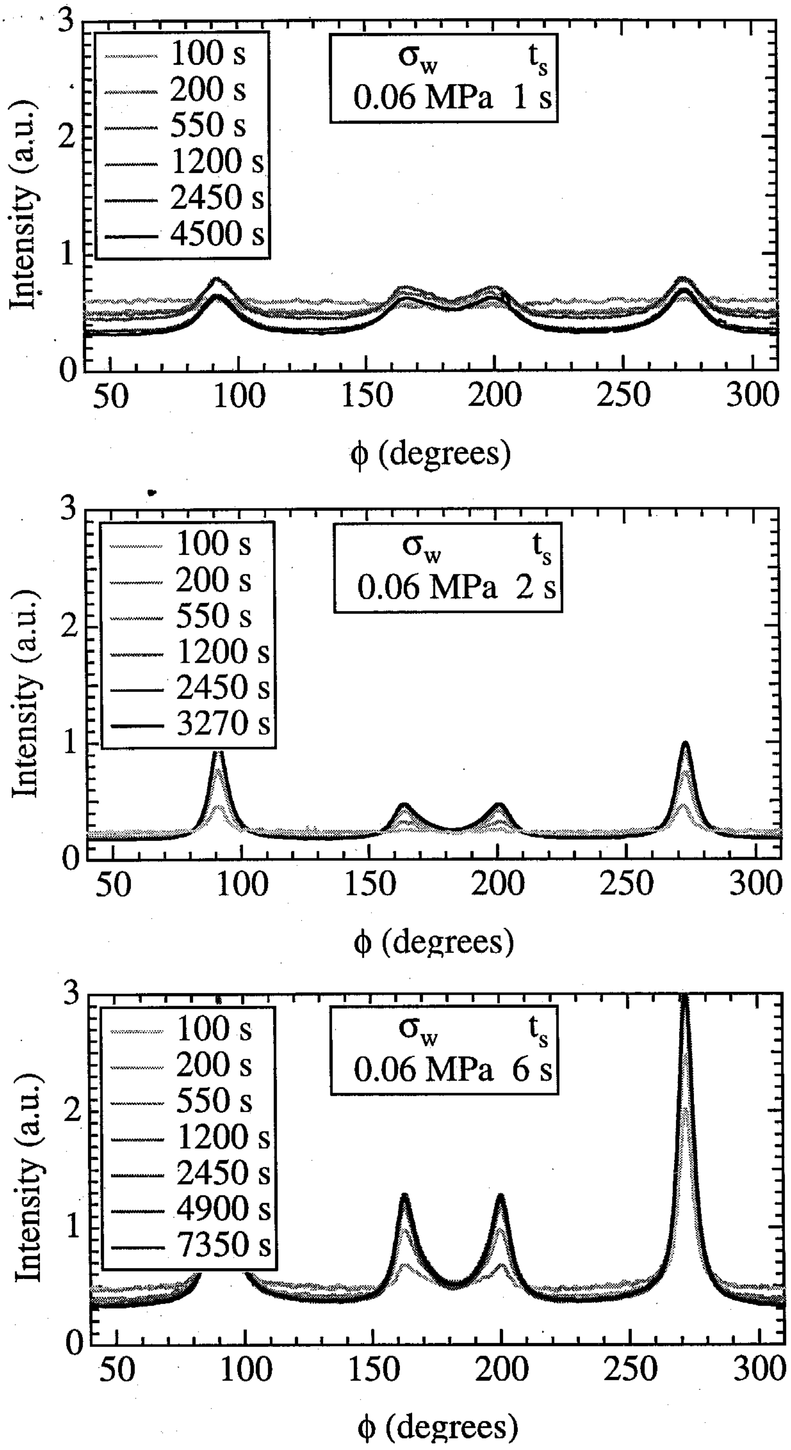

Figure 6.13: Evolution of azimuthal intensity at the 110-WAXD peak with crystallization time for $t_s = 1$ s, 2 s and 6 s at $T_{cryst} = 150°C$ and $\sigma_w = 0.06$ MPa.

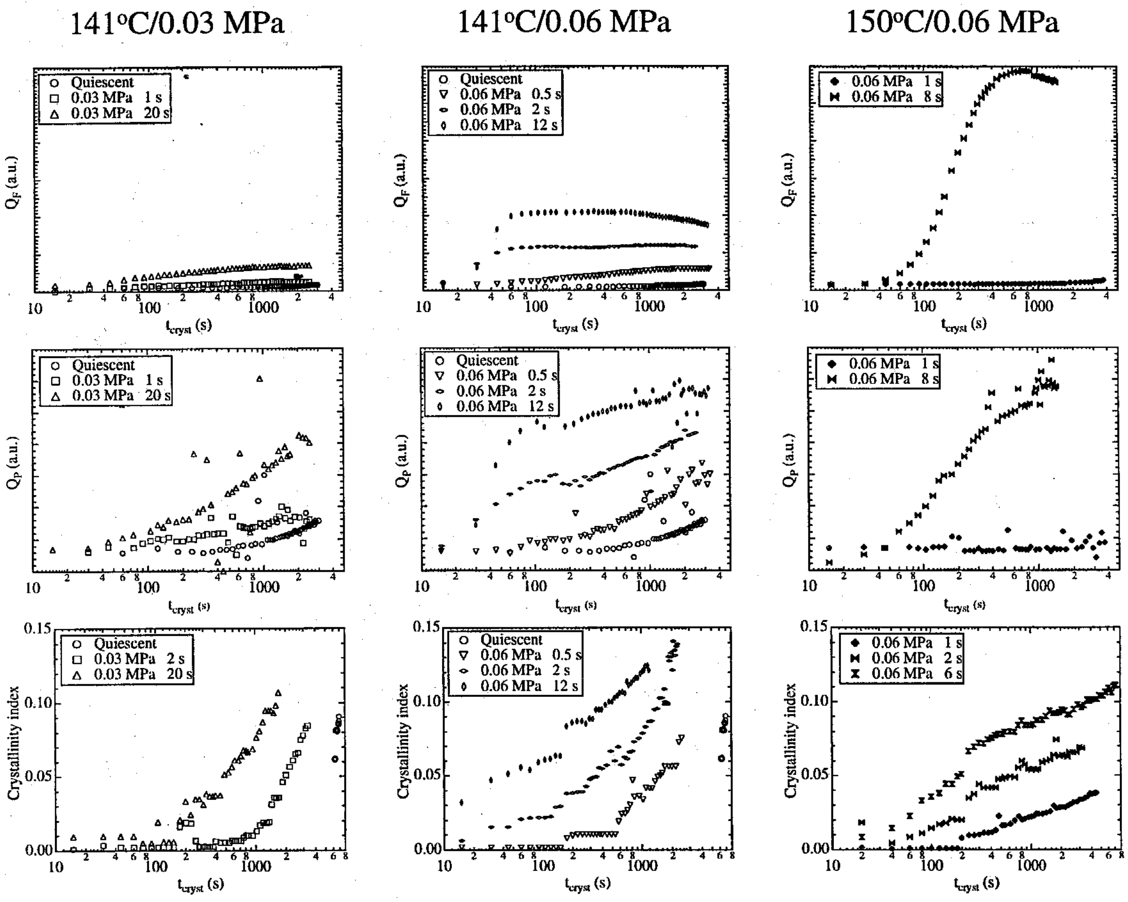

Figure 6.14: Influence of σ_w, t_s and T_{cryst} on the evolution of Q_F (first row), Q_P (second row) and x_c (last row): the first two columns show data at 141°C for σ_w = 0.03 MPa and 0.06 MPa respectively while the last column is for data at 150°C and σ_w = 0.06 MPa. Note that the arbitrary units used to plot the SAXS invariants are consistent across each row.

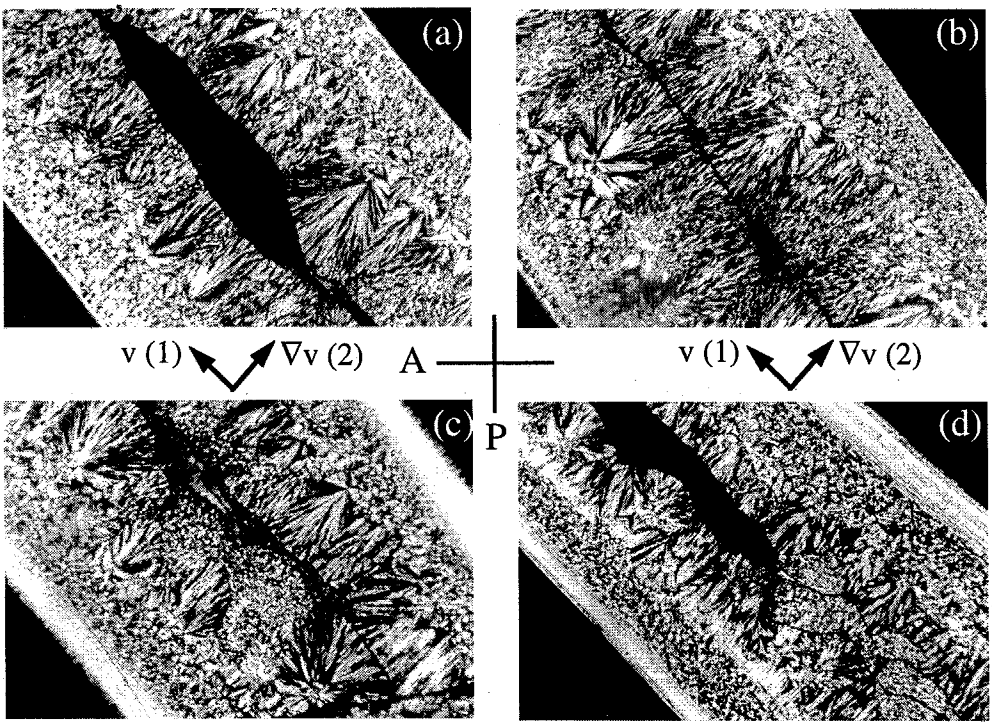

Figure 6.15: Polarizing optical micrographs that show the evolution of semicrystalline microstructure in the flow-velocity gradient plane with shearing duration for $T_{cryst} = 141°C$ and $\sigma_w = 0.06$ MPa. The direction of the polarizer and analyzer are as indicated.

Bibliography

1. van Krevelen, D. *Chimia* **1978,** *32,* 279.

2. Clark, E. S.; Spruiell, J. E. *Polym. Eng. Sci.* **1976,** *16,* 176.

3. Lovinger, A. J. *J. Polym. Sci. (Polym. Phys.)* **1983,** *21,* 97.

4. Lotz, B.; Wittmann, J. C.; Lovinger, A. J. *Polymer* **1996,** *22,* 4979.

5. White, H. M.; Bassett, D. C. *Polymer* **1997,** *38,* 5515.

6. Ulcer, Y.; Cakmak, M. *Polymer* **1997,** *38,* 2907.

7. Fitchmun, D. R.; Mencik, Z. *J. Polym. Sci. (Polym. Phys.)* **1973,** *11,* 951.

8. Meijer, H., Ed.; *Processing of Polymers,* Vol 18 VCH (NY): 1997.

9. Choi, K. J.; Spruiell, J. E.; White, J. L. *J. Polym. Sci. (Polym. Phys.)* **1982,** *20,* 27.

10. Kwack, T. H.; Han, C. D. *J. Appl. Polym. Sci.* **1988,** *35,* 363.

11. Isayev, A. I.; Chan, T. W.; Shimojo, K.; Gmerek, M. *J. Appl. Polym. Sci.* **1995,** *55,* 807.

12. Fujiyama, M.; Wakino, T.; Kawasaki, Y. *J. Appl. Polym. Sci.* **1988,** *35,* 29.

13. Ferry, J. D. *Viscoelastic Properties of Polymers,* John Wiley, NY: 3 ed.; 1980.

14. Alexander, L. E. *X-ray diffraction methods in polymer science,* Wiley-Intescience: 1969.

15. Baltá-Calleja, F. J.; Vonk, C. G. *X-ray scattering of synthetic polymers,* Elsevier: 1989.

16. Koch, E. E., Ed.; *Handbook on Synchrotron Radiation,* Elsevier, NY: 1983.

17. Dean, D. M.; Rebenfeld, L.; Register, R. A.; Hsiao, B. S. *J. Mater. Sci.* **1998,** *33,* 4797.

18. Ezquerra, T. A.; Lopez-Cabarcos, E.; Hsiao, B.; Balta-Calleja, F. *Phys. Rev. E* **1996,** *54,* 989.

19. Cakmak, M.; Teitge, A.; Zachmann, H.; White, J. *J. Polym. Sci. (Polym. Phys.)* **1993,** *31,* 371.

20. Ryan, A.; Patrick, J.; Fairclough, A.; Terrill, N.; Olmstead, P.; Poon, W. *Faraday Discuss.* **1999,** *112,* 13.

21. Pople, J. A.; Mitchell, G. R.; Sutton, S. J.; Vaughan, A. S.; Chai, C. K. *Polymer* **1999,** *40,* 2769.

22. Liedauer, S.; Eder, G.; Janeschitz-Kriegl, H.; Jerschow, P.; Geymayer, W.; Ingolic, E. *Intern. Polym. Proc.* **1993,** *8,* 236.

23. Liedauer, S.; Eder, G.; Janeschitz-Kriegl, H. *Intern. Polym. Proc.* **1995,** *10,* 243.

24. Kumaraswamy, G.; Issaian, A. M.; Kornfield, J. A. *Macromolecules* **1999,** *32,* 7537.

25. Strobl, G. R.; Schneider, M. *J. Polym. Sci. (Polym. Phys.)* **1980,** *18,* 1343.

26. Ruland, W. *Colloid Poly. Sci.* **1977,** *255,* 419.

27. Stribeck, N.; Ruland, W. *J. Appl. Cryst.* **1978,** *11,* 535.

28. Santa-Cruz, C.; Stribeck, N.; Zachmann, H. G.; Balta-Calleja, F. J. *Macromolecules* **1991,** *24,* 5980.

29. Hsiao, B. S.; Verma, R. K. *J. Synchrotron Rad.* **1998,** *5,* 23.

30. Albrecht, T.; Strobl, G. *Macromolecules* **1995,** *28,* 5267.

31. Ryan, A. J.; Stanford, J. L.; Bras, W.; Nye, T. M. W. *Polymer* **1997,** *38,* 759.

32. Vleeshouwers, S. *Polymer* **1997,** *38,* 3213.

33. Ruland, W. *Acta. Cryst.* **1961,** *14,* 1180.

34. Isasi, J. R.; Mandelkern, L.; Galante, M. J.; Alamo, R. G. *J. Polym. Sci. (Polym. Phys.)* **1999,** *37,* 323.

35. For conditions that showed very little orientation, the extremely broad peaks made it difficult to accurately determine the baseline value, and therefore, the data could not be fitted to determine the FWHM of the peaks, the parent to daughter ratio or the ratio of oriented to unoriented crystal fraction.

36. There is a slight distortion in the shape of the daughter peaks since the WAXD pattern is obtained using a flat plate CCD. As the daughter peaks are not located on the meridian (horizontal direction in Figure 6.9), we expect the contribution from this distortion to be small and neglect it in our calculations.

37. Padden, F. J (Jr.); Keith, H. D. *J. Appl. Phys.* **1959,** *30,* 1479.

38. Janimak, J. J.; Cheng, S. Z. D.; Giusti, P. A.; Hsieh, E. T. *Macromolecules* **1991,** *24,* 2253.

39. Andersen, P.; Carr, S. *Polym. Eng. Sci.* **1978,** *18,* 215.

40. Bashir, Z.; Odell, J. A.; Keller, A. *J. Mater. Sci.* **1984,** *19,* 3713.

41. Keller, A.; Kolnaar, H. W. H. Processing of Polymers. In , Vol. 18; Meijer, H. E. H., Ed.; VCH: 1997.

42. Kumaraswamy, G.; Issaian, A. M.; Sun, Y.; Kornfield, J. A.; Liu, W.; Yeh, F.; Hsiao, B. S. *in preparation.*